D I P L O M A R B E I T

The Physical Electrochemistry of Monolayer Protected Metal Nanoclusters

Ausgeführt am Department of Chemistry

University of Dublin, Trinity College

unter der Anleitung von

Dr. Michael E. G. Lyons

durch

Dominic Sigmar Janisch

Unterm Hag 6
3341 Ybbsitz
Austria

22. Juni 2005

Abstrakt

In dieser Arbeit wurden nach der Brust Methode Goldnanopartikel, geschützt mit Thiolat-Monolagen, hergestellt. Es wurde versucht, die gleiche Methode auch zur Herstellung von Silber- und Kupfer-nanopartikel anzuwenden. Dies gelang gut im Fall des Silbers und nur teilweise bei Kupfer. Die erhaltenen Nanopartikel wurden mittels TEM, zur Bestimmung der Größenverteilung, und mittels UV/VIS Spektroskopie und einiger elektrochemischer Untersuchungsmethoden charakterisiert. Die Kapazität der Cluster wurde aus Zyklovoltametrie-Messungen abgeleitet, Diffusionskoeffizienten wurden mittels Chrono-amperometrie und rotierender Scheibenelektrode bestimmt und die Kinetik der Durchtrittsreaktion wurde mittels Wechselstromimpedanz charakterisiert.

Abstract

In this work thiolate monolayer protected gold nanoparticles were prepared following the Brust method. It was tried to use this method also for the synthesis of silver and copper nanoparticles. This was successful in the case of silver but only partly successful with copper. The particles obtained were characterized using TEM for analysis of the core size distribution, UV/VIS spectroscopy, and several electro-chemical methods. The cluster capacitance was derived from cyclic voltammetry measurements, the diffusion coefficient was determined using chronoamperometry and rotating disc electrode, and data on the electron transfer kinetics was obtained from A. C. impedance measurements.

Contents

1 Introduction 1
1.1 Fundamental Concepts of Electrochemistry 2
1.1.1 Electrode Reactions 2
1.1.2 Electron Transfer across the Electrode-Solution Interface 4
1.1.3 Mass Transport Mechanisms in Electrolytes 8
1.1.4 Electrode Kinetics 10
1.2 Monolayer Protected Metal Nanoparticles 16
1.2.1 Synthesis of Nanoparticles 17
1.2.1.1 Gold 18
1.2.1.2 Silver 23
1.2.1.3 Copper 24
1.2.2 Self-Assembled Monolayers (SAMs) 25
1.2.3 Structure of Monolayer Protected Clusters 30
1.2.4 Reactions of MPCs 32
1.3 Applications of MPCs 37
References 41

2 Methods and Experimental 45
2.1 Synthesis of Gold Nanoparticles 46
2.2 Synthesis of Silver Nanoparticles 48
2.3 Synthesis of Copper Nanoparticles 51
2.4 Place Transfer (Ligand Exchange) 54
2.5 Transmission Electron Microscopy 55
2.6 Elemental Analysis 56
2.7 Nuclear Magnetic Resonance 56
2.8 Electrolyte and Electrode Preparation for Electrochemical Measurements 57
2.9 Cyclic Voltammetry 59
2.10 Rotating Disc Electrode 62
2.11 Differential Pulse Voltammetry 66
2.12 Chronoamperometry 67

2.13 A. C. Impedance 69
2.14 UV/VIS Spectroscopy 72
References 75

3 Results and Discussion 76
3.1 Distribution of the Core Size 77
3.2 Surface Coverage 82
3.3 Place Transfer 84
3.4 Surface Plasmon Resonance 88
3.4.1 The Effect of the Monolayer Thickness 90
3.4.2 Light Sensitivity of Silver Nanoparticles 91
3.5 Nanoparticle Capacitance 93
3.5.1 The Concentric Sphere Capacitor Model 95
3.5.2 Quantized Charging 97
3.6 Diffusion Coefficient 108
3.6.1 Calculation from the Stokes-Einstein Equation 108
3.6.2 Determination by Rotating Disc Electrode 109
3.6.3 Determination by Chronoamperometry 113
3.6.4 Determination by A. C. Impedance 117
3.6.5 Comparison of the Diffusion Coefficient Results 118
3.7 Charge Transfer Resistance and Exchange Current from Impedance Measurements 119
3.8 Transfer Coefficient and Exchange Current Density from Tafel Plots 122
References 126

4 Conclusion 127

5 Outlook 131

Acknowledgements 133
Abbreviations 134
Symbols 135

1. Introduction

1.1 Fundamental Concepts of Electrochemistry

This part will give a short introduction into some fundamental concepts, as far as they are of relevance for the experimental work undertaken. For further reading, there are several textbooks on electrochemistry available[1, 3-6,] as well as textbooks on physical chemistry with an electrochemistry chapter[2].

1.1.1 Electrode Reactions

An electrode reaction is a heterogeneous chemical process involving the transfer of electrons to or from a surface, generally a metal or a semiconductor. The electrode can act as only a source (for reduction) or a sink (for oxidation) of electrons transferred to or from species in solution, as in

$$O + ne^- \rightleftharpoons R \qquad (1.1)$$

where O and R are the oxidized and reduced species, respectively. Alternatively, the electrode can take part in the electrode reaction, as in dissolution of a metal M:

$$M \rightleftharpoons M^{n+} + ne^- \qquad (1.2)$$

The reduction and oxidation processes responsible for the overall reaction in a cell are separated in space: oxidation takes place at the anode.

$$Red_1 \rightarrow Ox_1 + n\, e^- \qquad (1.3)$$

The electrons released in the oxidation travel through the external circuit and re-enter the cell through the other electrode, the cathode. There they cause reduction:

$$Ox_2 + n\, e^- \rightarrow Red_2 \qquad (1.4)$$

The electrode reaction, however, is a sequence of basic steps. To maintain a current it is essential to supply reactant to the electrode surface and to remove the product, as well as for the electron transfer reaction at the surface to occur. Therefore, for example in a reaction where O is reduced to R, the electrode reaction involves three steps:

$$O_{bulk} \xrightarrow{mass\ transport} O_{electrode} \qquad (1.5)$$

$$O_{electrode} \xrightarrow{electron\ \ transfer} R_{electrode} \qquad (1.6)$$

$$R_{electrode} \xrightarrow{mass\ transport} R_{bulk} \qquad (1.7)$$

The reaction rate, and hence the electric current, is dependent on the rate of the slowest step.

Electrode reactions are half-reactions, by convention expressed as reductions, and each has associated with it a standard electrode potential $E^{\otimes}$, measured relative to the normal hydrogen electrode with all species at activity $a_i = 1$.

For half-reactions at equilibrium, the actual potential, E, can be related to the standard electrode potential according to the *Nernst Equation*

$$E = E^{\otimes} - \frac{RT}{nF} \sum \upsilon_i \ln a_i \qquad (1.8)$$

where ν_i are the stoichiometric numbers, which are positive for products (reduced species) and negative for reagents (oxidized species).

The relationship between standard potential and the Gibbs energy ΔG^0 is given by

$$\Delta G_0 = -nFE_0 \qquad (1.9)$$

1.1.2 Electron Transfer across the Electrode-Solution Interface

Electron transfer on the surface of an electrode involves electron tunnelling between the closely spaced energy levels of the electrode and the ions in solution. For the explanation of electrochemical reaction mechanisms, it is important to understand the structure of this interface, which forms the boundary between electronic conductivity in the electrode and ionic conductivity in solution. The most primitive model of this phase boundary is represented in terms of an electrical double layer, which consists of a sheet of positive charge at the surface of the electrode and a sheet of negative charge next to it in the solution or vice versa. This arrangement creates an electrical potential difference, called the Galvani potential difference, between the bulk of the metal electrode and the bulk of the solution. More sophisticated models for the electrode-solution interface try to

describe the gradual changes in the structure of the solution between the charged electrode surface and the bulk of the solution.

The Helmholtz Model (1879)

In the Helmholtz[7] layer model of the interface, the solvated ions arrange themselves along the surface of the electrode but they are held away from it by their hydration spheres (Figure 1.1). The location of the sheet of ionic charge, which is called the outer Helmholtz plane (OHP), is identified as the plane running through the solvated ions. In this simple model, the electrical potential changes linearly within the layer bounded by the electrode surface on one side and the OHP on the other.

The Gouy-Chapman Model (1910)

The Helmholtz layer model ignores the disrupting effect of thermal motion, which tends to break up and disperse the rigid outer plane of charge. In the Gouy[8]-Chapman model of the diffuse double layer, the disordering effect of thermal motion is taken into account (Figure 1.2). In the diffuse double layer of charge the concentration of counter ions is greatest next to the electrode surface and decreases progressively until a homogeneous distribution of ions is reached in the bulk electrolyte.

The Stern Model (1924)

The Gouy-Chapman theory neglects the finite size of the ions. Stern[9] postulated that ions could not approach the electrode beyond a plane of closest approach, thereby introducing the ion size. The basis of Stern's model is a combination of the Helmholtz and Gouy-Chapman approaches (Figure 1.3).

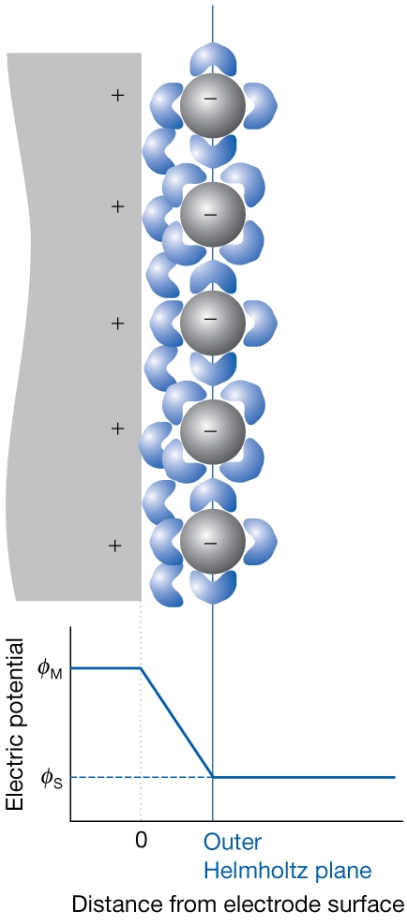

Figure 1.1. Helmholtz Model (all reproduced from reference 2)

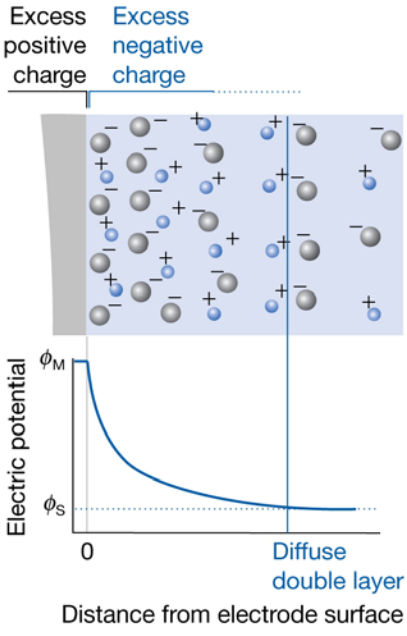

Figure 1.2. Gouy-Chapman Model

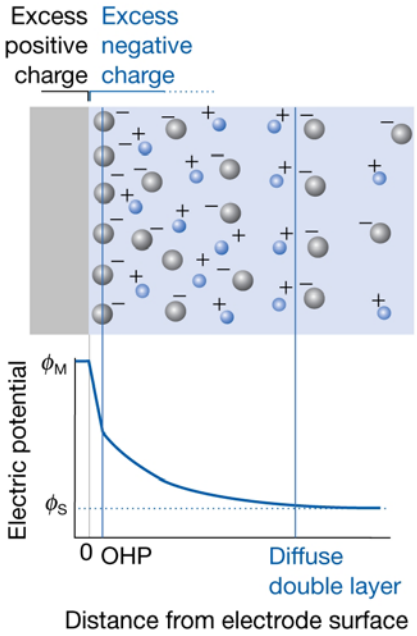

Figure 1.3. Stern Model

The Grahame Model (1947)

Grahame[10] realized that full interpretation of the thermodynamic data required two planes of closest approach, one for specifically adsorbed ions (inner Helmholtz plane, IHP) and one for non-specifically adsorbed ions (outer Helmholtz plane, OHP), and a diffuse layer region extending to the bulk electrolyte phase (Figure 1.4)

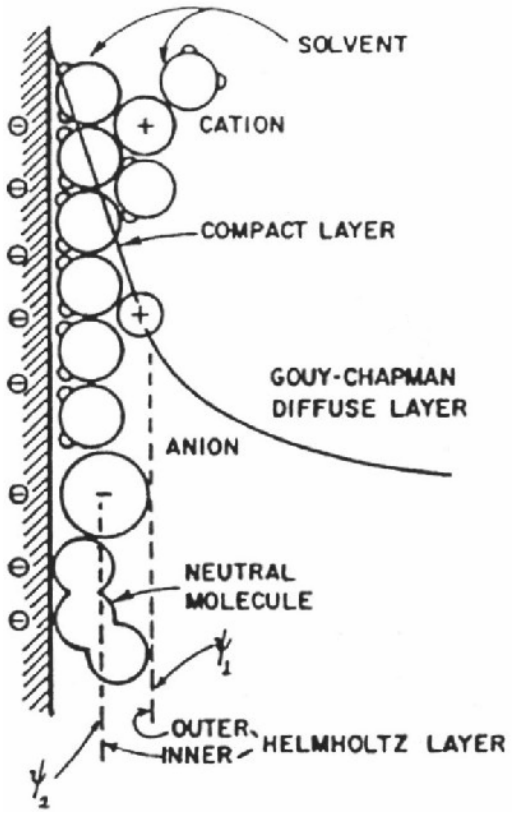

Figure 1.4. Grahame Model (Reproduced from reference 11)

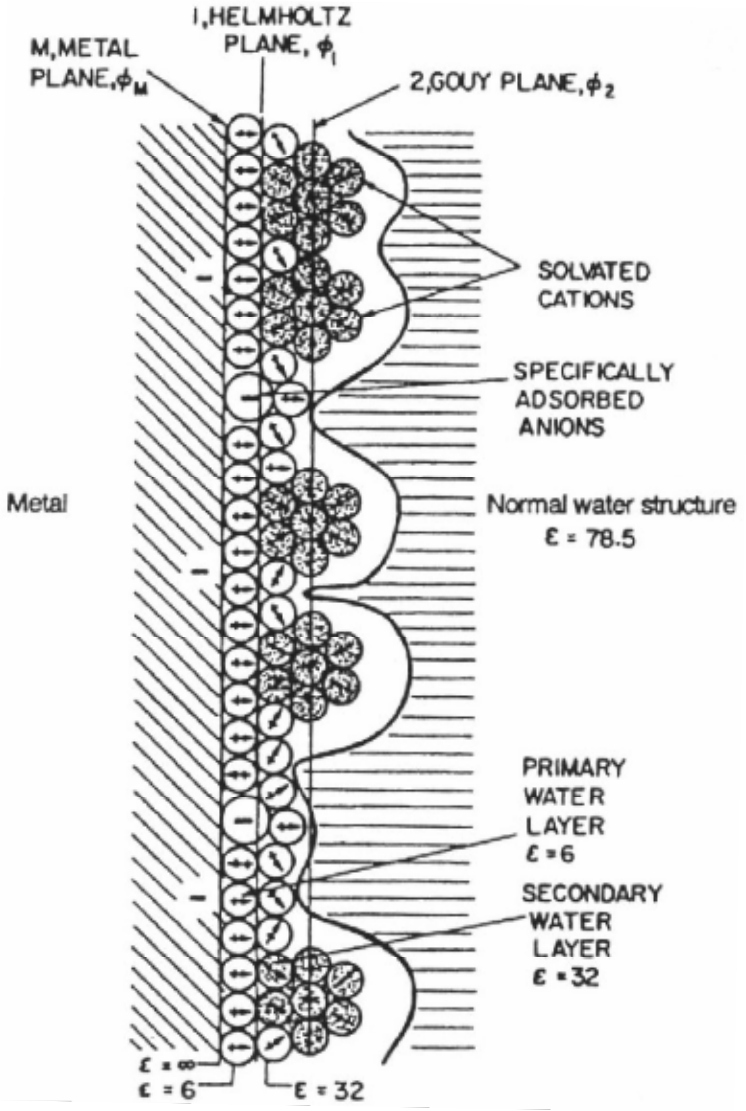

Figure 1.5. Model of Bockris, Devanathan and Müller showing presence and orientation of solvent dipoles (Reproduced from reference 11)

The Bockris-Devanathan-Müller Model

Bockris and Potter[12] suggested in 1952 that dipolar properties of water would bring about an oriented layer of water on the electrode, which would contribute to the potential across the interphase. How this layer of oriented water dipoles would influence the properties of the interface was developed by Macdonald[13] and by Macdonald and Barlow[14], Mott and Watts-Tobin[15], and particularly by Bockris, Devanathan, and Müller[16] in the years 1961-1963.

From about 1980 the idea has been developed[17, 18], that the potential-distance relationship for the double layer in the interfacial region, which had usually been seen as undergoing a sharp change at the metal surface, is in fact continuous through it, with the potential reaching a constant value "just inside" the metal (Jellium Model). The distance (≈1 Å) inside the metal in which the potential varies is called the Thomas-Fermi length.

Study of the electrode/electrolyte interface has not reached its end yet and there are reports of new advances brought about by the use of STM, X-ray and optical techniques[19, 20].

1.1.3 Mass Transport Mechanisms in Electrolytes

In order to understand electrochemical reactions and measurements knowledge of the different transport mechanisms for ions in an electrolyte is important. These are *Diffusion*, *Migration and Convection*. Diffusion is due to a concentration gradient, and migration is due to an electric field gradient. Thus, whilst diffusion occurs for all species,

migration affects only charged species. Convection arises from mechanical movement or density differences in liquid phase.

Steady-State Diffusion is described by Fick's first law:

$$J_i = -D_i \frac{\partial c_i}{\partial x} \tag{1.10}$$

where J_i is the flux of species I of concentration c_i in direction x, and $\frac{\partial c_i}{\partial x}$ is the concentration gradient. D_i is the proportionality factor between flux and concentration gradient, known as the diffusion coefficient. The negative sign is used because the flux of species tends to go from high to low concentration, i.e. against the concentration gradient.

In the presence of an applied electric field, equation (1.10) is transformed into

$$J_i = -D_i \frac{\partial c_i}{\partial x} - z_i c_i \frac{F}{RT} \frac{\partial \Phi}{\partial x} \tag{1.11}$$

where the second term on the right-hand side represents migration. Here z_i means the charge of the species i, F the Faraday Constant, R the Gas Constant, T the absolute temperature, Φ the potential, thus $\frac{\partial \Phi}{\partial x}$ the electric field gradient, the driving force of migration. Friction opposes this electric force, depending on the size of the solvated ion, which leads to a maximum velocity for each ion. Different cation and anion velocities give rise to a potential difference, the *liquid junction potential*. Liquid junction potentials can be widely suppressed by using

supporting electrolytes composed of anions and cations of similar mobility.

In many electrochemical measurements and processes migration plays only a minor part due to the use of supporting electrolytes of well-conducting species, which decrease solution resistance, thus lowering the electric field gradient, so that diffusion becomes the main transport mechanism.

Convection can be suppressed by carrying out experiments without moving the electrode or the solution and in a thermostat. In many technical processes, however convection is desired because it enhances mass transport and can be used to influence the surface structure in electrodeposition.

1.1.4 Electrode Kinetics

In an electrode-electrolyte system in dynamic equilibrium, the electrochemical potential will be given by the Nernst equation (equation 1.8) and the anodic and cathodic partial current densities i_a and i_c will equal the so-called exchange current density i_0, thus the measured current density i through the interface will be zero.

$$i_a = -i_c = i_0 \Rightarrow i = i_a + i_c = 0 \qquad (1.12)$$

If an external potential is applied on the system, the electrode and the electrolyte will try to regain equilibrium potentials, which will cause an electric current through the interface.

Now the partial current densities depend exponentially on the overpotential η which is the deviation of the applied potential E from the equilibrium potential E_{eq} (The latter is given by the Nernst equation).

$$\eta = E - E_{eq} \tag{1.13}$$

$$i_a = i_0 e^{\frac{\beta nF}{RT}\eta} \qquad i_c = -i_0 e^{-\frac{(1-\beta)nF}{RT}\eta} \tag{1.14}$$

Inserting equations (1.14) into equation (1.12) gives the *Butler-Volmer Equation*:

$$i = i_0 \left[e^{\frac{\beta F}{RT}\eta} - e^{-\frac{(1-\beta)F}{RT}\eta} \right] \tag{1.15}$$

where β is the symmetry factor, which indicates the formal location of the energy barrier of the electron transfer on the reaction coordinate ($0 \leq \beta \leq 1$).

The above equations apply for single electron transfer processes. The symmetry factor, β, is concerned with the activation of vibrational states, with force constants, and the energy to dissociate bonds. A more general concept is the transfer coefficient, α. In α, also the stoichiometry of the reaction and the succession of steps in the overall reaction are considered. The cathodic, α_c, and anodic transfer coefficients, α_a, are expressed in terms of β[3a]:

$$\alpha_c = \frac{\gamma}{\upsilon} + r\beta \tag{1.16}$$

$$\alpha_a = \frac{n-\gamma}{\upsilon} - r\beta \tag{1.17}$$

$$\alpha_c + \alpha_a = \frac{n}{\upsilon} \tag{1.18}$$

In the expressions for α, ν is the stoichiometric number, that is, the number of times the rate determining step of the reaction takes place for one act of the overall reaction; γ is the stoichiometric factor, the number of equilibrium steps before the rate-determining step. Finally, n is the number of charges passing in one act of the overall reaction and r is the number of charges passing in the rate-determining step. Thus, α can also be defined for multi-electron transfer reactions, whereas β is restricted to single electron transfer.

The Butler-Volmer equation in its more general form, involving the transfer coefficient, α, can be written as:

$$i = i_0 \left[e^{-\frac{\alpha_c F}{RT}\eta} - e^{\frac{\alpha_a F}{RT}\eta} \right] \tag{1.19}$$

The Butler-Volmer equation is often discussed in one of two limits. In the **low-overpotential limit**, near η = 0, where the current density is proportional to the overpotential, the equation can be approximated by

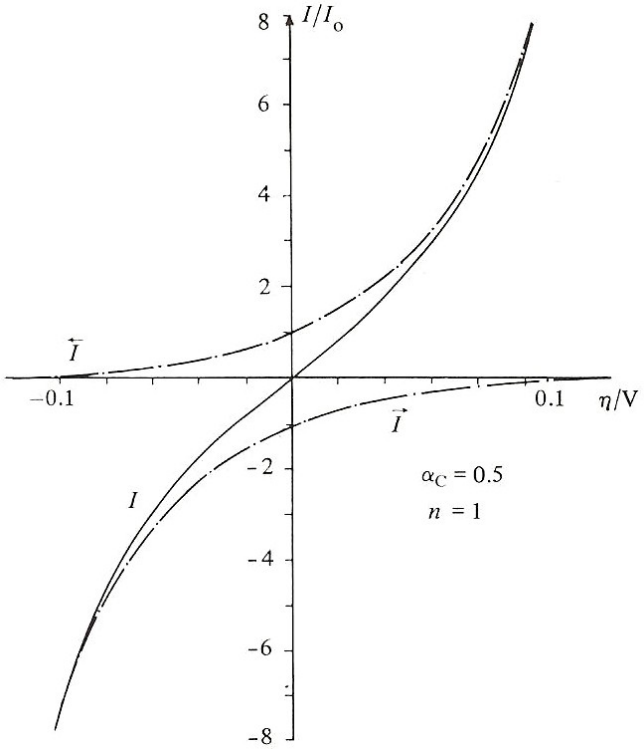

Figure 1.6. Current-voltage characteristics predicted by equation (1.15), showing the contributions from the two partial current densities (Reproduced from reference 4).

a Taylor series, which is terminated after the linear term (this is a variant of Ohm's Law):

$$i = i_0 \frac{F}{RT}\eta \qquad (1.16)$$

In the **high overpotential limit** (positive or negative), one of the partial current densities will be dominant, the other one can be neglected.

At high overpotentials (anodic net current), in logarithmic form:

$$\ln i = \ln i_0 + \frac{\beta F}{RT}\eta \qquad (1.17)$$

At very negative overpotentials (cathodic net current):

$$\ln |i| = \ln i_0 - \frac{(1-\beta)F}{RT}\eta \qquad (1.18)$$

A plot of the logarithm of the current density against the overpotential is called a *Tafel Plot* (Figure 1.7). The slope of the graph gives the value of α and the intercept at η = 0 gives the exchange current density.

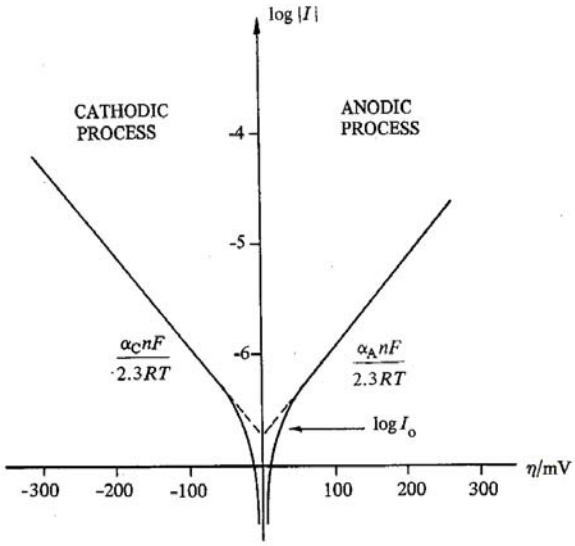

Figure 1.7. A Tafel Plot for the determination of the transfer coefficient, α, from the slope and the exchange current density, i_0, from the extrapolated intercept at η = 0 (Reproduced from reference 4).

The Tafel slopes, b_a and b_c, are given by

$$b_a = \frac{dE}{d\log i} = \frac{2.303RT}{\beta F} \tag{1.19}$$

$$b_c = \frac{dE}{d\log i} = \frac{2.303RT}{(1-\beta)F} \tag{1.20}$$

It has to be noted that the Butler-Volmer (1.15) and Tafel equations (1.17, 1.18) only describe the voltage-current behaviour in an overpotential range where the kinetics of the electron transfer is reaction rate determining. In the case of very high overpotentials, however, all species reaching the electrode interface will be reacted immediately and mass transport to/from the electrode will become rate determining. The slope of the current versus overpotential curve will decrease until a plateau of a limiting current is reached beyond which the current does not change with increasing overpotential any longer. This region of diffusion (mass transfer) control is very useful for determining diffusion coefficients.

A scheme of a system with regions of electron transfer and mass transfer control is pictured in figure 1.8 below.

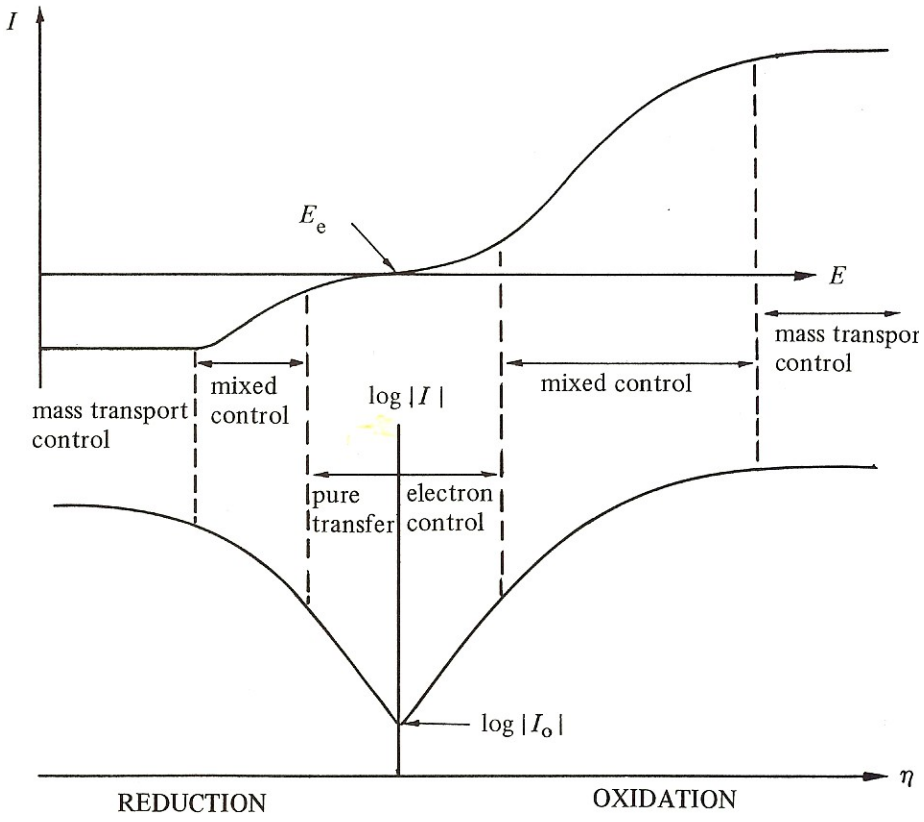

Figure 1.8. Current-overpotential and log current-overpotential characteristics for an electrode reaction with electron and mass transfer regions (Reproduced from reference 4).

1.2 Monolayer Protected Metal Nanoparticles

Metal nanoparticles are not new. A so-called Elixir of Life, a potion made from gold, was discussed, if not actually manufactured, in ancient times. Colloidal gold has been used since Ancient Roman times to colour glass an intense red.

In the 16th century, the alchemist Paracelsus claimed to have created a potion called *Aurum Potabile* (Latin: potable gold).

Paracelsus' work is known to have inspired Michael Faraday to prepare the first pure sample of colloidal gold, which he called 'activated gold', in 1857[21]. He used white phosphorus to reduce a solution of gold chloride. Faraday was the first to recognize that the colour was due to the minute size of the gold particles.

There have been an increasing number of publications on metal nanoparticles in the last ten years. Most of them are dealing with gold, but also silver, copper and other metal nanoparticles have been described. The terms nanoparticles (abbreviated NP), nanoclusters, and nanocrystals have been used for the same material, depending on whether the author wants to stress the particle nature of the material or the fact that these are composed of a limited number of atoms or that the crystalline structure differs from that of the bulk metal structure.

There is no sharp boundary between metal particles and metal nanoparticles but generally, one speaks of nanoparticles at a particle size where the properties begin to deviate from the properties of bulk metal. This typically occurs in the range of less than 10-100 nm, depending on the material and which properties are investigated.

1.2.1 Synthesis of Nanoparticles

There are various methods for the synthesis of metal nanoparticles. Masala and Seshadri give a good overview of the preparation of large volumes of capped nanoparticles of metals as well as other inorganic materials[22].

Metal nanoparticles have been synthesized from the gas phase (e.g. via condensation of metal vapours[23-25]) but most important are

ways from the liquid phase. In general, a soluble salt of the metal in question is reduced by reducing agents such as $NaBH_4$ or sodium citrate to give nanodisperse particles. Recently, also microorganisms (e.g. the fungus fusarium oxysporum[26]) were shown to be able to reduce gold and silver salts intracellular to give nanoparticles of good monodispersity.

The number of atoms in these nanoparticles typically varies from fewer than 100 to approximately 1000. This means a significant part of the atoms will be at the surface of the particles. These will occupy positions of higher energy than that in the bulk. Thus, there will be a tendency of coagulation, which must be overcome in order to keep the particle size within the nanometre domain. Nanoparticles can be stabilized by surface charge but this limits the concentration to very dilute levels and is only possible in aqueous solution. Stabilization with molecular monolayers, in contrast, yields very stable nanoparticles. These are termed monolayer-protected clusters (MPC)[27, 28].

1.2.1.1 Gold

Citrate Reduction

In 1951, nearly a hundred years after Faraday's experiments, Turkevitch reproduced Faraday's results and prepared stable red gold dispersions by the use of trisodium *citrate*[29]. In 1973, Frens showed it was possible to control the resulting particle size ranging from 16 – 150 nm simply by varying the amount of the citrate reducing agent

used in the reaction[30]. He as well characterized the particles using electron microscopy.

In this method, the nanoparticles are stabilized via ion charge. As the gold ions are being reduced, they lose their positive charge that keeps them separated from neighbouring ions. It is believed that the gold atoms are not all completely reduced[29]. They form spherical particles surrounded by a ring of negative surface charge, probably in the form of $AuCl_2^-$ ions:

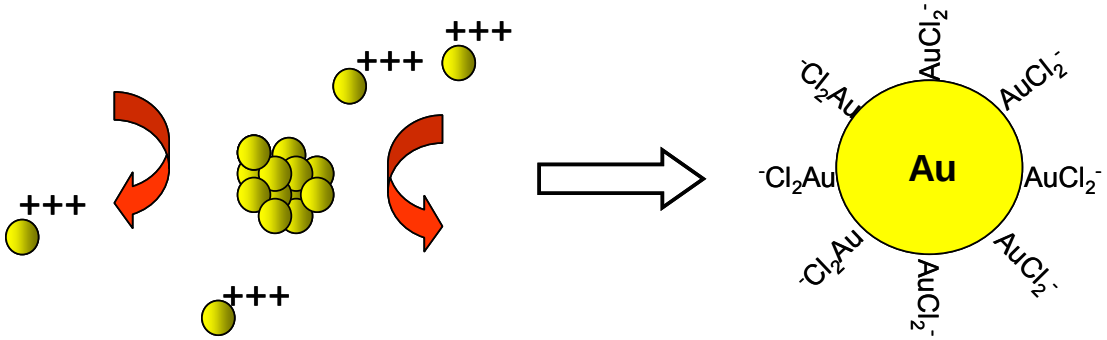

Figure 1.9. Ionic stabilization of gold nanoparticles (Adapted from reference 31)

The charge of the stabilizing ions is believed to be dependent on the reaction conditions. In the reducing environment of the reaction mixture, the ions are negative. The ions provide an electrostatic repulsive stabilizing force against Van der Waals attractions, thus inhibiting aggregation, thereby keeping the gold nanoparticles within the nanometre-size domain.

Recently, a practical preparation of sodium 3-mercaptopropionate-stabilized AuNPs was reported in which simultaneous addition of citrate salt and an amphiphile surfactant was adopted. The size could be controlled by varying the stabilizer/gold ratio[32].

Thiocyanate Reduction

This method was developed by Baschong[33]. The procedure is quite simple. A potassium carbonate solution is added to a solution of $HAuCl_4$ in water, followed by addition of aqueous KSCN or NaSCN solution. The result is an aqueous dispersion of thiocyanate protected gold nanoparticles, where the sulphur of the thiocyanate is bonded to the gold.

The gold nanoparticles produced by this method have a size ranging from 4 – 5 nm, in solution they show yellow-brown colour, but they are less stable than the ones produced by the citrate route and show aggregation upon prolonged exposure to light. The AuSCN sol forms protein-gold complexes and can be used for staining of biological materials for electron microscopy.

Phosphine Complexation

This is no synthesis technique of its own but phosphine complexation can be used to make previously formed nanoparticles more resistant to salts and other aggregation-inducing compounds[34, 35]. Repeated addition of aqueous phosphine ligand solution and precipitation with NaCl, followed by centrifugation, provides the gold nanoparticles with some extra durability in salt solutions, or biological buffers. This technique was developed out of the desire to manipulate gold nanoparticles in biological systems.

Another approach involves the reduction of $HAuCl_4$ by sodium borohydride in the presence of triphenylphosphine (PPh_3) to phosphine protected gold nanoparticles. The reaction is conducted in a two-phase system of water and toluene with tetraoctylammonium bromide as phase transfer agent, like in the Brust synthesis. The reaction path is outlined in equation (1.21).

$$HAuCl_4 + 3\ PPh_3 \rightarrow AuCl(PPH_3) + O{=}PPh_3 + PPh_3 + 3\ HCl \rightarrow Au_{101}(PPh_3)_{21}Cl_5 \quad (1.21)$$

Ligands other than the ones described above involving phosphanes[36], amines[37], selenides, and tellurides[38] have been used successfully as well.

Monolayer Protection

As mentioned before, nanoparticles aggregate the easier, the smaller their size. Thus, there is a need to find ways to stabilize them better than it can be done with ionic stabilization and complexation. The idea is to protect and isolate the particles from the solvent by formation of a well-ordered monolayer of molecules on the particle surface. Brust took advantage of the affinity of thiol functional groups of gold metal and used straight-chained, aliphatic thiol molecules as "surfactants"[39]. By reducing a gold salt with $NaBH_4$ in a two-phase system, Brust found that the nucleation and growth of the gold nanoparticles was controlled by the presence of the surrounding thiols:

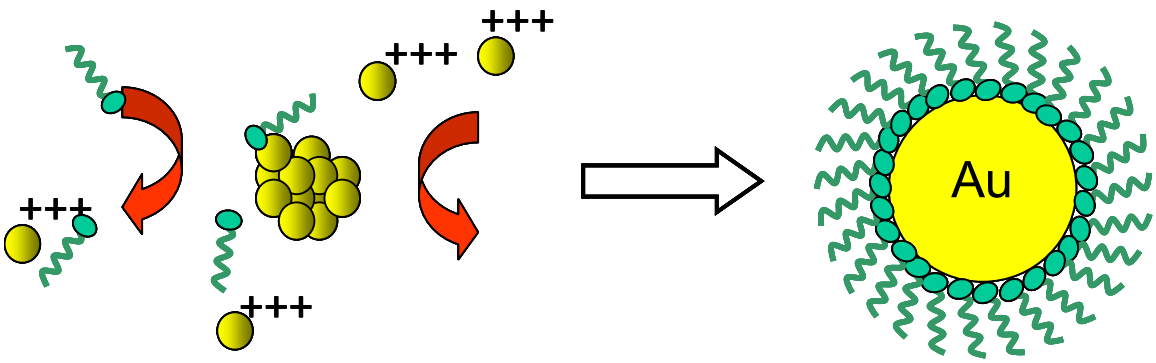

Figure 1.10. Monolayer protection of gold nanoparticles (Adapted from reference 31).

The nanoparticles produced by this method have diameters in a range of 1.5 to 5.2 nm[40, 41]. The particle size can be controlled by varying the gold-to-thiol ratio[42]. Their solutions' colour is very dark brown, almost black. Due to the hydrophobic layer of aliphatic hydrocarbon chains, thiolate-protected nanoparticles are insoluble in polar organic solvents and water but well soluble in non-polar solvents like toluene, pentane, and chloroform and can be further purified by gel-filtration chromatography[39]. Despite the small particle size, they are stable on air for several months and can be dried, stored as a powder, and redissolved, without apparent change of properties[43].

This method of metal nanoparticles synthesis is not limited to hydrophobic products. By using thiols with hydrophilic end groups, water-soluble nanoparticles were obtained. Typical ligands include tiopronin[44], hydroquinone[45], 4-hydroxythiophenol[46], glutathione[47], mercaptobenzoic acid[48, 49] and cysteine[50].

Due to the good stability of gold nanoparticles and the noble character of gold, their synthesis was developed earlier than that of

other metal nanoparticles[51]. A good variety of reducing agents can be used and inert gas atmosphere is not necessary, contrary to less noble metals, many of which are air sensitive in nanodisperse form and require stronger reducing agents, which again demand exclusion of oxygen.

1.2.1.2 Silver

For the preparation of silver nanoparticles very often methods analogous to gold were developed. A suitable salt, usually $AgNO_3$ or silver acetate is reduced in solution in the presence of a stabilizer[51]. The Brust synthesis was employed on silver as well, with $NaBH_4$ as reducing agent[52] and alkanethiols as protecting agent. Among various other reducing agents reported are sodium citrate[53], potassium bitartrate[54], ascorbic acid[55], dimethyl formamide[56] and alcohols[57, 58]. Stabilizing ligands other than alkanethiols such as aniline[53], polivinylpyrrolidone[58] and Bunte salt (S-dodecylthiosulfate)[59] were described. Also thermal decomposition of an Ag^+-oleate complex leads to monodispersed nanocrystallites, with a diameter of 9.5±0.7 nm[60].

Highly symmetric silver nanocubes of dimensions from 50 to 100 nm were obtained via a synthesis involving reduction of silver nitrate with ethylene glycol as reducing agent and solvent and polyvinylpyrrolidone as a capping agent[61].

1.2.1.3 Copper

There are only few synthetic routes reported for copper nanoparticle reduction in solution. One approach is the thermal decomposition of the Cu (II) precursor [$Cu(ODH(Me)CH_2NMe_2)_2$] in hot coordinating solvents (hexadecylamine, tri-n-octylphosphine oxide) which results in well-defined, spherical particles of about 7.5 nm[62].

Reverse micelles were used to form nanosized metallic copper particles[63]. With increasing water content, the size of the particles obtained increased from 2 to 10 nm and upon further increase of water content copper oxide particles were formed instead.

Synthesis of copper nanoparticles protected by alkanethiolate monolayers was also reported, using superhydride in tetrahydrofuran as the reducing agent and copper nitrate as the copper source[64]. However, apart from small nanoparticles of 1-2 nm, also large (>15 nm) crystals were formed.

Strong agglomeration was also observed in an attempt to prepare Cu nanoparticles by refluxing copper acetate with ethanol in the presence of polyvinylpyrrolidone and addition of magnesium metal[58].

In all of these methods inert gas atmosphere had to be used in order to obtain copper nanoparticles instead of copper oxide. The resulting particles, even with protecting ligand layer, had to be stored under inert gas and on air they degraded within days.

1.2.2 Self-Assembled Monolayers (SAMs)

Self-assembled monolayers, SAMs, are formed when surfactant molecules spontaneously adsorb in a monomolecular layer on surfaces. Two of the most widely studied systems of SAMs are gold - alkanethiolate monolayers and alkylsilane monolayers (the latter will not be discussed here).

The first gold-alkanethiolate monolayer was produced by Allara and Nuzzo at Bell Laboratories in 1983[65]. They realized the utility of combining a relatively inert gold surface with a bifunctional organic molecule in well-ordered, regularly oriented array.

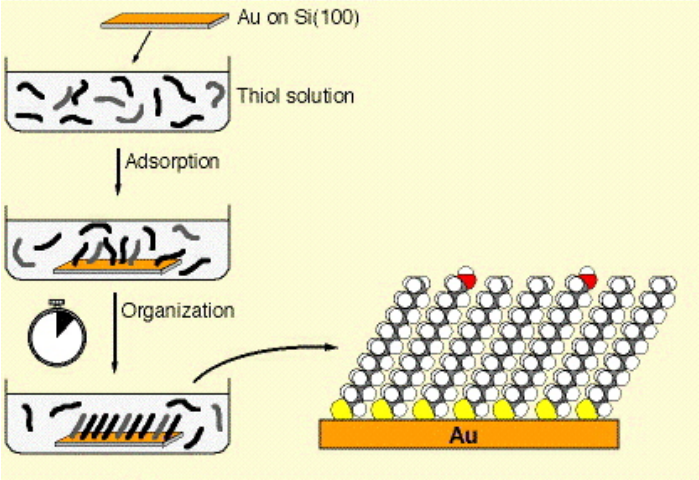

Figure 1.11. Preparation of SAMs. The substrate, Au on Si, is immersed into an ethanol solution of the desired thiol(s). Initial adsorption is fast (seconds); then an organization phase follows which should be allowed to continue for >15 h for best results. A schematic of a fully assembled SAM is shown to the right. (Reproduced from reference 66)

Gold-thiol monolayers are stable when exposed to air. They are also quite facile to produce. A gold surface is immersed into a 2mM solution of ethanolic alkanethiol for a period of hours to days. Even though a self-assembled monolayer forms very rapidly on the substrate, it is necessary to use adsorption times of 15 h or more to obtain well-ordered, defect-free SAMs. Multilayers do not form, and adsorption times of two to three days are optimal in forming highest-quality monolayers.

Mixed monolayers may be formed if the ethanolic solution of T-functionalized alkylthiols contains two or more different thiols.

The tail group that provides the functionality of the SAM can be widely varied. CH_3-terminated SAMs are commercially available; other functional groups can be synthesized, providing almost infinite possibilities of variation. In addition, chemical modification of the tail group is entirely possible after formation of the SAM, expanding the available range of functionalities even further.

Reactivity of monolayers varies substantially from analogous solution reactions[67]. Due to the close proximity of the alkyl chains, interchain reactions, also known as intrafilm reactions, can occur. Reaction kinetics can vary widely from those observed in bulk solution. Often, heterogeneous kinetics is observed.

SAMs have been thoroughly characterized using a large number of techniques such as infrared spectroscopy, ellipsometry, studies of wetting by different liquids, X-ray photoelectron spectroscopy, electrochemistry, and scanning probe measurements. It has been shown that SAMs with an alkane chain length of 12 or more methylene units form well-ordered and dense monolayers on Au(111) surfaces. The thiols are believed to attach primarily to the threefold hollow sites of the gold surface, losing the hydrogen in the process and forming a

(√3×√3)R30° overlayer structure (shown in Figure 1.8). The distance between pinning sites in this geometry is 5.0 Å, resulting in an available area for each molecule of 21.4 $Å^2$. Since the van der Waals diameter of the alkane chain is somewhat too small (4.6 Å) for the chain to completely occupy that area, the chains will tilt, forming an angle of approximately 30° with the surface normal. In contrast, SAMs formed from alkanethiol-type (and dithiol-type) surfactants on silver or copper substrates are not appreciably tilted[68, 69].

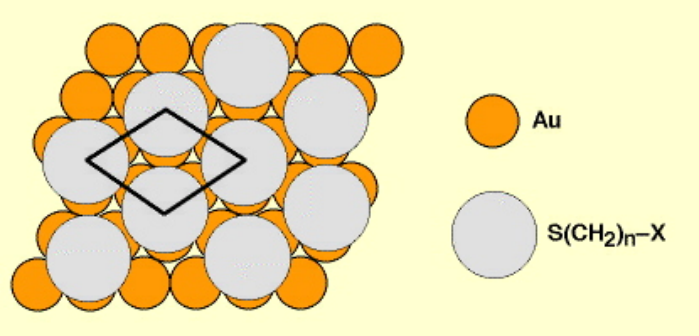

Figure 1.12. A schematic model of the (√3×√3)R30° overlayer structure formed by alkanethiolate SAMs on Au(111) (Reproduced from reference 66)

On the Au (100) surface, the SAM has a square array of ligands, which is rotated relative to the underlying gold layer[69]. An equal number of on-top and 4-fold hollow sites are occupied (Figure 1.13 b). The S-S spacing is 4.54 Å, which means that the packing density on Au (100) is greater than on Au (111). The methyl groups are at different heights due to the two kinds of adsorption sites and XRD studies established a rather complex, distorted hexagonal chain packing.

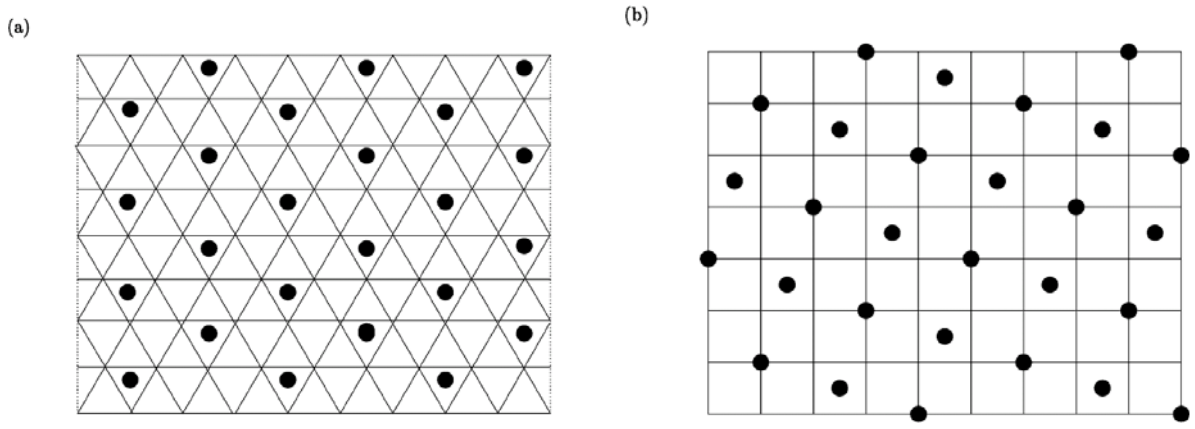

Figure 1.13. Arrangement of thiol molecules on bulk gold surfaces. (a) Au (111) surface, (b) Au (100) surface. The lines connect the gold atoms on the surface and the dots represent the positions of the sulphur groups of the ligands. (Reproduced from ref. 70)

The Au-thiolate bond is strong - homolytic bond strength 167 kJ/mol[69] - and contributes to the stability of the SAMs together with the van der Waals forces between adjacent methylene groups, which amount to 6-7.5 kJ/mol. The latter forces add up to significant strength for alkyl chains of 10-20 methylenes and play an important role in aligning the alkyl chains parallel to each other in a nearly all-trans configuration. At low temperatures, typically 100 K, the order is nearly perfect, but even at room temperature there are only few gauche defects, concentrated to the outermost alkyl units.

The ligand group on the metal core is often called "thiolate" to consider the loss of the hydrogen from the thiol. However, this does not mean the thiolate would be ionic. On the contrary, the Au-S bond is of covalent nature.

The *reaction mechanism* of the thiolate layer formation on gold (and other metals) is not fully clarified yet. There are two possibilities

described in the literature[69, 71 - 74] for the question of the elimination of the hydrogen from the thiol either as a proton or as a neutral hydrogen species:

a) An oxidative addition of the S-H bond to the gold surface, followed by a reductive elimination of the hydrogen and formation of hydrogen molecules, without any electron transfer at the interface, as shown in equation (1.22):

$$Au + RS - H \rightleftharpoons RS - Au + \frac{1}{2} H_2 \qquad (1.22)$$

This theory is backed by the fact that calculated values of ΔG_{ads} for the adsorption following equation (1.12) is closer to the experimentally determined values (ΔG_{ads} = -23±2kJ/mol for n-$C_{18}H_{37}SH$ adsorption onto gold and ΔG_{ads} = -18±1kJ/mol for n-$C_8H_{17}SH$)[71]. With adsorption of thiol from the gas phase, hydrogen gas evolution was reported[73, 74].

b) An anodic reaction, involving electrochemical electron transfer steps:

$$Au + RS - H \rightleftharpoons RS - Au + H^+ + e^- \qquad (1.23)$$

It was shown that the rate and extent of adsorption of thiol onto gold and silver can be influenced by applying an external potential to the substrate, by addition of a redox couple to the solution and by changing the solution pH, all of which favour the idea of an electrochemical process with electron transfer involved[72].

1.2.3 Structure of Monolayer Protected Clusters

Alkanethiolates can adsorb onto gold nanoparticles and form monolayer-protected gold clusters, MPCs. The reactivity of these 3D molecules is quite different from that of planar SAMs. Due to the curvature of the gold core, the chain density of the monolayer decreases as the chain radiates from the core.

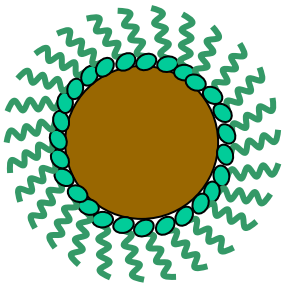

Figure 1.14. Schematic picture of a metal nanoparticle with an adsorbed self-assembled monolayer.

The surface coordination of thiol molecules on finite metal crystallites can differ from that on bulk surfaces, depending on cluster size and geometry. The MPC ligand coverage is in the range of 50 % or more, which is larger than the 33% (ligand/surface Au atom) coverage characteristic of 2D SAMs on Au(111) faces[75]. Theoretical calculations show that this high coverage results from larger ligand/Au binding ratios on core edges and vertexes[43, 76].

It was shown in calculations[70] that surface protection effects by thiol ligands can be considerable and can result in changes in the order of stability between different structural isomers. The most stable

structures of metal nanoparticles were found in simulations and experiments to be of fcc-like cuboctahedral or truncated octahedral or of icosahedral or decahedral geometries, among which the truncated cuboctahedron is the predominant structural motif[51]. The number of atoms per core tends toward closed shell structures ("magic numbers").

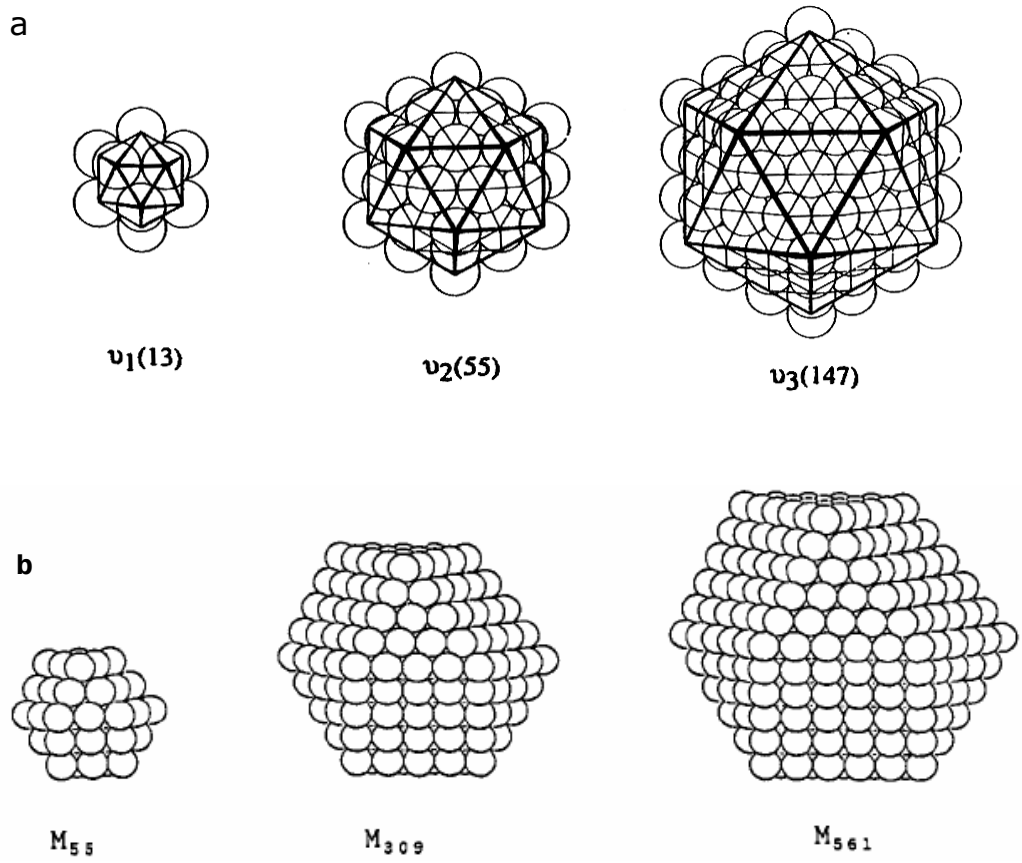

Figure 1.15. (a) The first three members of the ν_n icosahedral closed shell clusters (n = 1, 2, 3). (Reproduced from reference 77)
(b) The truncated octahedral magic numbers 55 (n = 2), 309 (n = 3), and 561 (n = 4). (Reproduced from reference 78)

1.2.4 Reactions of MPCs

The properties of monolayer protected clusters can be modified by ligand exchange or reactions on the molecule end groups, leading to a wide range of applications. Another alternative that leads to functionalized MPCs is the use of functionalized ligands or mixtures of ligands[79] in the synthesis of the clusters, as mentioned in chapter 1.2.1.1 (This path is usually taken for the preparation of water-soluble nanoparticles).

The clusters themselves show self-assembling behaviour to form 2D or 3D lattices resulting from either ligand layer interaction or crosslinking via difunctional molecule layers.

Ligand Exchange

Place-exchange of ligands is a key step to MPC functionalization. As an example, alkanethiol (RS) protected nanoclusters can be functionalized with R'S groups via exchange of ligand groups:

$$x(R'SH) + (RS)_m M \rightarrow x(RSH) + (R'S)_x (RS)_{m-x} M \qquad (1.24)$$

M is the metal core, x and m are the stoichiometric numbers of new and original ligands, respectively. The rate and equilibrium of reaction (1.24) are controlled by factors such as the feed mole ratio of R'SH to RS, their relative steric bulk, and R versus R' chainlengths[80].

It was shown in studies of ligand place-exchange dynamics[81] that

(1) The exchange has a 1:1 stoichiometry, which means one original ligand molecule is replaced by one new ligand molecule and the overall number of occupied adsorption sites stays unchanged.
(2) The mechanism is associative (as opposed to dissociative).
(3) The displaced ligand is found in solution as a thiol.
(4) The reaction does not involve disulphides or oxidized sulphur species.

The rate of place-exchange decreases with an increase in the size of the entering ligand and the chain length of the protecting monolayer.

The time-dependent rate of place-exchange was interpreted as reflecting a hierarchy of different core surface binding sites with associated susceptibility to place-exchange (vertexes, edges >> terraces).

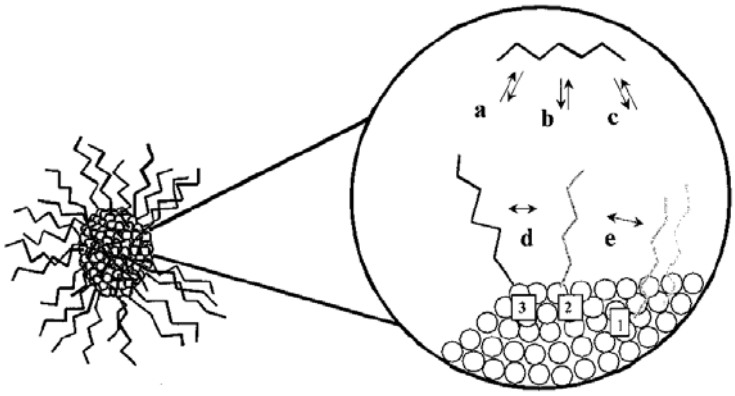

Figure 1.16. (a) Exchange of vertice thiolates (3) with solution thiol; (b) exchange of edge and near-edge thiolates (2) with solution thiol; (d) surface migration among vertice and edge thiolates; (e) surface migration among edge, near-edge, and terrace thiolates. The metal sites are labelled as: (1) terrace core sites, (2) edge and near-edge core sites, and (3) vertice sites (Reproduced from reference 81).

Interior terrace sites are nearly nonexchangeable. There is also evidence of slow surface migration. The migration depends on the presence of sites that are either vacancies or that exhibit a variable thiolate coordination number.

Reactions of ω-Functional Groups

Functional groups on the outermost portion of the MPC ligand sphere can undergo many synthetic transformations.

S_N2 reactions of mixed monolayer MPCs containing ω-bromoalkanethiolates exhibit reactivities similar to those for primary halogen alkane monomers and very different from analogous reactions on 2D SAMs, which shows the steric effects in MPC reactivity[43]. Even ω-bromo sites "buried" in the monolayer are reactive, reflecting a monolayer disorder.

A large variety of further reactions on the ligand end groups is possible, e.g. coupling, as well as polymerizations. Some of the possibilities are outlined in Figure 1.14.

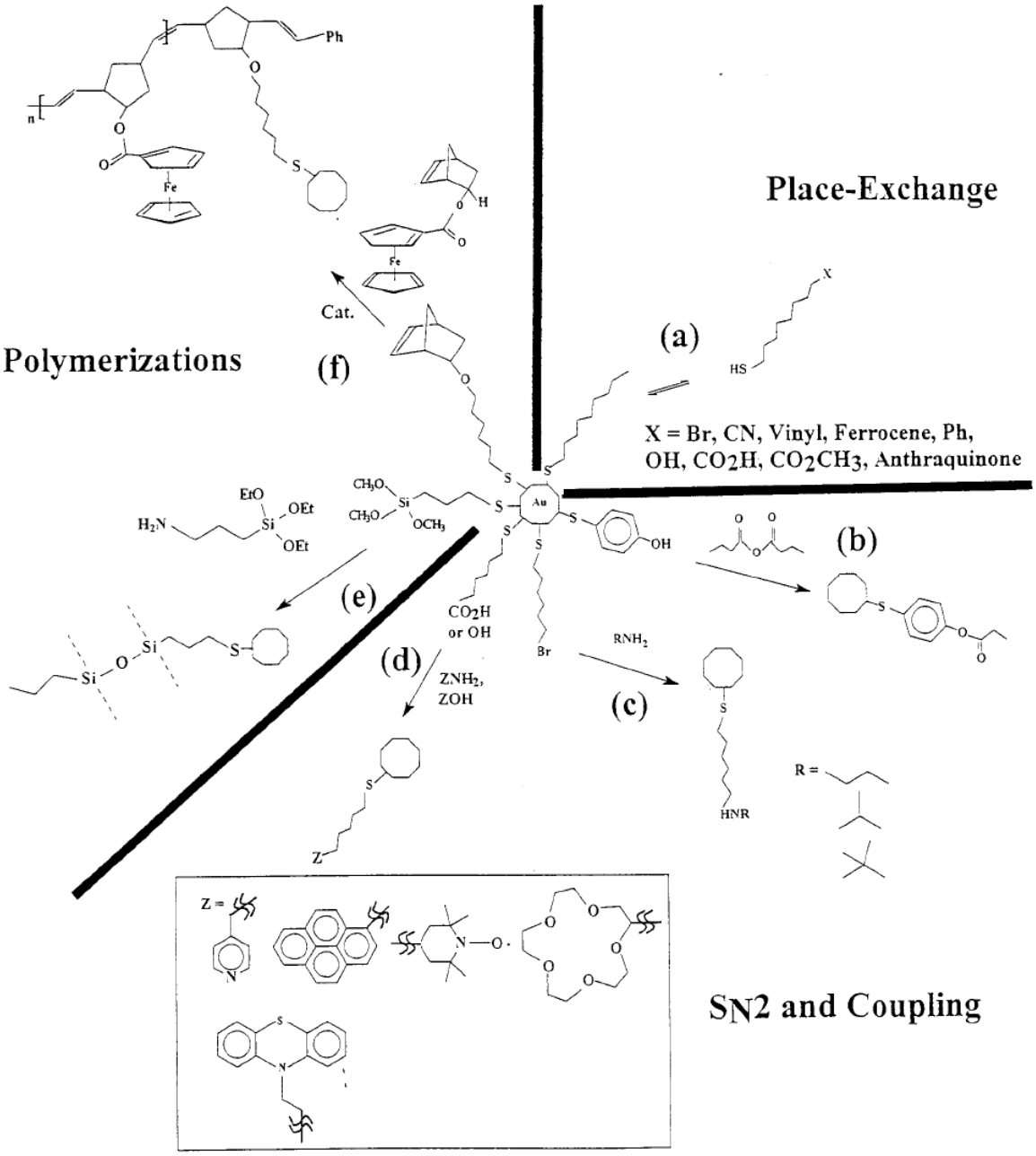

Figure 1.14. Reactions on MPCs. (a) Place exchange, (b) reaction of p-mercaptophenol with propionic anhydride, (c) S_N^2 reaction of ω-bromoalkanethiolated MPCs with primary alkylamines, (d) amide and ester coupling reactions, (e) siloxane formation reactions, and (f) transition-metal-catalyzed ring-opening metathesis polymerization (ROMP) (Reproduced from reference 43).

Self-Assembling of MPCs

A striking feature of thiol-stabilized metal nanoparticles is their tendency to form highly ordered two-dimensional hexagonal superlattices spontaneously in a fully reversible process simply by allowing the slow evaporation of the organic solvent on a suitable substrate. The interparticle spacing is to some extend adjustable with molecular precision by the choice of alkane thiol ligands of different chain length[51]. It has also been demonstrated by X-Ray diffraction techniques that the nanoscale periodicity extends to three dimensions. Bilayers[82] and crystallites of nanocrystals of a size of several tens of micrometers have been observed[83].

A prerequisite for the formation of superlattices of MPCs is the availability of particles that are uniform in size and shape. Nanoparticles produced by the Brust route are usually approximately sphere-shaped and have narrow size distributions, which can be further narrowed by fractional precipitation or extraction[84].

Self-assembling of monolayer-protected gold nanoclusters onto a gold electrode surface via surface-active peripheral thiol groups was reported, resulting from a ligand exchange reaction where thiol ligands were partly displaced with dithiols[85, 86].

1.3 Applications of MPCs

Due to the wide range of nanoparticles properties, which can be tailored easily through synthesis conditions and reactions on the ligand shell, there are manifold applications, part of which are already realized, others still in development or only proposed yet. This section will only give a short overview to show some examples of what is possible.

Catalysis

Gold is very chemically inert and resistant to oxidation. However, AuNP supported on Co_3O_4, Fe_2O_3, or TiO_2 are highly active catalysts[40, 87], under high dispersion, for CO[88] and H_2 oxidation, NO reduction, water-gas shift reaction, CO_2 hydrogenation, and catalytic combustion of methanol.

For homogeneous catalysis, appropriate catalytic groups can be anchored to the ligand shell.

Optics

Films of gold or silver nanoparticles exhibit strong optical anisotropy if they are aligned into parallel rows. Light polarized parallel to the rows will be absorbed as if it were passing through a continuous thin metal film, whereas light polarized perpendicular to the rows will be

transmitted. This effect can be exploited for *polarizing filters* and for *displays*. Dirix and co-workers formed polyethylene foils containing elemental silver nanoparticles and aligned the particles by drawing of the films[89]. These films exhibited a colour that was strongly dependent on the polarization direction of the incident light. The perceived colour of the transmitted light was yellow if polarized perpendicular to the rows, and red if polarized in parallel.

Glasses containing metal nanoparticles show *nonlinear optic properties* and can be used to change the wavelength of laser light. The nanoparticles can be synthesized in the glass by ion implantation and where found to grow through an Ostwald ripening mechanism controlled by diffusion in the glass[40].

Electronic Devices

Monolayer protected metal nanoclusters show a single electron transfer behaviour (Coulomb blockade) where electrons can tunnel through the ligand shell, thereby changing the charge state of the metal core. Charge transfer is only possible when certain core potentials are reached and the result is a staircase-like current-potential correlation of current steps depending on the core potential. This phenomenon was investigated in this work and it is described more detailed in chapter 3.

The single electron transfer behaviour of MPCs is thought to be useful for the design of nanosized *capacitors* and *single-electron transistors*, leading to molecular electronics[90]. Schiffrin and co-workers have demonstrated an electrochemically addressable nano-switch, which consists of a single gold particle attached to a gold surface via a

small number of dithiol molecules containing a redox-active viologen moiety[91]. It was shown by in situ STM that the electron transfer between the gold substrate and the gold nanoparticles depended strongly on the redox-state of the viologen, which could be switched electrochemically.

Furthermore, it is perceived to be possible to construct a memory *storage device* based on the presence or the absence of a single electron on a nanoparticle[68].

Nanotechnology

Research in self-assembling metal nanostructures has been and will be a very important aspect of the *bottom-up* approach to nanosized fabrication, which focuses on assembly techniques of nanosized structures to build nano-devices, as opposed to the *top-down* approach which is based on miniaturization of existing objects. The challenge to design and prepare three-dimensional objects of precisely controlled geometry remains an important goal of future research efforts and a larger repertoire of construction strategies, as well as a more profound understanding of the processes involved will bring about a host of new applications.

Sensors

Thin films of MPCs have shown to change their electrical conductivity rapidly and reproducibly in the presence of organic vapours[92, 93]. This

effect is due to the reversible swelling of the material upon gas absorption, which causes the spacing between the metal cores to increase. The electron hopping conductivity in these materials depends very sensitively on this distance, thus the absorption of organic vapour leads to a strong decrease in electrical conductivity. This phenomenon has been used for the development of novel *gas sensors*[94].

Metal nanoclusters have been used to set up a variety of *biosensors* transducing biorecognitive interactions into optical signals[95]. The reason for this choice is their enormously high extinction coefficient that outperforms e.g. conjugated chromophores at least 100 to 1000 times based on molar concentrations. By use of cluster-based assays, it is possible to visualize the binding of biomolecules at a given surface by a bound layer of ligand-modified metal clusters via either cluster-enhanced absorption or emission.

DNA-MPC Assemblies

Conjugates of nanoparticles and oligonucleotides are of great current interest because of the potential use of the programmability of DNA base pairing to organize nanocrystals in space and the multiple ways of providing a signature for the detection of DNA sequences[96, 97]. Possible applications are expected to be in the fields of biosensors, disease diagnosis, and gene expression.

References

1. C. M. A. Brett, A. M. Brett, *Electrochemistry. Principles Methods and Applications*, Oxford University Press, Oxford, 1993
2. P. Atkins, J. de Paula, *Atkins' Physical Chemistry*, Oxford University Press, Oxford, 2002
3. J. O'M. Bockris, S. U. M. Khan, *Surface Electrochemistry. A Molecular Level Approach*, Plenum Press, New York, 1993

3a. chapter 3, p. 277

4. Southampton Chemistry Group, *Instrumental Methods in Electrochemistry*, Wiley, New York, 1985
5. A. J. Bard, L. R. Faulkner, *Electrochemical Methods. Fundamentals and Applications*, 2nd ed., Wiley, New York, 2001
6. C. H. Haman, W. Vielstich, Elektrochemie, Wiley-VCH, Weinheim, 1998
7. H. L. v. Helmholtz, *Wied. Ann.* **7** (1879) 337
8. G. Gouy, *Chim. Phys.* **9** (1910) 457
9. O. Stern, *Z. Elektrochem.* **30** (1924) 508
10. D. C. Grahame, *Chem. Rev.* **41** (1947) 441
11. B. E. Conway, *http://electrochem.cwru.edu/ed/encycl/art-c03-elchem-cap.htm*, 2003, visited 25-4-2005
12. J. O'M. Bockris, E. C. Potter. *J. Chem. Phys.* **20** (1952) 614
13. J. R. Macdonald, *J. Chem. Phys.* **22** (1954) 1857
14. J. R. Macdonald, C. A. Barlow, *J. Chem. Phys.* **36** (1962) 3062
15. N. F. Mott, R. J. Watts-Tobin, *Electrochim. Acta* **4** (1961) 79
16. J. O'M. Bockris, M. A. V. Devanathan, K. Müller, *Proc. Roy. Soc.* **A274** (1963) 55
17. J. P. Badiali, M. L. Rosinberg, J. Goodisman, *J. Electroanal. Chem.* **130** (1981) 31
18. W. Schmickler, *Chem. Phys. Lett.* **99** (1983) 135
19. A. J. Bard, *J. Phys. Chem.* **97** (1993) 7147
20. M. J. Weaver, *J. Phys. Chem.* **100** (1996) 13079
21. M. Faraday, *Philos. Trans. R. Soc. London* **147** (1857) 145
22. O. Masala, R. Seshadri, *Annu. Rev. Mater. Res.* **34** (2004) 41
23. K. Sattler, J. Mühlbach, E. Recknagel, *Phys. Rev. Lett.* **45** (1980) 821
24. S. Lin, M. T. Franklin, K. J. Klabunde, *Langmuir* **2** (1986) 259
25. S. Stoeva, K. J. Klabunde, C. M. Sorensen, I. Dragieva, *J. Am. Chem. Soc.* **124** (2002) 2305
26. P. Mukherjee et al., *Chem. Bio. Chem.* **5** (2002) 461
27. A. C. Templeton, M. J. Hostetler, C. T. Kraft, R. W. Murray, *J. Am. Chem. Soc.* **120** (1998) 1906

28. A. C. Templeton, M. J. Hostetler, E. K. Warmoth, S. Chen, C. M. Hartshorn, V. M. Krishnamurthy, D. E. Forbes, R. W. Murray, *J. Am Chem. Soc.* **120** (1998) 4845
29. J. Turkevitch, J. Hillier, P. C. Stevenson, *Disc. Farad. Soc.* **11** (1951) 55
30. G. Frens, *Nature (London) Phys. Sci.* **241** (1973) 20
31. B. Yuhas, *http://nanonet.rice.edu/research/ben_res_manual_files/A%20Practical%20Guide%20to%20Gold%20Nanocrystal%20Synthesis.doc* (2003), visited 11-5-2005
32. T. Yonezawa, T. Kunitake, *Colloids Surf. A.* **149** (1999) 193
33. W. Baschong, J. M. Lucocq, J. Roth, *Histochem.* **83** (1985) 409
34. C. J. Loweth, W. B. Caldwell, X. Peng, A. P. Alivisatos, P. G. Schultz, *Angew. Chem. Int. Ed.* **38** (1999) 1808
35. W. W. Weare, S. M. Reed, M. G. Warner, J. E. Hutchison, *J. Am. Chem. Soc.* **122** (2000) 12890
36. G. Schmid, A. Lehnert, *Angew. Chem. Int. Ed. Engl.* **28** (1989) 780
37. D. V. Leff, L. Brandt, J. R. Heath, *Langmuir* **12** (1996) 4723
38. M. Brust, N. Stuhr-Hansen, K. Nørgaard, J. B. Christensen, L. K. Nielsen, T. Bjørnholm, *Nano Lett.* **1** (2001) 189
39. M. Brust, M. Walker, D. Bethell, D. J. Schiffrin, R. Whyman, *J. Chem. Soc., Chem. Commun.* (1994) 801
40. M. C. Daniel, D. Astruc, *Chem. Rev.* **104** (2004) 293
41. A. C. Templeton, J. J. Pietron, R. W. Murray, P. Mulvaney, *J. Phys. Chem. B* **104** (2000) 564
42. D. V. Leff, P. C. Ohara, J. R. Heath, W. M. Gelbart, *J. Phys. Chem.* **99** (1995) 7036
43. A. C. Templeton, W. P. Wuelfing, R. W. Murray *Acc. Chem. Res.* **33** (2000) 27
44. A. C. Templeton, S. Chen, S. M. Gross, R. W. Murray, *Langmuir* **15** (1999) 66
45. H. Hong, W. Park, *Langmuir* **17** (2001) 2485
46. S. Chen, *Langmuir* **15** (1999) 7551
47. T. G. Schaaff, F. Knight, M. N. Shafigullin, R. F. Borkman, R. L. Whetten, *J. Phys. Chem. B.* **102** (1998) 10643
48. S. R. Johnson, S. D. Evans, R. Brydson, *Langmuir* **14** (1998) 6639
49. C. J. Ackerson, P. D. Jadzinsky, R. D. Kornberg, *J. Am. Chem. Soc.* **127** (2005) 6550
50. K. Naka, H. Itoh, Y. Tampo, Y. Chujo, *Langmuir* **19** (2003) 5546
51. M. Brust, C. J. Kiely, *Coll. Surf. A Phys. Eng. Asp.* **202** (2002) 175
52. S. He, et al., *Langmuir* **17** (2001) 1571
53. Y. Tan, Y. Li, D. Zhu, *J. Coll. Int. Sci.* **258** (2003) 244

54. Y. Tan, X. Dai, Y. Li, D. Zhu, *J. Mater. Chem.* **13** (2003) 1069
55. I. Sondi, D. V. Goia, E. Matijević, *J. Coll. Int. Sci.* **260** (2003) 75
56. I. Pastoriza-Santos, L. M. Liz-Marzán, *Langmuir* **15** (1999) 948
57. C. Lee, C. Wan, Y. Wang, *Adv. Funct. Mater.* **11** (2001) 344
58. S. Ayyappan, R. S. Gopalan, G. N. Subanna, C. N. R. Rao, *J. Mater. Res.* **12** (1997) 398
59. Y. Shon, E. Cutler, *Langmuir* **20** (2004) 6626
60. D. K. Lee, Y. S. Kang, *ETRI J.* **26** (2004) 252
61. Y. Sun, Y. Xia, *Science* **298** (2002) 2176
62. J. Hambrock, R. Becker, A. Birkner, J. Weiß, R. A. Fischer, *Chem. Commun.* (2002) 68
63. I. Lisiecki, M. P. Pileni, *J. Am. Chem. Soc.* **115** (1993) 3887
64. S. Chen, J. M. Sommers, *J. Phys. Chem. B* **105** (2001) 8816
65. R. G. Nuzzo, D. L. Allara, *J. Am. Chem. Soc.* **105** (1983) 4481
66. I. Engquist, *http://www.ifm.liu.se/applphys/ftir/sams.html* (1996), visited 17-5-2005
67. V. Chechik, R. M. Crooks, C. J. M. Stirling, *Adv. Mater.* **12** (2000) 1161
68. J. H. Fendler, *Chem. Mater.* **13** (2001) 3196
69. A. Ulman, *Chem. Rev.* **96** (1996) 1533
70. N. T. Wilson, R. L. Johnston, *Phys. Chem. Chem. Phys.* **4** (2002) 4168
71. D. S. Karpovich, G. J. Blanchard, *Langmuir* **10** (1994) 3315
72. S. Chon, W. Paik, *Phys. Chem. Chem. Phys.* **3** (2001) 3405
73. T. Pradeep, N. Sandhyarani, *Pure Appl. Chem.* **74** (2002) 1593
74. N. Sandhyarani, T. Pradeep, *Int. Rev. Phys. Chem.* **22** (2003) 221
75. W. D. Luedtke, U. Landman, *J. Phys. Chem. B* **102** (1998) 6566
76. M. J. Hostetler et al., *Langmuir* **14** (1998) 17
77. D. L. Feldheim, C. A. Foss, *Metal Nanoparticles. Synthesis, Characterization, and Applications*, Marcel Dekker, 2002, p.62
78. G. Schmid, et al., *Pure & Appl. Chem.* **62** (1990) 1175
79. H. Choo, E. Cutler, Y. Shon, *Langmuir* **19** (2003) 8555
80. R. S. Ingram, M. J. Hostetler, R. W. Murray, *J. Am. Chem. Soc.* **119** (1997) 9175
81. M. J. Hostetler, A. C. Templeton, R. W. Murray, *Langmuir* **15** (1999) 3782
82. J. Fink, C. J. Kiely, D. Bethell, D. J. Schiffrin, *Chem. Mater.* **10** (1998) 922
83. R. L. Whetten et al., *Acc. Chem. Res.* **32** (1999) 397
84. J. F. Hicks, A. C. Templeton, S. Chen, K. M. Sheran, R. Jasti, R. W. Murray, *Anal. Chem.* **71** (1999) 3703
85. S. Chen, *J. Phys. Chem. B.* **104** (2000) 663

86. S. Chen, R. W. Murray, *J. Phys. Chem. B* **103** (1999) 9996
87. G. Schmid, M. Bäumle, M. Geerkens, I. Heim, C. Osemann, T. Sawitowski, *Chem. Soc. Rev.* **28** (1999) 179
88. N. Lopez et al., *J. Cat.* **223** (2004) 232
89. Y. Dirix, C. Bastiaansen, W. Caseri, P. Smith, *Adv. Mater.* **11** (1999) 223
90. G. Schmid, *Chem. Unserer Zeit* **39** (2005) 8
91. D. I. Gittins, D. Bethell, D. J. Schiffrin, R. J. Nichols, *Nature* **408** (2000) 67
92. H. Wohltjen, A. W. Snow, *Anal. Chem.* **70** (1998) 2856
93. S. D. Evans, S. R. Johnson, Y. L. Cheng, T. Shen, *J. Mater. Chem.* **10** (2000) 183
94. R. R. Smardzewski, N. L. Jarvis, A. W. Snow, H. Wohltjen,
95. C. Mayer, N. Stich, T. Schalkhammer, G. Bauer, *Fresenius J. Anal. Chem.* **371** (2001) 238
96. C. A. Mirkin, R. L. Letsinger, R. C. Mucic, J. J. Storhoff, *Nature* **382** (1996) 607
97. A. P. Alivisatos, et al., *Nature* **382** (1996) 609

2. Methods and Experimental

In this chapter the applied synthesis methods and procedures are described as well as the basic principles of the characterization methods.

The chemicals used were bought in p. a. quality from Sigma-Aldrich, water was purified by a Millipore® system and solvents were of technical quality, obtained from the Trinity College Hazardous Materials Facility.

2.1 Synthesis of Gold Nanoparticles

The synthesis described here is based on the method developed by Brust and Schiffrin[1]. The reaction consists of a phase transfer of the $AuCl_4^-$ from the aqueous phase to the organic phase with tetraoctylammonium bromide (TOAB) (equation 2.1).

$$Au\,Cl_4^-(aq) + N(C_8H_{17})_4^+(C_6H_5Me) \rightarrow N(C_8H_{17})_4^+\,AuCl_4^-(C_6H_5Me) \qquad (2.1)$$

The following step is the reduction of $AuCl_4^-$ to AuNP in the presence of thiol (equation 2.2). The source of electrons is BH_4^-.

$$m\overset{III}{Au}\,Cl_4^-(C_6H_5Me) + nC_{12}H_{25}SH(C_6H_5Me) + 3me^- \rightarrow$$
$$\rightarrow 4mCl^-(aq) + (Au_m)(C_{12}H_{25}SH)_n(C_6H_5Me) \qquad (2.2)$$

0.354g $HAuCl_4 \cdot 3H_2O$ was dissolved in 30 mL water (30 mM) and added to a solution of 2.187 g of TOAB $[CH_3(CH_2)_7]_4NBr$ (i.e. 4x excess) in 80 mL toluene (50 mM). This two-phase system was stirred

several minutes until the water phase lost its yellow colour and the organic phase turned orange, showing the transfer of the $AuCl^-$ into the organic phase. Hereby the tetraoctylammonium bromide acts as a phase transfer agent.

0.2 mL of dodecanethiol (4x excess) was added and the colour got a bit lighter.

A freshly prepared solution of 0.378 g $NaBH_4$ (10x excess) in 25 mL water (0.4 M) was introduced which caused gas evolution and a colour change to brown-black. The mixture was stirred for 3 hours at room temperature, after which the water phase was removed in a separation funnel.

The stages of the reaction are shown in the picture below.

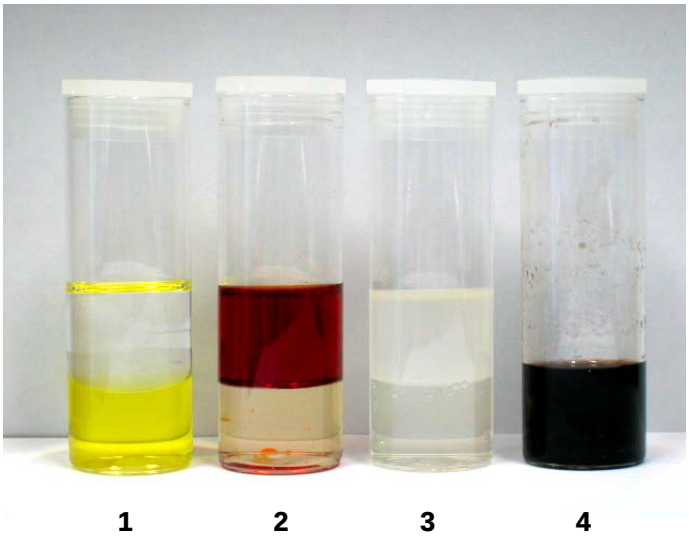

Figure 2.1. The four stages of gold nanoparticle synthesis: **(1)** TOAB in the clear toluene phase above $AuCl_4^-$ in the aqueous phase. **(2)** Within several minutes' stirring, the $AuCl_4^-$ is transferred to the organic phase which turns red. **(3)** After addition of dodecanethiol, the organic phase turns white due to formation of a complex. **(4)** The organic phase, after addition of aqueous $NaBH_4$ solution and removal of the aqueous phase. The black colour originates from the gold nanoparticles in solution.

For the workup two different ways were open:

1) The organic phase was evaporated to 10 mL in a rotary evaporator, 400 mL ethanol added and left to precipitate at -18°C over night. The black precipitate was transferred with a pipette into centrifuge tubes and centrifuged for approx. 10 min at 4,000 rpm. The supernatant was removed and the precipitate dissolved in toluene.

2) The organic phase was washed with water 3 times and then was evaporated to near dryness in a rotary evaporator. The solid residue was washed into a beaker with 250 mL of ethanol and kept at -18°C over night to precipitate. The black precipitate was filtered under suction with blue band filter paper, washed with copious amounts of ethanol and acetone and dried by sucking air through the filter cake.

This procedure is easier to perform than the centrifugation in option 1 and full removal of excess thiol is ensured better.

The yield was typically around 214 mg (86%) black, waxy solid (via workup option 2) or ≈ 100 mL dark brown solution in toluene (workup route 1). These solutions were stable on air for several months.

2.2 Synthesis of Silver Nanoparticles

The method undertaken was very similar to the synthesis of the gold nanoparticles but due to the different stoichiometry of the reduction of Ag^+ to Ag different amounts of reactants had to be used.

0.153 g $AgNO_3$ was dissolved in 30 mL water. 2.187 g TOAB (Tetraoctylammonium bromide) was dissolved in 80 mL toluene. The

two clear solutions were united and stirred vigorously for several minutes; no colour change was observed but a white precipitate of presumably AgBr formed in the aqueous phase (Br^- from TOAB). This observation was also mentioned by other researchers already[2].

0.2 mL dodecanethiol was added (no colour change). 0.126 g $NaBH_4$ was dissolved in 10 mL Millipore water and added (10x excess). Within seconds the colour of the mixture changed from white over yellow to red-brown and gas evolved. The mixture was stirred for 3 hours, and then the phases were separated in a separation funnel. The organic phase was washed with water 3 times and evaporated to near dryness. The residue was washed into a beaker with 250 mL ethanol and left to precipitate over night at approx. -18°C. In contrast to the gold nanoparticles, the silver nanoparticles did not precipitate fully. They were filtered under suction with blue band filter paper, which did not hold back the entire solid. The filtrate was filtered through the same filter again. This time the filtrate was clear. Filtration took an hour because the filter got blocked by the fine precipitate. The solutions in toluene seemed to be light sensitive. In daylight, partial precipitation and decomposition (layer of silver on glass sample tubes) occurred within two weeks. Protected from light, the solutions were stable for several months.

The stages of the reaction are shown in Figure 2.2 below.

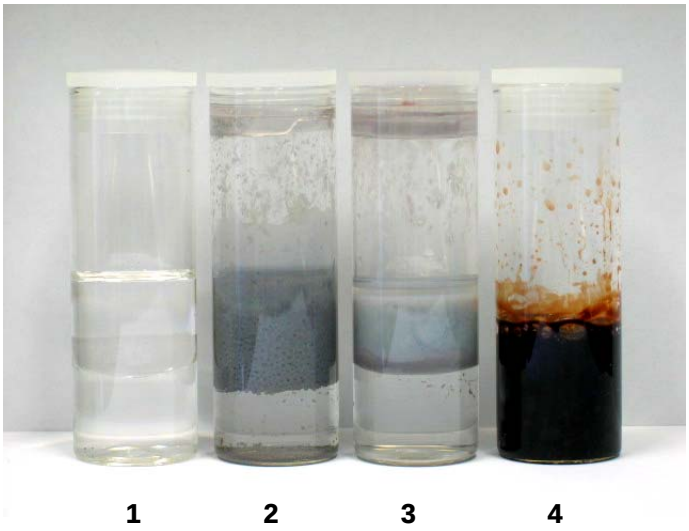

Figure 2.2. The four stages of silver nanoparticle synthesis: **(1)** TOABr in toluene over silver nitrate in water. Both phases are clear. **(2)** When the two-phase system is stirred, a white precipitate of AgBr is formed (very light sensitive, turns grey), which slowly transfers to the organic phase. **(3)** No change upon addition of dodecanethiol. **(4)** After addition of aqueous $NaBH_4$ solution, the organic phase turns brown, indicating the formation of silver nanoparticles.

The assumed reaction path is described by equations (2.3) – the formation of AgBr in the first step – and (2.4) – the reduction to silver nanoparticles (the electrons are donated by $NaBH_4$).

$$Ag^+(aq) + N(C_8H_{17})_4{}^+ Br^-(C_6H_5Me) \rightarrow AgBr_{(s)} \downarrow + N(C_8H_{17})_4{}^+(C_6H_5Me) \qquad (2.3)$$

$$AgBr_{(s)} + me^- + nC_{12}H_{25}SH(C_6H_5Me) \rightarrow (Ag_m)(C_{12}H_{25}SH)_n(C_6H_5Me) + Br^- \qquad (2.4)$$

The yield of this reaction was 118 mg grey solid powder.

2.3 Synthesis of Copper Nanoparticles

It was tried to use the Brust reaction also for the formation of copper nanoparticles.

0.225 g $CuSO_4 \cdot 5\ H_2O$ was dissolved in 30 mL water and 4.374 g TOAB in 160 mL toluene was added. The two phase system was stirred vigorously for several minutes but no colour change occurred, the aqueous phase stayed blue and the organic phase was colourless, which indicates that no phase transfer had taken place.

After addition of 0.2 mL dodecanethiol the toluene phase became cloudy. 0.756 g $NaBH_4$ was dissolved in 50 mL water and added, upon which the water phase turned over brown to black within seconds and strong gas evolution (H_2) was observed. The mixture was stirred for 3 hours, within which the water phase lost its colour entirely and the toluene phase became black (very intense green). The phases separated easily and no precipitation was observed.

The organic phase was washed with water 3 times to remove ionic compounds and evaporated to 10 mL, then mixed with 500 mL ethanol, transferred to a beaker and stored at -18°C for 2 days. The particles precipitated well; brown powder and colourless crystal needles were formed. Both were insoluble in ethanol and acetone. The precipitate was filtered with double blue band filter paper under suction and washed several times with copious amounts of ethanol and acetone, upon which the colourless crystals disappeared.

The remaining brown powder was dissolved in approximately 50 mL toluene. The particles were not stable; they aggregated and precipitated within one week.

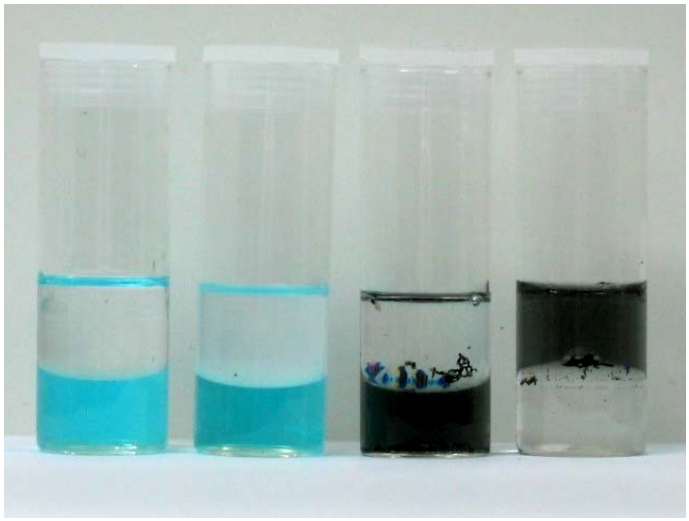

Figure 2.3. The stages of the copper nanoparticle formation. **(1)** The clear TOAB solution in toluene above the blue aqueous phase of copper sulphate solution. The appearance does not change through stirring; no phase transfer of Cu^{2+} is observable. **(2)** Upon addition of dodecanethiol, the organic phase turns cloudy. **(3)** After addition of aqueous $NaBH_4$ solution, the aqueous phase turns black, indicating copper reduction. **(4)** Three hours later: The black particles have transferred to the organic phase, which is black now. The aqueous phase is clear.

Another route which allegedly leads to copper nanoparticles of small size (1-2 nm), reported by Chen and Sommers[3], was tried out as well but failed. This route uses a one-phase system and superhydride® (Lithium triethylboro-hydride, 1 M solution in THF)

0.242 g $Cu(NO_3)_2 \cdot 3\ H_2O$ was dissolved in 4 mL water (blue solution). 1.1 g TOAB in 40 mL freshly distilled THF was added and stirred vigorously. 718 mL dodecanethiol was added and the solution suddenly turned cloudy and a white flaky precipitate was formed. 2 mL superhydride® was added drop by drop via a syringe but no change occurred, except gas evolution. The resulting foamy, white mixture was stirred over night but when still no colour change would indicate

the formation of metal nanoparticles (dark brown colour), the experiment was terminated. Obviously, no reduction had been achieved.

In further experiments it was found out that water is not necessary to dissolve the copper nitrate, as copper nitrate is sufficiently soluble in THF. Water decomposes the superhydride® under hydrogen evolution, and so it was convenient to be able to leave out water at all. Still, the reduction did not work. $NaBH_4$ is only sparingly soluble in THF or ethanol but it reduces copper nitrate to a brown, fluffy precipitate in absence of dodecanethiol. In the presence of dodecanethiol, the same white precipitate as with superhydride® formed, although a successful synthesis of copper nanoparticles by reduction of copper nitrate with sodium borohydride in the presence of alkanethiol in ethanol was reported recently[4].

The problem seemed to lie in a reaction of copper nitrate with dodecanethiol. The white precipitate formed was insoluble in water, ethanol and THF but soluble in toluene, DCM and chloroform, was of lower density than all of these and melted easily upon heating. It could have been a disulfide compound formed by oxidation of dodecanethiol with Cu^{2+}.

The white precipitate also formed when copper nitrate crystals were dropped into dodecanethiol. No reducing agent was added. Brown NO_2 gas evolution was observed and heat was generated. The solution turned red, probably due to formation of a copper complex. The solution lost its colour within hours, probably through oxidation by air.

2.4 Place Transfer (Ligand Exchange)

The reaction was first described by Hostetler, Green, Stokes and Murray[5]. It was applied here to synthesize nanoparticles with ferrocene-terminated alkanethiol ligands.

A nanoparticle solution (in toluene) of known molarity was prepared. First, if the as-prepared nanoparticles were dissolved in toluene, they were dried to constant weight in high vacuum using a water bath for heating. For calculation of the molarity the average particle formula mass had to be derived from the core size (which was determined from TEM measurements). There is a relation between particle core size and number of metal atoms in the core, as described by Hostetler et al[5].

Once the average number of metal atoms per core is known, the formula mass of the core can be calculated.

The mass fraction of the ligand shell can be determined by elemental analysis and the sum of the ligand shell mass and the core mass gives an estimate of the (average) formula mass of the nanoclusters. To be precise, this formula mass (proportional to R^3) is not the average of the cluster mass distribution because it was derived from a size distribution average (R) but the approximation is sufficient because the measured size distributions were relatively symmetrical.

To the nanoparticle solution of known molarity in toluene, a known molar ratio of ferrocenecarboxydodecanethiol, -decanethiol or -octanethiol was added, e.g. a molar ratio of 2:1 ferrocenecarboxyalkanethiol vs. nanoparticles. These compounds are not available on the market and were synthesized by Conchúir Mac Gloinn of Chemistry Department, Trinity College Dublin.

The solution was stirred for 24 hours, then it was evaporated to 10 mL and tried to precipitate through addition of 500 mL ethanol. As precipitation did not occur, the sample was evaporated to dryness and 500 mL ethanol was added again. This time precipitation was successful. The precipitate was filtered, washed with copious amounts of acetone and dissolved in dichloromethane (DCM).

The sample prepared with ferrocenecarboxydecanethiol was instable in DCM and decomposed, covering the flask with a gold layer. The other two samples were stable for months.

2.5 Transmission Electron Microscopy

Transmission electron microscopy (TEM) was conducted on a Hitachi® H-7000 Scanning Transmission Electron Microscope.

Samples were prepared by evaporation of 1 – 2 drops nanoparticle solution in toluene on a holey carbon film supported by a copper grid.

Images were captured at 50,000 to 600,000-fold magnification. (acceleration voltage: 100 kV). The best pictures were obtained at 200,000-fold magnification.

The particle core size was analyzed from the images, using the program UTHSCSA ImageTool Version 3.0 (available free on the web at http://ddsdx.uthscsa.edu/dig/itdesc.html, developed at the University of Texas Health Science Center at San Antonio).

2.6 Elemental Analysis

Elemental Analysis was conducted by Sean Walsh of Trinity College Dublin Centre for Microscopy and Analysis on an Agilent 7500a Inductively Coupled Plasma Mass Spectrometer. Samples were prepared by digestion in aqua regia (gold) or nitric acid (silver). The purpose of the measurements was the determination of trace impurity content of iron and nickel for magnetism measurements conducted in Professor Coey's research group (Physics Department, Trinity College Dublin), but also the gold (silver) content was measured.

2.7 Nuclear Magnetic Resonance

^{1}H Nuclear Magnetic Resonance (NMR) was used to verify that the ligands were bonded to the metal core and for the calculation of ligand exchange ratios in the product of place exchange reactions.

If the sample was dissolved in solvent it was dried first. A small amount of the dry solid was dissolved in $CDCl_3$.

The measurements were conducted by Dr. John O'Brian of Chemistry Department, Trinity College Dublin.

2.8 Electrolyte and Electrode Preparation for Electrochemical Measurements

A 0.05 M solution of tetrabutylammonium perchlorate (TBAP) was prepared as a supporting electrolyte for the electrochemical measurements – 0.427 g TBAP in 25 mL DCM.

5 mL supporting electrolyte was added to 10 mL nanoparticle solution (≈ 10 – 30 μM, solvent: toluene). This was the same for Au, Ag, and Cu.

It is very important that the DCM is free from chloride (a decomposition product if DCM is exposed to light). Chloride precipitates silver nanoparticles as AgCl, thus making any electrochemical measurement impossible. A simple test was conducted before each preparation of the electrolyte as follows: a small amount silver nitrate was dissolved in Millipore® water (not tap water!) in a test tube, and shaken with DCM. Chloride impurities in DCM would show as white precipitate of AgCl in the aqueous phase. Both solutions clear meant the DCM was pure enough for use.

The working electrode consisted of a 1 mm^2 Au disc electrode, the counter electrode was a Pt wire electrode, and the reference electrode was an aqueous Ag/AgCl electrode (3 M KCl).

Before measurements, the gold working electrode was polished for a minute with wet 0.05 micron alumina powder on a polishing pad in a figure 8 pattern, rinsed with Millipore® water, dried with paper, and rinsed with toluene.

The counter electrode was rinsed with toluene prior to measurements.

The vicor tip of the reference electrode was rinsed with Millipore® water, dried with paper, and rinsed with toluene.

The electrochemical cell consisted of a shot glass with a Teflon® cell top with three holes for working, counter and reference electrode.

For rotating disc electrode experiments, a BAS® 100B Electrochemical Analyzer with Rotating Disc Electrode Stand RDE 2 was used. For all other electrochemical measurements, a CHI® 760B Electrochemical Workstation was used.

The setup of the electrochemical cell can be seen in the picture below (Figure 2.4).

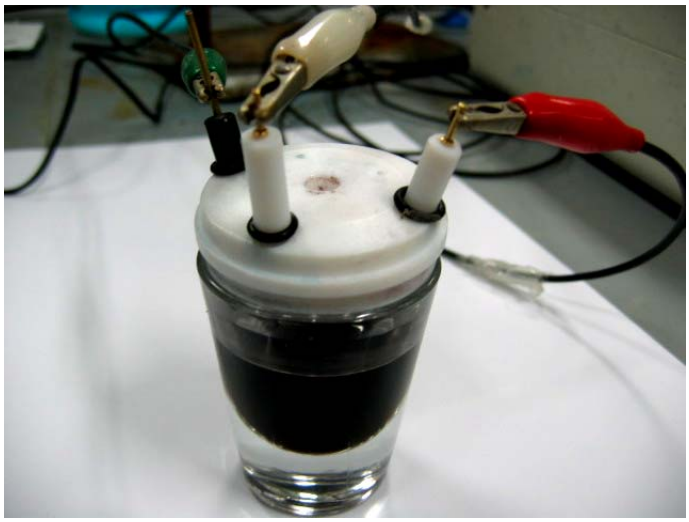

Figure 2.4. The electrochemical cell. Left: working electrode (green clamp), centre: reference electrode (white clamp), right: counter electrode (red clamp).

2.9 Cyclic Voltammetry

2.9.1 Principles

In cyclic voltammetry (CV), the current at a working electrode is monitored as an applied potential is swept up and down at a constant rate between pre-set limits (See figure 2.5). The cell current is recorded as a function of the applied potential (it should be noted, however, that the potential axis is also a time axis). The sweep rates used in conventional experiments range from a few mV s^{-1} up to a few hundred V s^{-1}. This sweep technique is used widely in the area of preliminary mechanistic investigations as well as for the determination of kinetic parameters. An "electrochemical spectrum" indicating the potentials at which processes occur can be rapidly obtained, while from the sweep rate dependence the involvement of coupled homogeneous reactions is readily identified, and other complications such as adsorption can be recognized. Thus it is not surprising that cyclic voltammetry is nearly always the technique of first choice when studying a system for the first time.

The Parameters in cyclic voltammetry are the upper and lower potential limit, the initial potential (which normally lies at either limit or between them), the sweep speed and the sensitivity for the recording of the current.

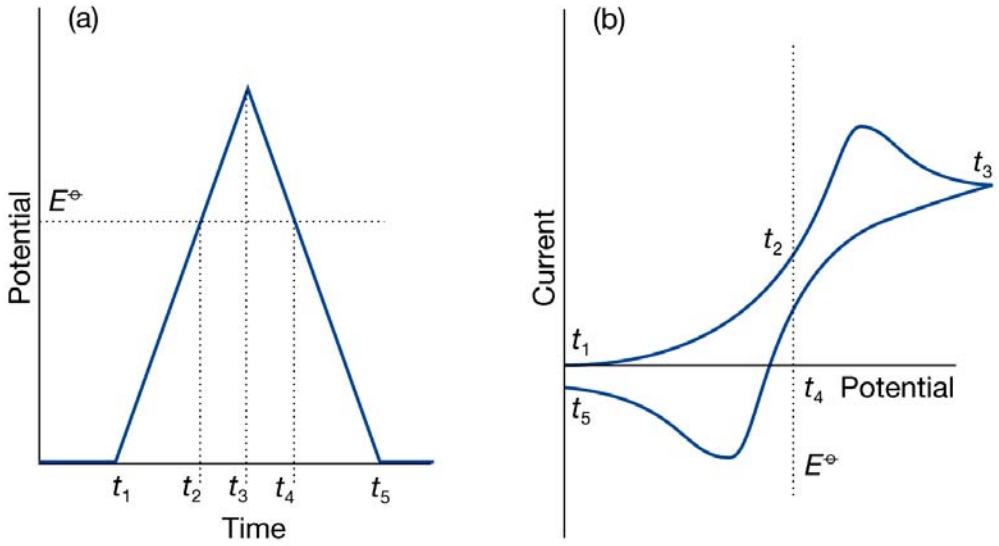

Figure 2.5. (a) Potential-time profile, (b) cyclic voltammogram (Reproduced from reference 7)

In Figure 2.5, a typical triangular potential-time profile and the current response are pictured. At time t_1 the experiment starts at the initial potential and sweeps in positive (i.e. anodic) potential direction. As the potential at time t_2 approaches $E^{\ominus}$ for a solution that contains a reduced component Red, current begins to flow as Red is oxidized. When the potential is swept beyond $E^{\ominus}$, the current passes through a maximum and then falls as all the Red near the electrode is consumed and converted to Ox, the oxidized form. When the potential reaches the upper limit at t_3, the direction of the sweep is reversed. The potential passes through $E^{\ominus}$ at t_4 and current flows in the reverse direction. This current is caused by the reduction of the Ox previously formed near the electrode, which is consumed. The cycle can be terminated at t_5 or more cycles can follow.

The forward and reverse current maxima bracket $E^{\ominus}$, so the species present can be identified. Furthermore, the forward and reverse peak currents are proportional to the concentration of the

redox couple in the solution, and vary with the sweep rate. If the electrode kinetics is reversible, the peak separation is independent of the sweep rate and equal to 59 mV per electron transferred. If the voltammetry is irreversible, the peak separation is greater and increases with increasing sweep rate. If homogeneous chemical reactions accompany the oxidation or reduction of the couple at the electrode, the shape of the voltammogram changes, and the observed changes can give valuable information about the kinetics of the reactions and about the identity of the species present.

2.9.2 Experimental Procedure

The electrolyte and the electrodes were prepared as described in section 2.8. CVs were recorded with different potential limits, most common +/-2 V or +/- 5 V. These wide ranges could be used because the electrolyte was non-aqueous, thus decomposition of the electrolyte did not occur within these potentials (as opposed to aqueous electrolytes which allow only measurements between the potentials of hydrogen and oxygen evolution).

Sweep speed was varied from 5 mV/s to 500 mV/s to find a speed where scan duration was reasonably short and signal/noise ratio in the current measurement was acceptable. A sweep speed of 100 to 200 mV/s proved to give best results, whereas at 500 mV and more noise increased strongly.

For easier recognition of peaks, the derivatives of the spectra could be plotted with the supplied CHI® software.

2.10 Rotating Disc Electrode

2.10.1 Principles

The rotating disc electrode experiment (RDE) is a very popular system for kinetic and mechanistic studies. A disc of the electrode material is surrounded by non-conducting sheath so that the faces of the electrode and the sheath are flush and only the face of the disc electrode is exposed to the electrolyte solution. When the electrode is rotated perpendicular to the face of the disc, a well defined flow pattern is established, as illustrated in figure 2.6.

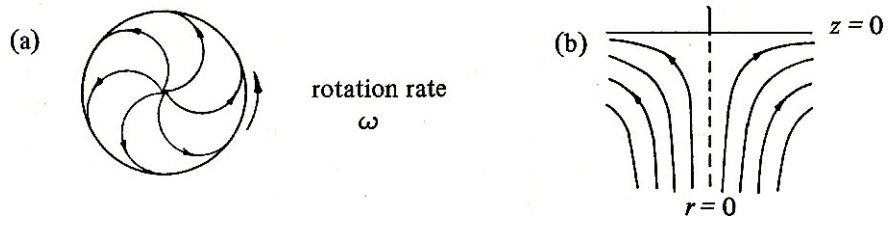

Figure 2.6. Flow pattern created by the rotating disc electrode. (a) Solution flow close to the electrode surface, viewed from below, (b) view from the side showing how the solution is pumped towards the disc, and then thrown outwards. (Reproduced from reference 8)

The great advantage of the rotating disc electrode is its well defined geometry which makes it possible for the concentration profile brought about by the forced convection to be correlated to the system parameters. The concentration gradient of any species perpendicular to the disc plane (i.e. in direction of the z coordinate) depends on the

rotation rate of the disc ω, on the kinematic viscosity of the liquid ν and the diffusion coefficient D. This is can be described by a differential equation (equation 2.5)

$$\frac{\partial^2 c}{\partial z^2} = \frac{-0.51\omega^{\frac{3}{2}}\upsilon^{-\frac{1}{2}}}{D} z^2 \frac{\partial c}{\partial z} \qquad (2.5)$$

The Nernst Diffusion layer model

Near the electrode surface there is a thin layer of electrolyte which has the same rotation speed as the electrode and is not subject to any convection. Thus, in this layer, mass transport is diffusion controlled and under steady state conditions, a linear concentration profile as described by Fick's First Law (equation 1.10) will be established. Far away from the rotating electrode the liquid is at high turbulence, thus the concentration is equal in space and equal to the bulk value. In between these two extremes there is a transition zone. It is helpful to understanding of experiments with a rotating disc electrode to use a model where the continuously varying flow conditions are replaced by an equivalent system where the zones for diffusion and convection have been completely separated (figure 2.7).

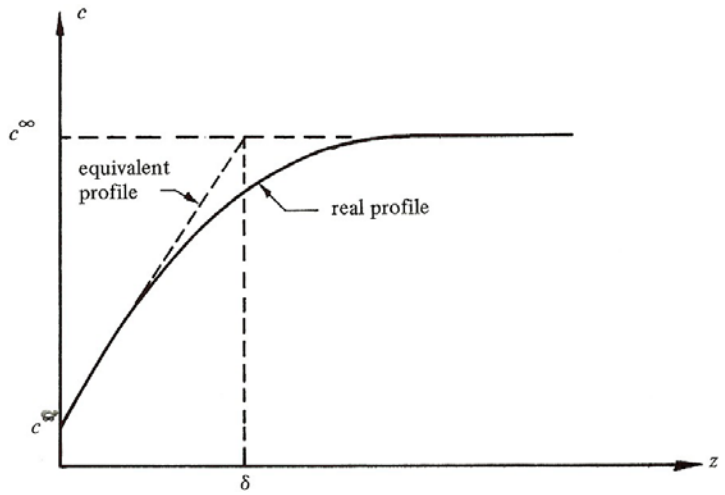

Figure 2.7. Concentration profile for electroactive species according to the Nernst diffusion layer model for transport to a rotating disc electrode (Reproduced from reference 8).

The flux of material to the rotating disc electrode is uniform over the whole surface. Therefore it is possible to discuss the mass transport in a single direction, that perpendicular to the surface (along the z coordinate). It is clear from equation (2.5) that the rate of diffusion to the disc is strongly dependent on the rotation rate of the disc. This is taken into account in the Nernst diffusion layer model by noting that the stagnant layer thickness δ will increase as the rotation rate is increased. A quantitative relationship has been deduced:

$$\delta = \frac{1.61\upsilon^{\frac{1}{6}} D^{\frac{1}{3}}}{\omega^{\frac{1}{2}}} \qquad (2.6)$$

The diffusional flux through the Nernst diffusion layer is given by

$$J = \frac{D(c^{\infty} - c^{\sigma})}{\delta} \qquad (2.7)$$

Here c^{∞} is the bulk concentration and c^{σ} the concentration at the electrode surface (see also figure 2.7). The quotient D/δ can be calculated from the limiting current density i_L (the potential is held at a value where $c^{\sigma} = 0$):

$$\frac{D}{\delta} = \frac{i_L}{nFc^{\infty}} \tag{2.8}$$

For high overpotentials, where the surface concentration of the electroactive species is zero, an equation relating the limiting current density and the rotation rate is found by combining equations (2.6) – (2.8):

$$i_L = 0.62nFD^{\frac{2}{3}}\upsilon^{-\frac{1}{6}}c^{\infty}\omega^{\frac{1}{2}} \tag{2.9}$$

This is also known as the Levich equation. It provides a test that the current is entirely mass transport controlled; a plot of i vs. $\omega^{1/2}$ should be linear and pass through the origin. The slope of such a plot may be used to estimate the diffusion coefficient of the electroactive species.

2.10.2 Experimental Procedure

The electrolyte was prepared as described in section 2.8 with particles carrying the electroactive ferrocene functionality in the ligand shell (obtained via place exchange, see 2.4). On the BAS® 100B Electrochemical Analyzer with Rotating Disc Electrode Stand RDE 2 the rotation rate could be controlled in a range of 0 - 10,000 min^{-1}. CV

scans were run without and with rotation. The rotation speed was kept constant during each scan and a range of 500 – 10,000 min^{-1} was covered with six steps. The scan range chosen was 0 to +1.2 V, to cover the ferrocene redox peak at approx. +0.75 V. The working electrode was made of gold and had an area of 3 mm^2.

2.11 Differential Pulse Voltammetry

2.11.1 Principles

In differential pulse Voltammetry (DPV) a pulsed voltage signal is superimposed on a linear base potential ramp similar to cyclic Voltammetry. The pulse height stays constant and the base potential is swept slowly with time. The current shortly before the pulse and that at the end of the pulse are measured and the difference between these values is recorded as a function of the potential (see figure 2.8).

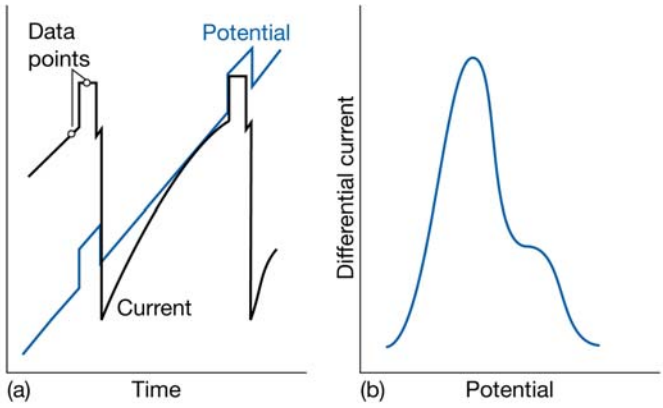

Figure 2.8. Differential pulse voltammetry. (a) Input potential signal (blue) and current response (black), (b) resulting voltammogram. (Reproduced from reference 7)

Since the current is measured well after the application of the pulse, the double layer charging current will have decayed essentially to zero and the current measured will be totally faradaic.

The resulting spectrum is very similar to a derivative of a CV. For example, a step feature in a CV would appear as a peak in a DPV.

2.11.2 Experimental Procedure

The parameters in differential pulse voltammetry are the initial and final potential of the base potential ramp and the potential increment, the pulse amplitude, width and pulse period, the sampling width and the sensitivity. Special attention should be paid that pulse period and sampling width match so that the data points are always taken at the same section of the pulse and base potential.

The electrolyte was prepared as usual. DPV was conducted on all gold, silver and copper samples as synthesized. The potential range was the same as for the CV measurements.

2.12 Chronoamperometry

Chronoamperometry is a potential step technique where the potential of the working electrode is changed instantaneously and the current-time response is recorded. A potential-time profile as shown in figure 2.9 is applied to the working electrode. E_1 is chosen such that no electrode reaction occurs; this is normally the open-circuit potential (OCP). At time t = 0 the potential is instantaneously changed to a new

value E_2, where an electron transfer reaction (oxidation or reduction) occurs at a diffusion controlled rate.

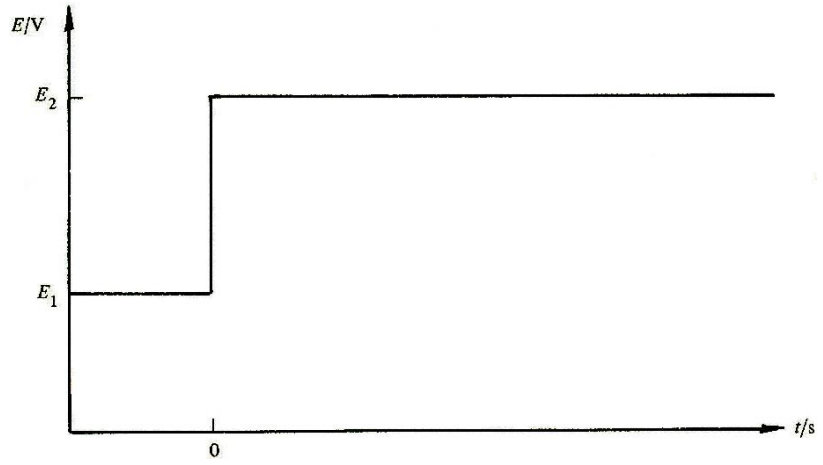

Figure 2.9. The potential-time profile for a single potential step chronoamperometric experiment (Reproduced from reference 8)

Time dependent diffusion through a plane parallel to an electrode surface is described by Fick's 2nd Law

$$\frac{\partial c_i}{\partial t} = D_i \frac{\partial^2 c_i}{\partial x^2} \qquad (2.10)$$

With the appropriate boundary conditions, this differential equation can be solved and gives the Cottrell equation

$$|i| = \frac{nFD_i^{\frac{1}{2}} c_i^{\infty}}{\pi^{\frac{1}{2}} t^{\frac{1}{2}}} \qquad (2.11)$$

A plot of i versus $t^{-1/2}$ should therefore be linear and should pass through the origin, if the reaction is diffusion controlled. The diffusion coefficient D_i of the electroactive species i can be derived from the slope of the straight line.

2.13 A. C. Impedance

From an electrical point of view, an electrode-electrolyte interface can be represented by an equivalent circuit, composed of resistors and capacitors, also called the *Randles equivalent circuit* (See also figure 2.10).

As mentioned before, an electrode-electrolyte interface involves the charged planes of the electrode and the ions in the Helmholtz layer, forming a capacitor. This can be represented by a double layer capacitance C_{dl}. The electrode reaction shows a resistance, parallel to the double layer capacitance, composed of a charge transfer resistance R_{ct} and a Warburg impedance resulting from the mass transport by diffusion. If there is any uncompensated solution resistance R_u between the point at which the potential is measured (the tip of the reference electrode) and the working electrode, this too will appear as part of the measured total impedance. This circuit scheme is pictured below.

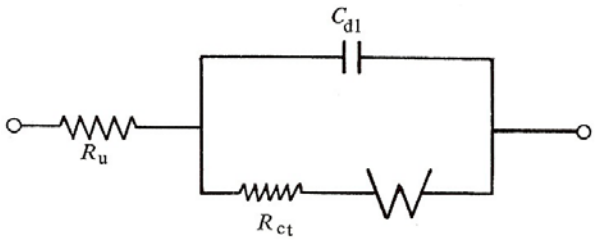

Figure 2.10. Randles equivalent circuit for an electrode reaction with double layer capacitance C_{dl}, charge transfer resistance R_{ct}, Warburg impedance and an uncompensated solution resistance R_u. (Reproduced from reference 8)

With alternating current, potential and current can show a phase difference, which can be represented by an impedance Z, consisting of a combination of resistances and capacitances. This complex resistance consists of a real part Z' and an imaginary part Z''. In a complex plane (Argand) diagram, the imaginary part is plotted versus the real part. The circuit shown in figure 2.7 would give the following diagram:

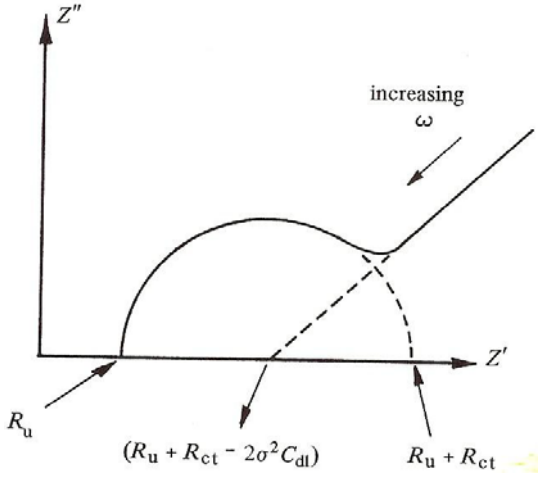

Figure 2.11. Complex plane (Argand) plot for the circuit of Figure 2.10.
(Reproduced from reference 8)

At high frequency ω, the plot shows a semi circle region with the centre on $Z' = R_u + R_{ct}/2$ and a radius of $R_{ct}/2$. In this region, the system is under kinetic control. With the current alternating very fast, impedance is dominated by the double layer charging and charge transfer processes. Diffusion is a much slower process, so the Warburg impedance is negligible in this region.

At low frequency, diffusion plays the leading role and a linear correlation between the imaginary and real impedance is observed, according to equation 2.12:

$$Z'' = Z' - R_u - R_{ct} + 2\sigma^2 C_{dl} \tag{2.12}$$

The slope of this straight line equals unit and the intercept on the real Z' axis is $R_u + R_{ct} - 2\sigma^2 C_{dl}$.

A. C. Impedance measurement is a steady state technique conducted at equilibrium as opposed to sweep techniques like CV or DPV which drive the working electrode potential far from equilibrium. Under this precondition and for a planar diffusion field, the charge transfer resistance R_{ct} and the Warburg coefficient σ are given by

$$R_{ct} = \frac{RT}{nFi_0} \tag{2.13}$$

$$\sigma = \frac{RT}{\sqrt{2}n^2F^2A\sqrt{D}}\left[\frac{1}{c_O^\infty} + \frac{1}{c_R^\infty}\right] \tag{2.14}$$

A is the electrode area and c_O^∞ and c_R^∞ are the bulk concentrations of the oxidized and reduced species, respectively.

R_{ct} is characteristic of the exchange current, i_0 which itself is characteristic of the electron transfer kinetics and its activation barrier (see also chapter 1.1.4). The Warburg coefficient, σ, on the other hand, is related to the Diffusion coefficient, D, and the ion concentrations c_O^∞ and c_R^∞. Thus, from the Warburg region of an A. C. impedance measurement, the diffusion coefficient of the species in solution can be determined.

2.14 UV/VIS Spectroscopy

2.14.1 Principles and Theoretical Background of UV/VIS Spectroscopy of MPCs

Already in ancient times, one of observations with colloidal gold was the red colour, which differs strongly from the colour of elemental gold. Later it was found out that the colour of gold nanoparticles is dependent on size. The colours range from blue over purple and red to brown, as illustrated in the picture below (figure 2.12).

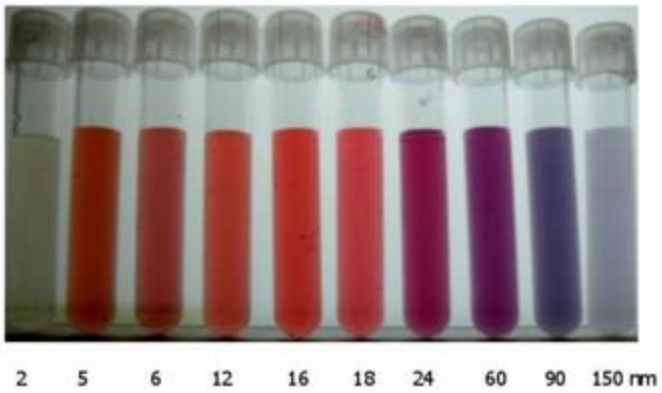

Figure 2.12. Colloidal gold solutions of different nanoparticle sizes show different colours. (Image by Irawati Kandela, Department of Pharmaceutical Sciences, School of Pharmacy, University of Wisconsin-Madison, and Ralph Albrecht laboratory, Department of Animal Sciences)

Also silver and copper nanoparticles show size-dependent colours[9]. The colours originate from a broad absorption band in the visible region of the electromagnetic spectrum. The very intense colour of these metal nanoparticles is absent for the bulk material as well as for the atoms (gas). Its origin is attributed to the collective oscillation of the free conduction electrons induced by an interacting electromagnetic field. These resonances are also denoted as surface plasmons.

UV/VIS spectroscopy is based on light absorption in the UV and visible regions of the electromagnetic spectrum. Absorbance, A, is directly proportional to the path length, x, and the concentration, c_i, of the absorbing species. *Beer's Law* states that

$$A = \varepsilon \, x \, c \qquad (2.15)$$

where ε is a constant of proportionality, called the *molar absorptivity*. It is important to note that absorptivity is a function of the

wavelength. If concentration and path length are known, the spectrum of the absorptivity can be easily deduced from the absorbance spectrum. With an absorbance band in a given colour region, the visible solution colour will be the complementary colour. Metal nanoparticles show very high absorptivity in their absorption bands, so that even very dilute solutions have intense colour and concentrated solutions appear black or brown.

2.14.2 Experimental Procedure

An approximately 40 mg/L nanoparticle solution in toluene or DCM was prepared either by dissolving the solid nanoparticle powder or by dilution of the solution obtained from the synthesis. This concentration was chosen in order for the absorption maximum to be in the range of A = 1. At lower absorption peaks would be very small and flat in the background whereas at too high absorption the detector limit, noise, and light scattering at the cell would falsify the spectrum.

For every sample a background subtraction was conducted by taking a baseline of pure toluene/DCM measured in the same cuvette. The cuvettes used were made of quartz glass and had a path length of 1 cm. They were rinsed with pure toluene/DCM between measurements. Measurements were conducted on a Varian Cary 50 Conc UV/Visible Spectrometer.

Scans were taken in a wavelength range of 300 nm to 700 nm. At wavelengths lower than approximately 300 nm light absorption by the solvent got too strong and at wavelengths exceeding 700 nm no more absorption features were found.

References

1. M. Brust, M. Walker, D. Bethell, D. J. Schiffrin, R. Whyman, *J. Chem. Soc., Chem. Commun.* (1994) 801
2. S. He, et al., *Langmuir* **17** (2001) 1571
3. S. Chen, J. M. Sommers, *J. Phys. Chem. B* **105** (2001) 8816
4. T. P. Ang, T. S. A. Wee, W. S. Chin, *J. Phys. Chem. B* **108** (2004) 11001
5. M. J. Hostetler, S. J. Green, J. J. Stokes, R. W. Murray, *J. Am. Chem. Soc.* **118** (1996) 4212
6. M. J. Hostetler et al., *Langmuir* **14** (1998) 17
7. P. Atkins, J. de Paula, *Atkins' Physical Chemistry*, Oxford University Press, Oxford, 2002
8. Southampton Chemistry Group, *Instrumental Methods in Electrochemistry*, Wiley, New York, 1985
9. P. Mulvaney, *Langmuir* **12** (1996) 788

3. Results and Discussion

3.1 Distribution of the Core Size

The distribution of the nanoparticle core size was determined via TEM. The procedure is described in section 2.5. With TEM, photographs of the nanoparticle samples were taken. The nanoparticle cores show as dark circular spots on the images because of the high electron absorption cross section of the heavy metal core, whereas the hydrocarbon ligand shell is not visible in the TEM images.

The TEM pictures are shown in Figures 3.1-3.3 below.

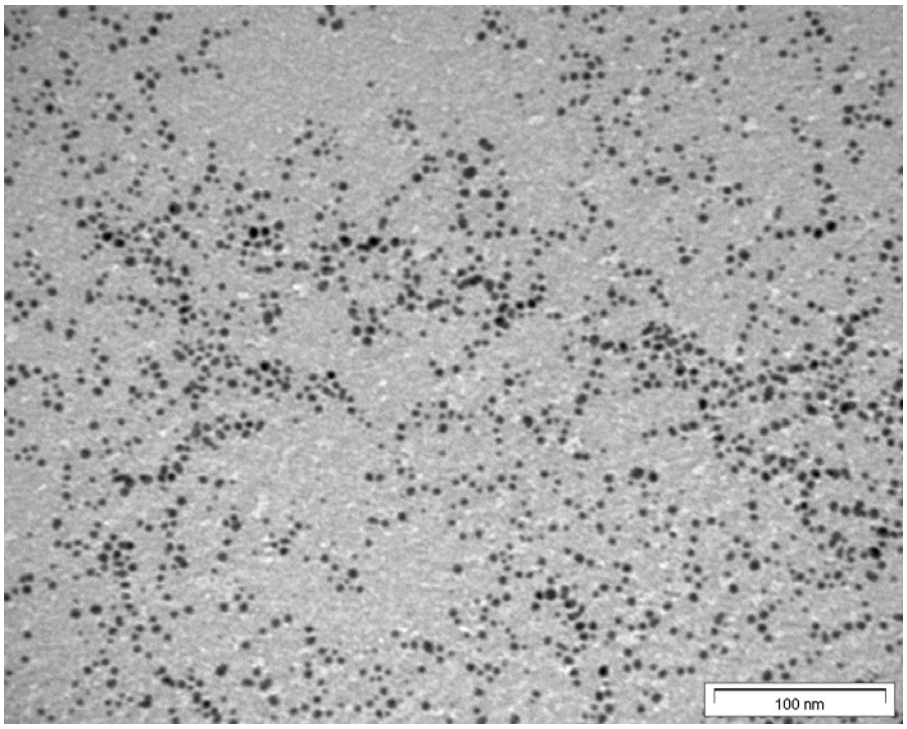

Figure 3.1. TEM image of gold nanoparticle cores (at 200,000x)

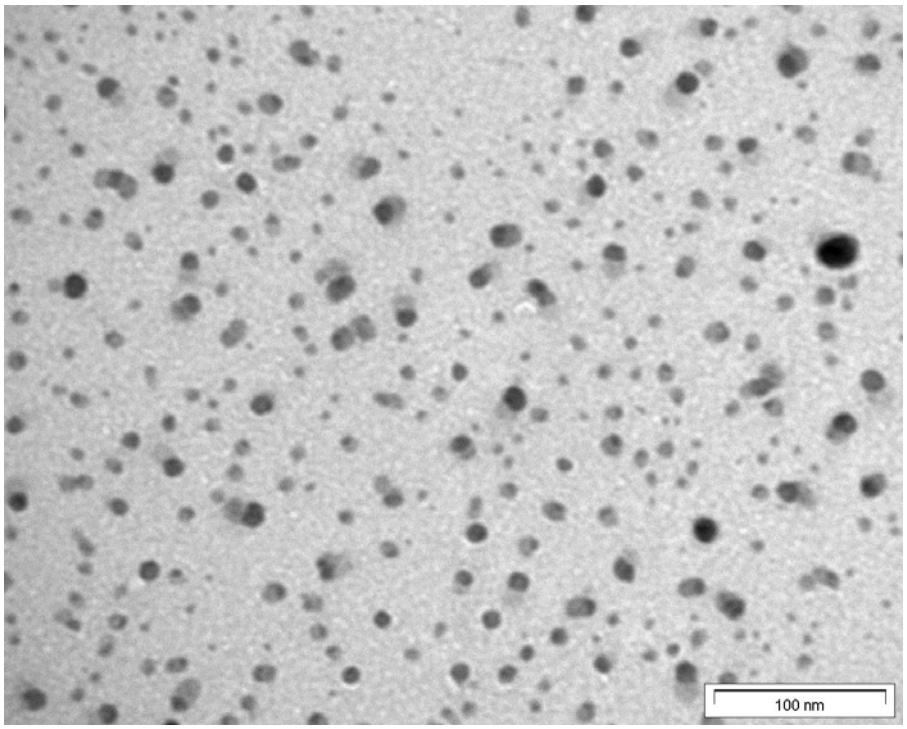

Figure 3.2. TEM image of silver nanoparticle cores (at 200,000x)

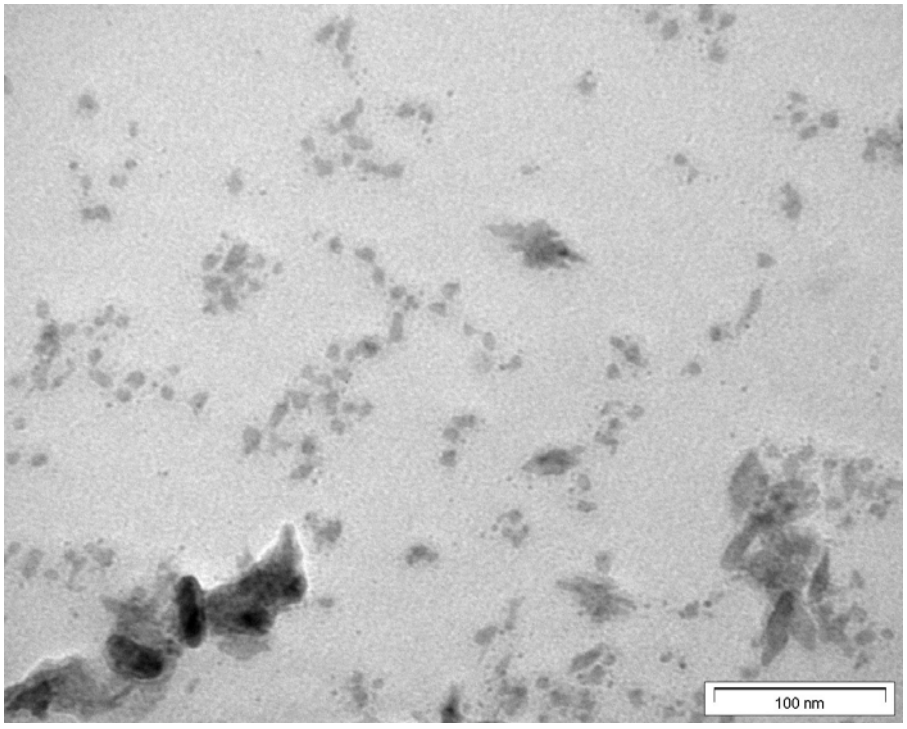

Figure 3.3. TEM image of copper nanoparticle cores (at 200,000x). Apart from small, irregular-shaped particles, also large quantities of larger crystals are present.

From these pictures, it can be seen that the gold and silver particles are approximately sphere-shaped, whereas the copper particles are of irregular shape. Some of the larger crystals can be seen in Figure 3.3. These were not considered in the size measurements. The three pictures were all taken at the same magnification. One can clearly see that contrast is best with gold, with the highest atomic mass. Silver is already lighter and copper shows in grey. The reason is that the electron beam of the TEM can penetrate copper more easily than silver than gold because lighter elements have smaller electron absorptivity.

The particle size was analyzed from these images on a computer by use of a programme called ImageTool®. The particle diameters were measured by drawing a line across by mouse-click. Several errors can occur in this measurement: The resolution of the image (pixel size), the inaccuracy of the manual mouse-click, very small particles are difficult to spot because of the noise in the image at high magnification and therefore they may be under-represented, particles may be counted twice because they cannot be marked as already measured, sometimes two particles are on top of each other, appearing as one larger particle. In spite of all these error sources, measurements proved to be well reproducible with deviations in the average diameter of less than 0.1 nm.

Histograms of the core size distributions were plotted, with the number of categories following the rule of the thumb # categories = (sample size)$^{1/2}$. The frequencies were normalized to a sum of 100%. The sample size was 200.

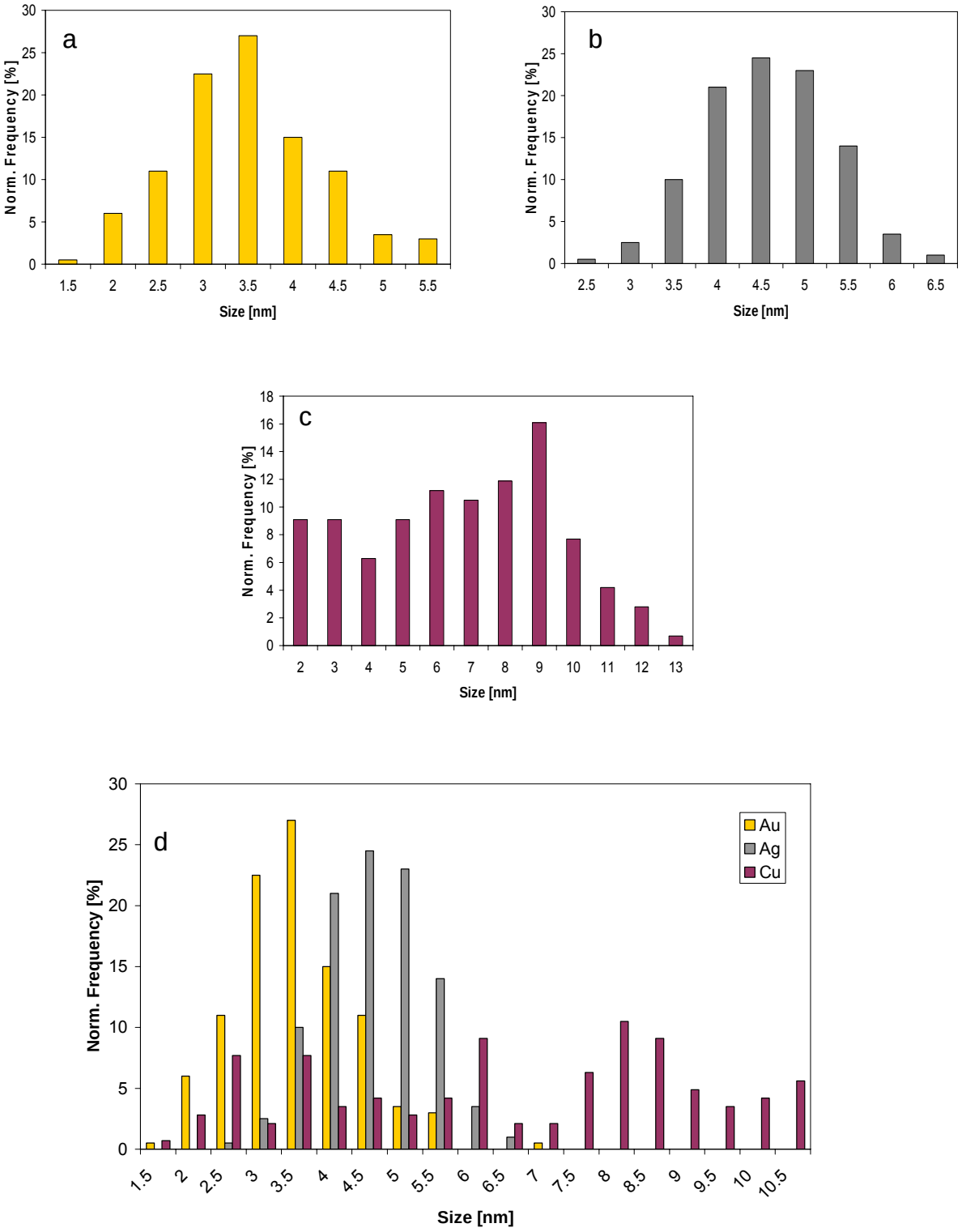

Figure 3.4. Core size distribution histograms. (a) Gold; average size: 3.5±0.8 nm. (b) Silver; average size: 4.6±0.7 nm. (c) Copper; average size: 6.8±3 nm. (d) Gold, silver, and copper.

The core sizes for gold are with 3.5±0.8 nm slightly higher than those described by Brust et al., who found the maximum in the particle size distribution at 2.0-2.5 nm[1]. The size distribution is narrow, as expected for fast addition of the reducing agent. Hostetler et al.[2] explained this with the quick nucleation of cores that grow within a constant thiol-$AuCl_4^-$ ratio. Upon slow reductant addition, on the other hand, very small particles are formed initially, corresponding to a large thiol-$AuCl_4^-$ ratio, whereas later during delivery, depletion of thiol concentration leads to a progression of larger cores.

The silver particles produced with the same molar ratios of reactants, were of significantly larger size. This is not surprising, given that the synthesis takes a different path; it involves a step of precipitation of AgBr as opposed to a phase transfer for the solvated $AuCl_4^-$. Also the oxidation state of the silver (I) source is different from that of gold (III) and the redox potential is different. The measured particle core size corresponds well with literature values[3].

In the core size analysis of the copper nanoparticles, the large crystals were ignored. The distribution was very broad. In Figure 3.4 d, where the nanoparticles of the three metals are shown together in a diagram, one can see that the gold particles were smaller than the silver particles and both distributions had about the same width, whereas the copper size distribution reached from small to very large sizes. The copper distribution in figure 3.4 d looks slightly different from Figure 3.4 c because the data bin width had to be adjusted to be the same as for gold and silver.

The size distributions of gold and silver had near Gaussian shape but if the data bins in the histograms were set narrower, some samples showed bimodal or multimodal distributions which indicated a preference for cluster magic numbers (closed shells)[4].

Self-assembly of nanoclusters to two-dimensional lattices was only observed in very small regions. This was probably due to the dilute samples, the fast evaporation of the solvent (vacuum) and the size distribution being too broad because no size fractionation was done.

3.2 Surface Coverage

The surface coverage, i.e. how many alkakanethiol molecules per surface atom were bonded at a nanoparticle core, was calculated for silver and gold. With the copper nanoparticles, the Brust method produced a small amount nanoparticles among a majority of larger crystals. The calculation described below is based on the elemental composition of the particle sample, thus it would be falsified by the large amount of big crystals.

Hostetler et al. calculated gold core sizes, numbers of surface atoms and theoretical alkanethiolate coverages for magic number clusters[2]. From their table, the number of atoms in a 3.5 nm diameter gold core was interpolated to approximately 1700 atoms. With the molecular mass of gold being 196.97 g/mol, the formula mass of the core was ≈336,000 g/mol. The gold content in the nanoparticles was determined from an ICP-MS measurement. The mass fraction was 0.824, so the molecular mass of the whole particle would be ≈408,000 g/mol. The difference of 72,000 g/mol was the mass of the ligand shell. The molecular mass of the alkanethiolate was 201 g/mol. Therefore the number of ligand molecules per nanoparticle was around 358.

From the same table, the number of surface atoms can be interpolated to 583. The **surface coverage** can be expressed as

number of ligands per surface atom. In this case a value of 61% was obtained. This number is higher than the value reported by Hostetler et al. (between 43% and 46%). To explain the difference, it must be noted that a size of 3.5 nm is between two closed-shell sizes, so there will be more surface atoms on vertex and edge sites, which can bond more ligands to saturate their valence electron shells. Surface defects and non-ideal particle shapes expose further gold surface atoms which can provide binding sites for alkanethiols.

In flat SAMs on gold (111) surfaces, the maximum possible coverage is 33%, i.e. one sulphur group is found in a hollow site between three gold atoms (see also chapter 1.2.2). On the convex surface of nanoparticles, the ligand chains experience less steric hindrance, thus the coverage can be higher.

The calculation of the surface coverage was done in the same way with silver also. Both silver and gold have a face centred cubic crystal structure and very similar lattice constants (Au: 4.0782 Å, Ag: 4.0853 Å), so it seemed appropriate to use the same correlation of radius vs. number of atoms. The average core diameter of 4.6 nm corresponded to approximately 3500 atoms. The molecular mass of silver is 107.87 g/mol, thus the molecular mass of the metal core was ≈377,000 g/mol. The silver content in the nanoparticles, as determined with ICP-MS, was 80.08 %, so the molecular mass of the average nanoparticle was ≈470,000 g/mol. The formula mass of the ligand shell was therefore ≈94,000. With the molecular mass of the ligand being 201 g/mol, the number of ligands per nanoparticle was ≈466. The number of surface atoms for a 4.6 nm cluster is approximately 980. This gives a surface coverage of 48 %. The theoretical value calculated by Hostetler is 42 %, so the value derived here is not far off.

3.3 Place Transfer

Place transfer (ligand exchange) experiments were conducted on silver and gold as described in section 2.4. The ligands transferred onto the particles were ferrocenecarboxyalkanethiols of alkane chain lengths C_8, C_{10} and C_{12}. The extent of exchange was monitored via NMR.

The structure formula of the ferrocenecarboxyalkanethiol ligand is shown below (Figure 3.5).

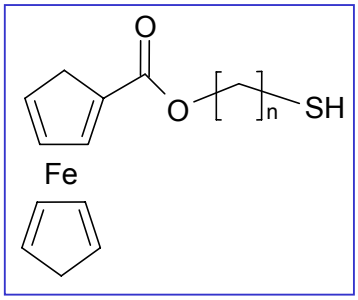

Figure 3.5. The ferrocenecarboxyalkanethiol ligand. n = 8, 10, 12

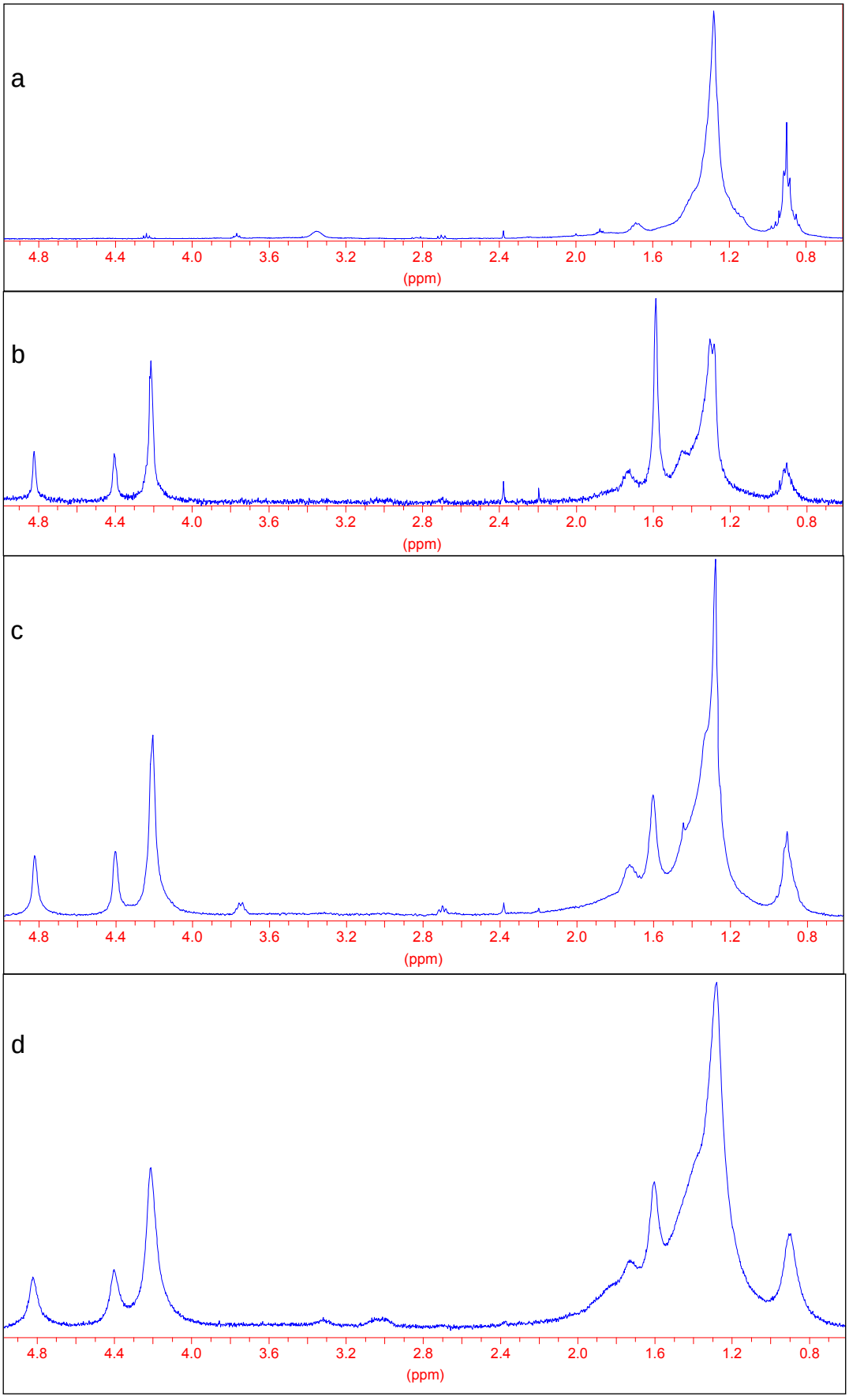
a
4.8
4.4
4.0
3.6
3.2
2.8
2.4
2.0
1.6
1.2
0.8
(ppm)
b
4.8
4.4
4.0
3.6
3.2
2.8
2.4
2.0
1.6
1.2
0.8
(ppm)
c
4.8
4.4
4.0
3.6
3.2
2.8
2.4
2.0
1.6
1.2
0.8
(ppm)
d
4.8
4.4
4.0
3.6
3.2
2.8
2.4
2.0
1.6
1.2
0.8
(ppm)

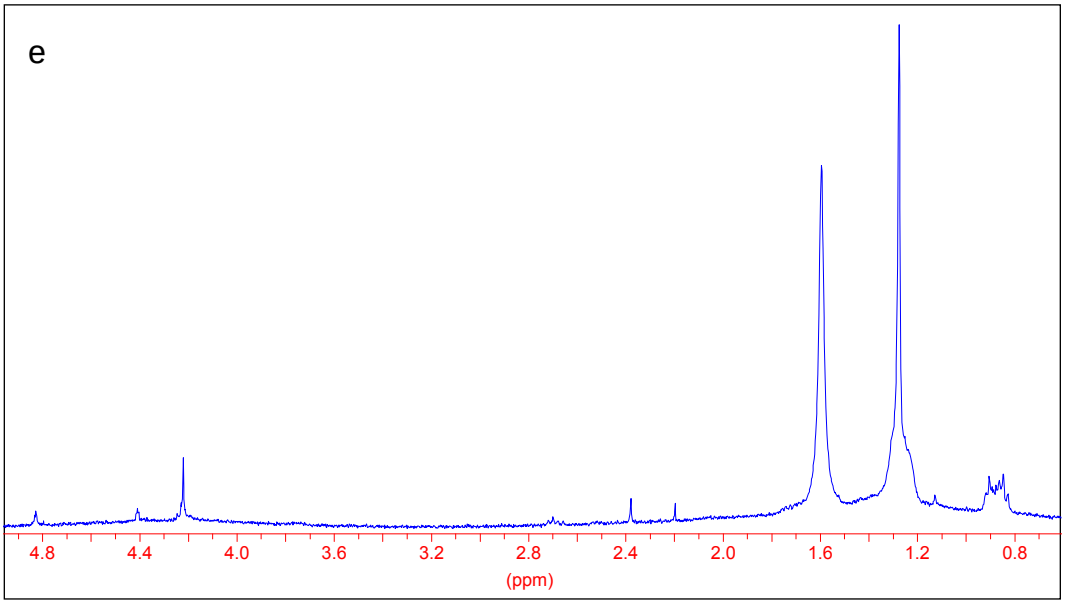

Figure 3.6. ^{1}H-NMR spectra of place-exchanged gold nanoparticles, (a) before place exchange; after exchange with (b) FcC12, (c) FcC10, (d) FcC8; (d) ^{1}H-NMR-spectrum of silver nanoparticles after place-exchange reaction.

In the low field region of the spectra the resonance peaks of the methyl end group shows at 0.9 ppm, the methylene groups of the alkane chains are very similar and show as a broad strong signal at 1.3 ppm, except the CH_2 group next to the sulphur, which experiences the electron withdrawing effect of the sulphur and is left-shifted to 1.6 ppm.

After partial exchange of ligands with ferrocenecarboxy-dodecanethiol (FcC12), -decanethiol (FcC10) or –octanethiol (FcC8), the alkane chain protons of the ferrocene-terminated ligands show also in this region. At 4.2, 4.4, and 4.8 ppm the protons of the ferrocene group give their signal.

An important observation is the line broadening, very well visible in the ferrocene region but also in the alkane chain region, which increases with shorter chainlengths. This effect is due to steric stress

in the ligand shell brought about by the ferrocene functionality which consumes more space than alkane chains. The shorter the chain of the ferrocene-terminated ligand, the deeper the ferrocene is drawn into the ligand layer of dodecanethiol, thus causing steric repulsion between ligands.

In Figure 3.6 e the spectrum of silver nanoparticles, previously subjected to place exchange, is shown. The ferrocene peaks are with 4.2, 4.4 and 4.8 ppm at the same positions as for gold, but they are very small. Apparently, hardly any ligands could be exchanged.

The ratio dodecanethiol : ferrocenecarboxyalkanethiol in the ligand shell was determined for each of these spectra from the integral of the peaks. The integral of the ferrocene protons was defined unity, the amount of methylene protons corresponding to the alkanethiol chain length was subtracted from the integral of methylene peak and the difference represented the contribution from the alkanethiol ligands. This procedure was already described in the literature[5].

The so calculated ligand ratios for gold are shown in table 3.1 as well as the feed ratios.

ligand	feed ratio	product ratio
FcC12	2:1	1:2.3
FcC10	2:1	1:3.0
FcC8	2:1	1:3.3

Table 3.1. Place exchange feed ratios (free ferrocenecarboxyalkanethiol : bonded alkanethiol) and the product ratios (% ferrocenecarboxyalkanethiol in the nanoparticle ligand shell)

The ratios obtained are within the range of values described in the literature for similar ligands[6-8]. The product ratio is much lower than the feed ratio. This means, either the dodecanethiol – gold bond is stronger than the ferrocenecarboxydodecanethiol – gold bond, or the kinetics of the exchange is very slow so that the equilibrium was not reached within 24 hours. The dodecanethiol and the new ligand have both a very similar hydrocarbon chain, so the gold – sulphur bond strength should be nearly the same. What makes a difference is the steric hindrance for the bulky ferrocene groups and this will eventually prevent full exchange, simply because the ferrocene terminated ligands are too large to occupy as many binding sites on the gold surface as dodecanethiol.

The steric hindrance also shows in the decreasing ferrocene ligand ratio in the product with decreasing chainlength. Ferrocene functionalities on short alkane chains get too close to each other and to surrounding dodecanethiol chains, so their exchange onto the gold surface is less favoured than for longer chains where the ferrocene functional group has more space because it is further away from the metal core.

3.4 Surface Plasmon Resonance

As mentioned in chapter 2.14, metal nanoparticles show strong colours which are due to collective oscillation of the free conduction electrons induced by an interacting electromagnetic field.

The UV/VIS spectra of gold, silver, and copper MPCs are shown in figure 3.7 below.

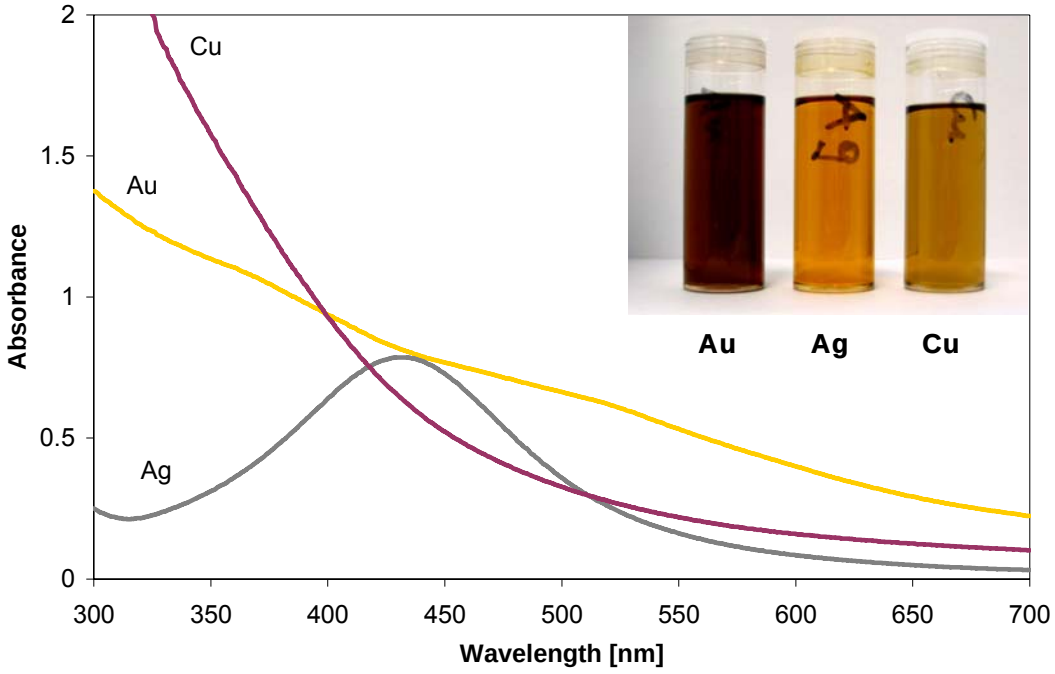

Figure 3.7. UV/VIS absorbance spectra of gold, silver, and copper nanoparticles. Inset: The colours of the nanoparticle solutions.

The silver nanoparticles show a broad absorbance peak with a maximum at 430 nm. This corresponds well with other reports of ligand-protected silver nanoparticles[3, 9, 10]. "Naked" silver nanoparticles are known to show an absorption maximum at 390 nm[11]. This shift of the surface plasmon band by capping of silver nanoparticles can be attributed to the bond formation of the Ag clusters and the ligands.

As shown by Mulvaney[12], the peak position is also dependent on the solvent refractive index and the dielectric constant of the ligand shell and the solvent. Particle size has almost no shifting effect but damping of the resonance occurs with decreasing particle size, so that the absorbance maximum decreases and the band broadens due to surface scattering for small particle sizes, a result of the quantization of the energy levels within the conduction band.

The gold nanoparticles exhibit a strong UV absorption feature which decays exponentially into the visible, with a very weak superimposed broad band at ≈ 510 nm. Like with silver nanoparticles, also for gold nanoparticles the surface plasmon band intensity decreases with decreasing cluster size, as was shown by Hostetler et al[2].

The copper nanoparticles show very strong absorption in the UV region and an exponential-like decay into the visible, without any surface plasmon band. The absence of the surface plasmon band probably stems from the very broad size distribution or the content of small particles < 2 nm[12].

3.4.1 The Effect of the Monolayer Thickness

Instead of dodecanethiol ($C_{12}H_{25}SH$), one silver nanoparticle sample was synthesized with octanethiol ($C_8H_{17}SH$), using exactly the same molarities. In figure 3.8, the UV/VIS spectrum of this sample is compared to the dodecanethiol sample.

The peak position at 430 nm is nearly unchanged but the peak maximum is decreased with the shorter chainlength. Two factors can provoke this effect here: particle size and ligand chainlength. The average particle size of the dodecanethiol sample is 4.6 nm, and 5.6 nm for the octanethiol.

As mentioned above, decreasing particle size leads to damping of the surface plasmon band, thus the peak should be smaller for the dodecanethiol. Exactly the opposite effect is observed. This is due to the difference in ligand chainlength. As shown by Malinsky et al.[13], the

peak height of the silver nanoparticle absorption band increases with monolayer thickness and this effect seems to prevail in this case.

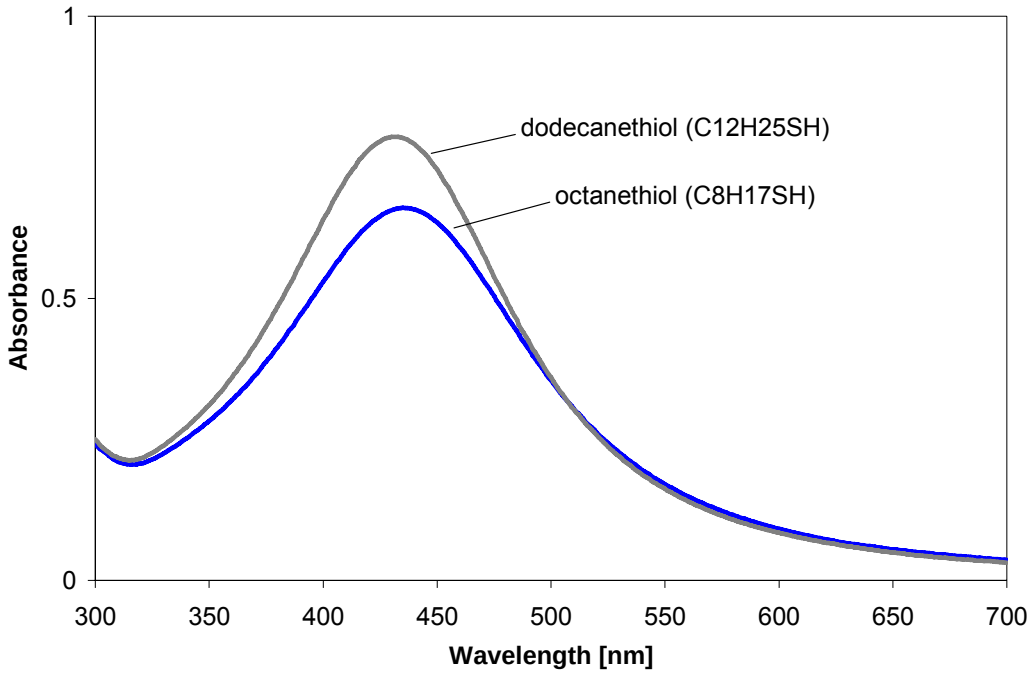

Figure 3.8. UV/VIS spectrum of silver MPCs with dodecanethiolate and octanethiolate monolayers.

3.4.2 Light Sensitivity of Silver Nanoparticles

A silver and a gold nanoparticle sample were left on a window shelf exposed to sunlight for 8 months. During this time, the appearance of the gold nanoparticle solution did not change, whereas the silver sample covered the glass tube with a layer of silver and part of it precipitated. The solution colour changed to brown. The UV/VIS

spectrum shows the complete loss of the characteristic surface plasmon band (figure 3.9). If silver nanoparticles were stored protected from light, they were stable up to one month.

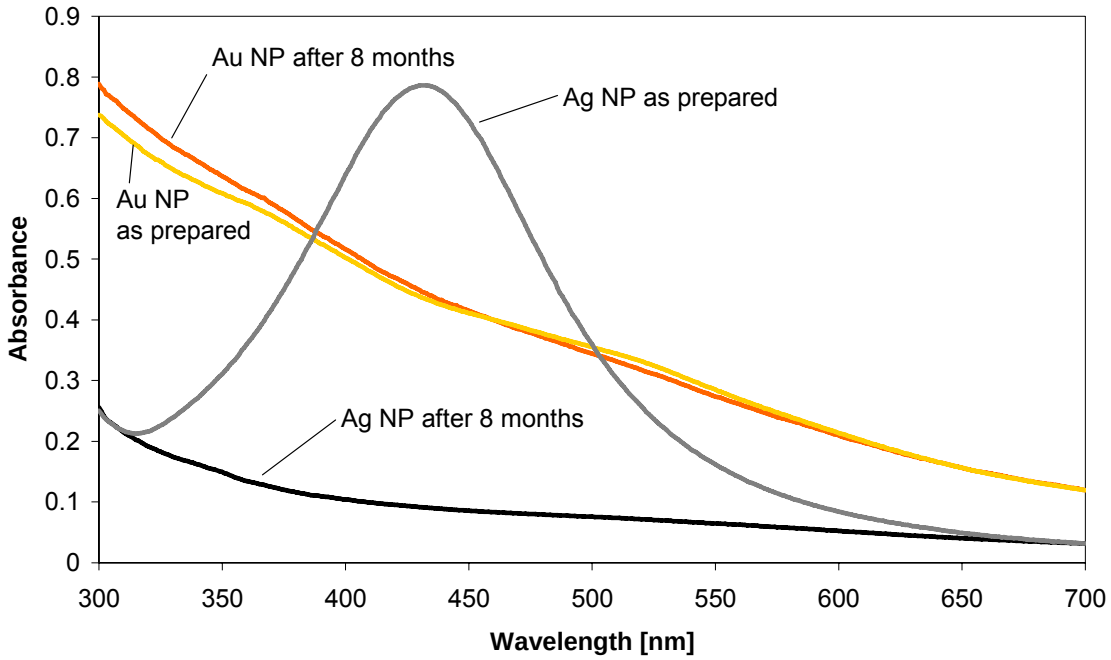

Figure 3.9. UV/VIS absorbance spectra of gold and silver nanoparticles as prepared and after storage in daylight for 8 months. The spectrum of gold was nearly unchanged whereas the silver sample lost the absorbance peak completely.

3.5 Nanoparticle Capacitance

Monolayer-protected metal nanoclusters can be regarded as "nanocapacitors" in that they consist of a metal core, a dielectric layer of ligand molecules and an outer plane of ions in the surrounding solvent. Thus, an MPC can be regarded as a concentric sphere capacitor, as illustrated in Figure 3.10.

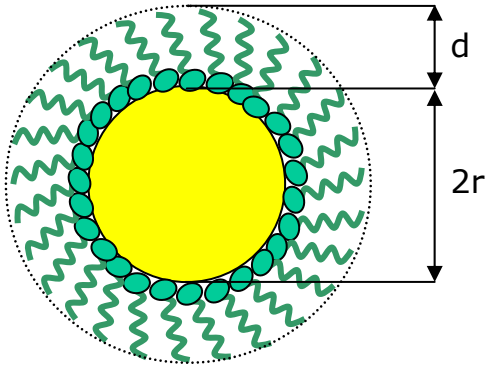

Figure 3.10. MPC as a concentric sphere capacitor.

Charging and discharging of this cluster involves the transfer of single electrons onto/from the core. Electrons tunnelling through the dielectric of the ligand shell change the potential of the metal core and due to the finite size of the cluster, the potential will jump each time a tunnelling event takes place. The result of this is a staircase current-potential characteristic. This is also called *Coulomb staircase* and the potential step is called *Coulomb blockade* (see Figure 3.11).

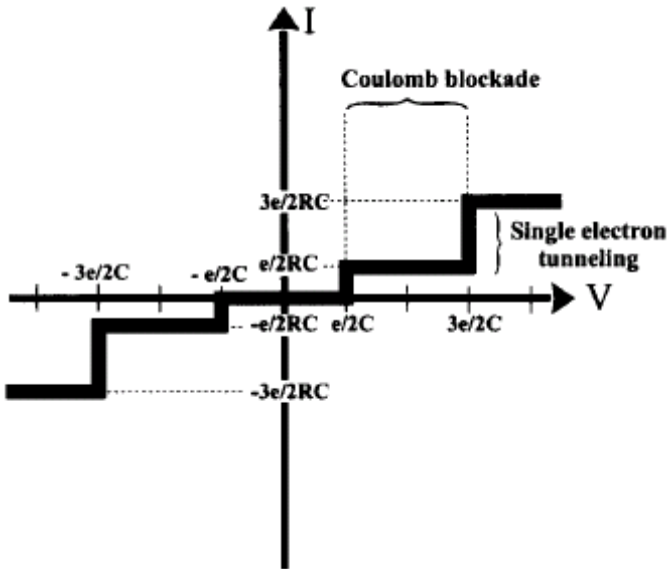

Figure 3.11. Ideal staircase I-V characteristics of a single-electron tunnelling junction (Reproduced from reference 14).

The MPC acts as a single-electron tunnelling junction. As the junction is biased by a constant current I and the potential at the junction is greater than e/2C (e is the electron charge, C is the capacitance of the junction), a tunnelling event takes place, making the core potential jump to –e/2C and a new charging cycle restarts. The junction is Coulomb blockaded as long as the potential V < e/2C, while single electron tunnelling is characterized by a jump of the current at V > e/2C. Each single-electron tunnelling generates a jump of e/RC in the current, because the current is proportional to the reciprocal of the resistance R of the junction times the potential V.

For the observation of single-electron events, two requirements must be fulfilled:

First, the electrostatic energy of introducing an electron into an isolated nanoparticle core, E_C, has to be larger than its thermal

fluctuation, k_BT (k_B is the Boltzmann constant, T is the absolute temperature):

$$E_C = \frac{e^2}{2C} >> k_B T \qquad (3.1)$$

This can be achieved by decreasing the temperature or the capacitance. Capacitance is dependent on the MPC size. Typically, for single electron charging to be observed at room temperature, the MPC capacitance must be in the sub-attofarad region, which is fulfilled for MPCs of sizes well below 10 nm.

The second requirement is that the dielectric barrier which surrounds the conducting nanoparticle should have a tunnelling resistance, R_T, which exceeds the resistance quantum h/e^2 ($R_T >> h/e^2 \approx 25.8$ kΩ). This requirement is met by the insulating SAM layer on the MPCs, which ensures the localization of the electron in (or on) the nanoparticle.

3.5.1 The Concentric Sphere Capacitor Model

The simplest model which gives an estimate of the MPC capacitance is the concentric sphere capacitor model. For a capacitor formed from concentric conducting spheres separated by a dielectric (the alkanethiolate monolayer) of thickness d and dielectric constant ε, the capacitance is given by

$$C_{CLU} = 4\pi\varepsilon_0\varepsilon\frac{r}{d}(r+d) \qquad (3.2)$$

C_{CLU} is the cluster capacitance, ε_0 the vacuum permittivity, r the radius of the core (measured by TEM), and d the monolayer thickness, approximated by the monolayer chain length (See also figure 3.10). Equation (3.2) shows that the cluster capacitance increases with core radius and decreases with monolayer thickness.

This very simplified model involves several approximations:

1) The core shape is not fully spherical but, as mentioned before, polyhedral structures like icosahedra and truncated octahedra dominate.

2) The lengths of fully extended alkanethiolate chains are assumed to define the dielectric thickness. The tilt of SAM molecules on metal surfaces is ignored.

3) The outer sphere of the phase boundary between the ligand chains and the solvent is not spherical, for one reason because the underlying metal core itself is not spherical and then the tilt of the SAM is not uniform because the core surface consists of (111) and (100) faces which provoke different tilt angles.

4) The phase boundary between monolayer dielectric and the surrounding electrolyte is assumed to be sharp and the electrolyte is assumed to be a good conductor over the entire sphere, which means that the ionic charge is homogeneously distributed. Helmholtz and diffusion layers are ignored. In reality, chain density decreases with the distance from the core, so that intercalation of solvent and ions in the monolayer is possible at the ligand chain ends.

5) Defects of the core surface and the monolayer are ignored.

6) The cluster capacitance is thought to be independent from the core charge, or the potential between the inner and the outer capacitor spheres. This is only true for a hard capacitor. Indeed, there are measurements indicating that the monolayer behaves as a soft sphere.

3.5.2 Quantized Charging

Based on a theory by Weaver et al.[15], Chen, Murray and Feldberg[16] developed a theoretical approach to formulating the potentials at which successive single electron transfers arising from quantized charging of metal nanoparticles occur. This theory involves the simplifications that

(a) the MPC capacitance is based on a spherical metal core,
(b) effects of HOMO – LUMO band gaps are neglected, and
(c) the MPC capacitance is assumed to be independent of the cluster's state of charge.

MPCs can be formally regarded as a multivalent redox system which exhibits equally spaced formal redox potentials. Thus, a mixture of nanoparticles having charge z and z-1 in a solution formally comprises a mixed valent solution of a "redox couple" with a formal potential $E^0_{z,z-1}$, which is dependent on the charge state z:

$$E^{0}_{z,z-1} = E_{PZC} + \frac{(z-\frac{1}{2})e}{C_{CLU}} \qquad (3.3)$$

E_{PZC} is the potential at zero charge, where the charge state of the metal core equals 0.

This equation is only valid for *equally spaced* potentials like illustrated in figure 3.11. In this case, where C_{CLU} is independent of z, the formal potentials of the charging steps should vary linearly with the valence states of the nanoparticle. From a plot $E_{z,z-1}$ versus z, the average nanoparticle capacitance can be evaluated.

A very important observation, made by Ingram et al. in 1997[17], is that this quantized charging can not only be observed for single clusters, but that also an ensemble of the same clusters. This means that a nanoparticle solution at an electrode demonstrates the same staircase charging behaviour as a single particle at an STM tip.

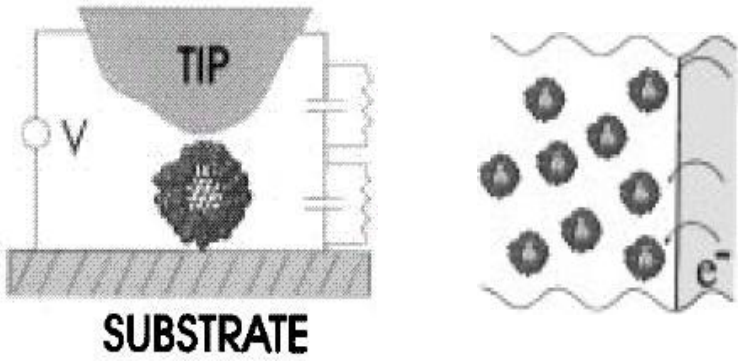

Figure 3.12. A single nanocluster at an STM tip and a nanoparticle solution at an inert electrode – both show the same staircase charging behaviour (Reproduced from reference 17).

Equation (3.3) has one severe disadvantage: The E_{PZC}, the potential of zero charge, is medium-dependent and very difficult to

determine experimentally. Very recently, Su and Girault[18] developed a way to determine the absolute standard redox potential, $[E^0_{z,z-1}]_{abs}$, on the basis of Born's model of ionic solvation, as illustrated in figure 3.13 below.

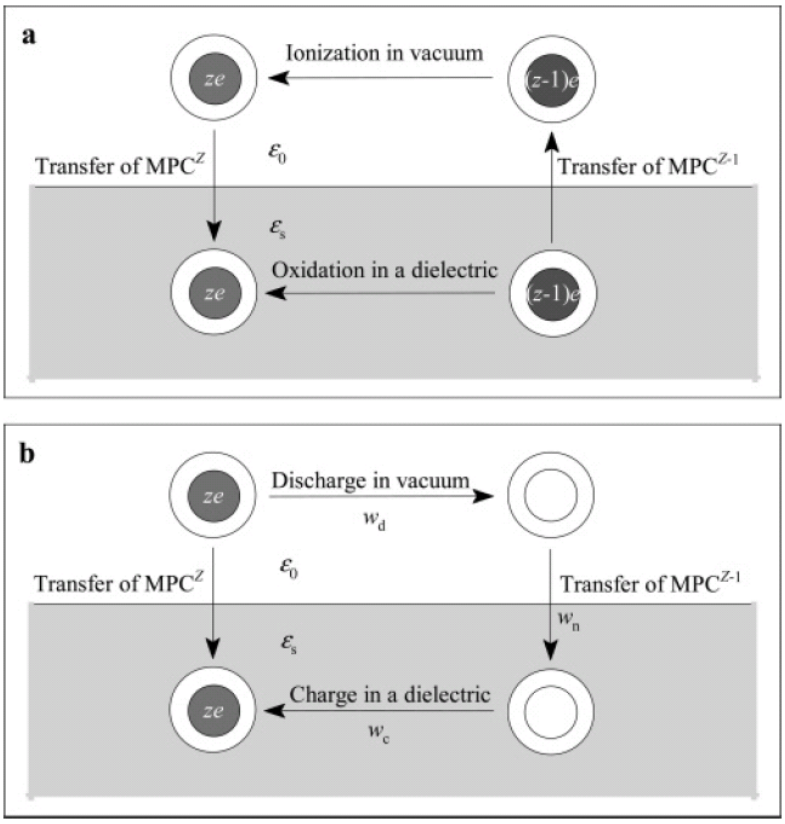

Figure 3.13. (**a**) A single-electron oxidation process in a solvent phase can be seen equivalent to a cycle of an ionization process in the vacuum preceded and followed by transfer of a charged-state couple of MPC between the vacuum and the solvent phase; (**b**) Born's model applied on the solvation of an MPC^z (Reproduced from reference 18).

As shown in Figure 3.13 a, the single-electron oxidation reaction in the solvent phase can be represented in three steps of a Born cycle:

The transfer of MPC^{z-1} from the solvent phase to the gas phase, the ionization of MPC^{z-1} to form MPC^{z} in the gas phase, and the transfer of MPC^{z} from the gas phase to the solvent phase. Figure 3.13b shows that the work of transferring MPC^{z} from the gas phase to the solvent phase can be expressed by the sum of the work of discharging MPC^{z} in a vacuum (to form a neutral sphere of the same size), the work of transferring this neutral sphere from the vacuum to the solvent phase, and the work of charging this sphere in the solvent phase.

Without the need of knowledge of a potential of zero charge (E_{PZC}), The absolute redox potential can be deduced from the charge state, z, the work function of the metal, Φ, the dielectric constant of the solvent, ε_s, the dielectric constant of the monolayer, ε_d, the core radius, r, and the monolayer thickness, d:

$$\left[E^{0}_{z,z-1}\right]_{abs} = \frac{\Phi}{e} + \frac{\left(z-\frac{1}{2}\right)e}{4\pi\varepsilon_0\left(r_0+d\right)}\left(\frac{d}{\varepsilon_d r_0}+\frac{1}{\varepsilon_s}\right) \qquad (3.4)$$

The E_{PZC} of a bulk metal is linked to the work function of the metal:

$$E_{PZC} = \frac{\Phi}{e} + \Delta^{M}_{S} g(dip) + \chi^{S} - \chi^{M} \qquad (3.5)$$

$\Delta_S^M g(dip)$ is the dipolar contribution to the metal/solution potential difference, and χ^S and χ^M represent the surface potential of the electrolyte and the surface potential of the bare metal, respectively.

Determination of the Cluster Capacitance by Cyclic Voltammetry

As described in section 2.9, cyclic voltammetry was conducted with gold, silver and copper nanoparticles.

The recorded electrochemical spectra are shown below, together with the first order derivative, for easier peak recognition. Differential pulse voltammograms yielded the same spectra as the derivatives; therefore they are not presented here.

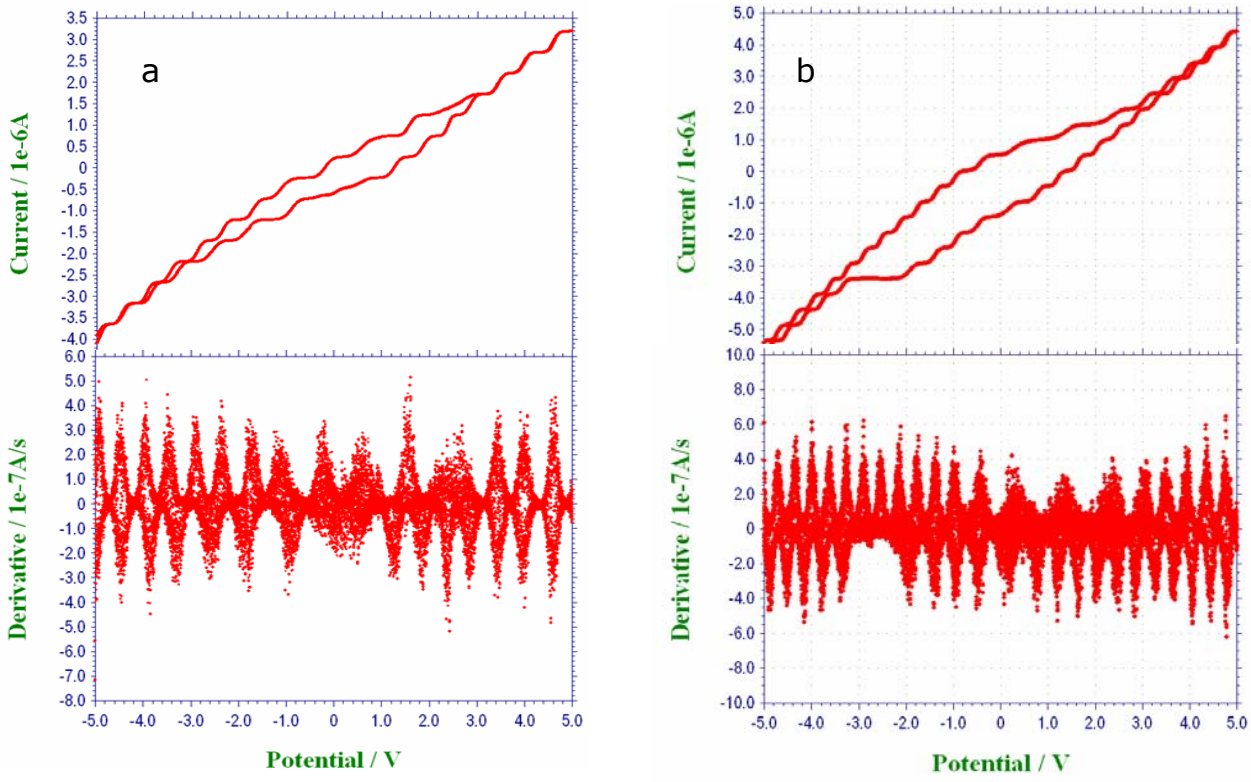

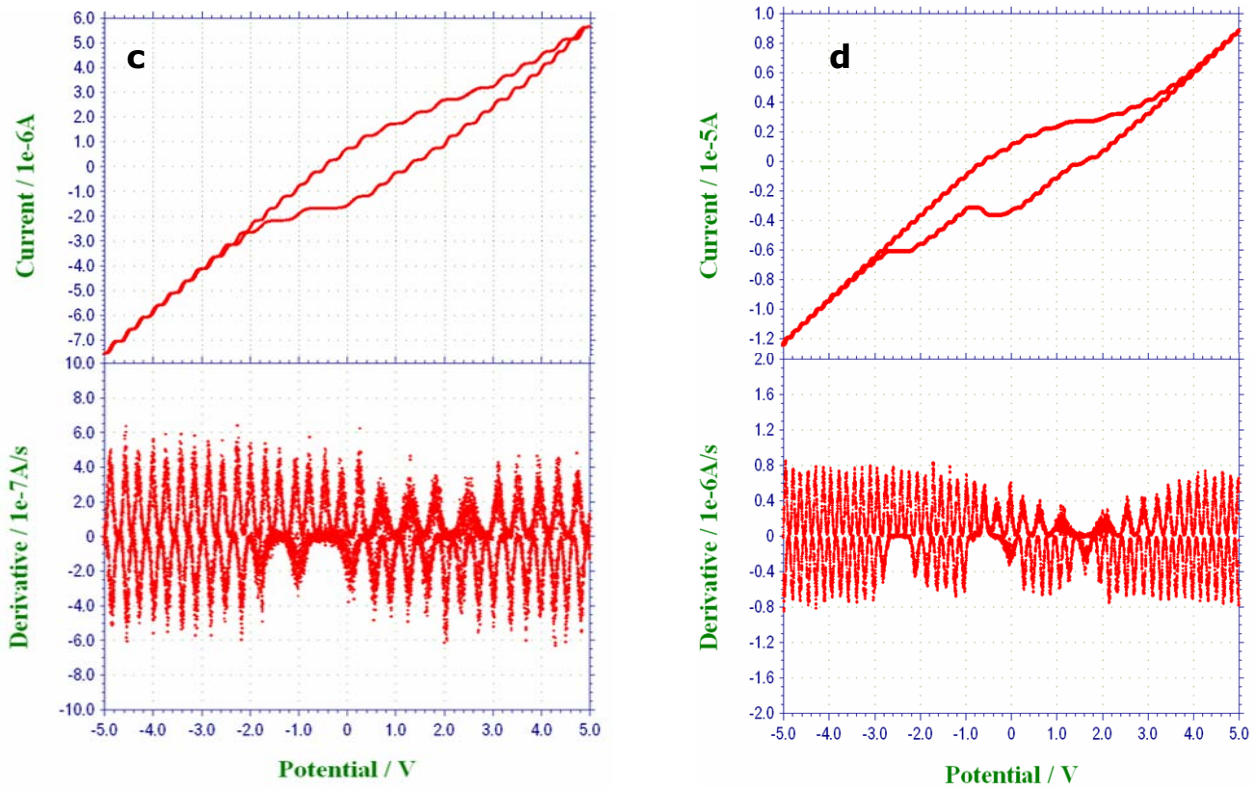

Figure 3.14. Cyclic voltammograms of alkanethiol protected (a) gold, (b) copper, (c) silver, and (d) octanethiol protected silver MPCs and their first order derivatives, respectively. All recorded with 100 mV/s. Potentials vs. aqueous Ag/AgCl reference electrode.

The four voltammograms all show staircase charging features, as well as a larger step, which can be attributed to the HOMO-LUMO gap, indicating that the nanoparticles can be regarded as large molecules with many energy states, rather than bulk metal particles (The HOMO-LUMO gap stems from the smallest particles in the polydisperse samples[19]).

As it can be seen from equation (3.3), the charging steps will increase in width with decreasing cluster capacitance. If graphs a, b, and c in figure 3.14 are compared, where in all three cases the same ligand was used, the thickness of the dielectric, d, must be the same

and any difference in the capacitance must originate from differences in the core radius. In fact, if gold (a) and silver (b) are compared, one clearly sees that the steps are narrower with silver, therefore the cluster capacitance must be greater and also the core radius. As it was shown in section 3.1, the silver nanoparticles, indeed, have a larger core.

With copper, the situation is made a bit more complicated by the broad size distribution. If the peak spacing in copper is compared to silver and gold, one would expect a core size between those of silver and gold. TEM measurements, however, showed the largest average particle diameter for copper. The copper size distribution has a large population at small sizes of 2-3 nm as well as a large population at around 9 nm. As mentioned before, there is a size limit below which quantized charging effects can be observed at ambient temperature. The large particles have great influence on the average of the size but they do not influence the single electron transfer steps. Their charging steps are too small to be detected and therefore the spectrum is dominated by the population of smaller particles.

In the derivatives of the cyclic voltammograms the staircase waves show as peaks. In the spectra of gold and copper, especially in the middle of the potential range, some peaks show side-peaks with different spacing, which shows that there are two (or more) particle populations of different sizes present.

The peak positions were measured from the derivatives, where they could be localized more easily. The charge state 0 was assigned to the valley nearest to the open circuit potential of the electrochemical cell. According to equation (3.3), the peak position potentials $E_{z,z-1}$ were plotted versus the charge states z-1/2.

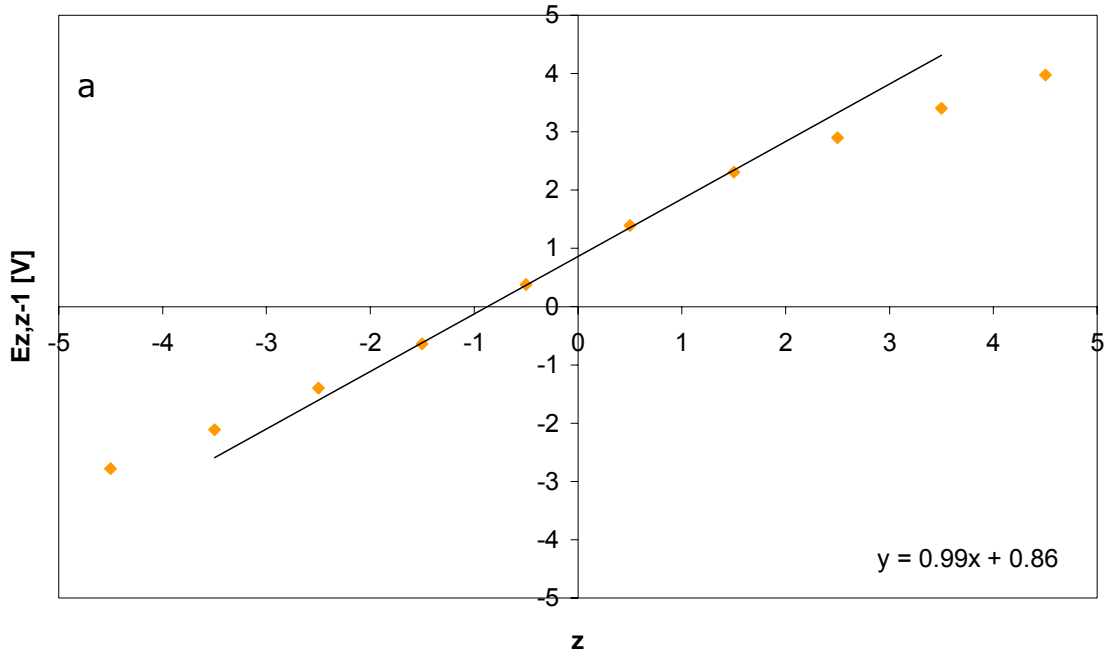
a
Ez,z-1 [V]
z
y = 0.99x + 0.86

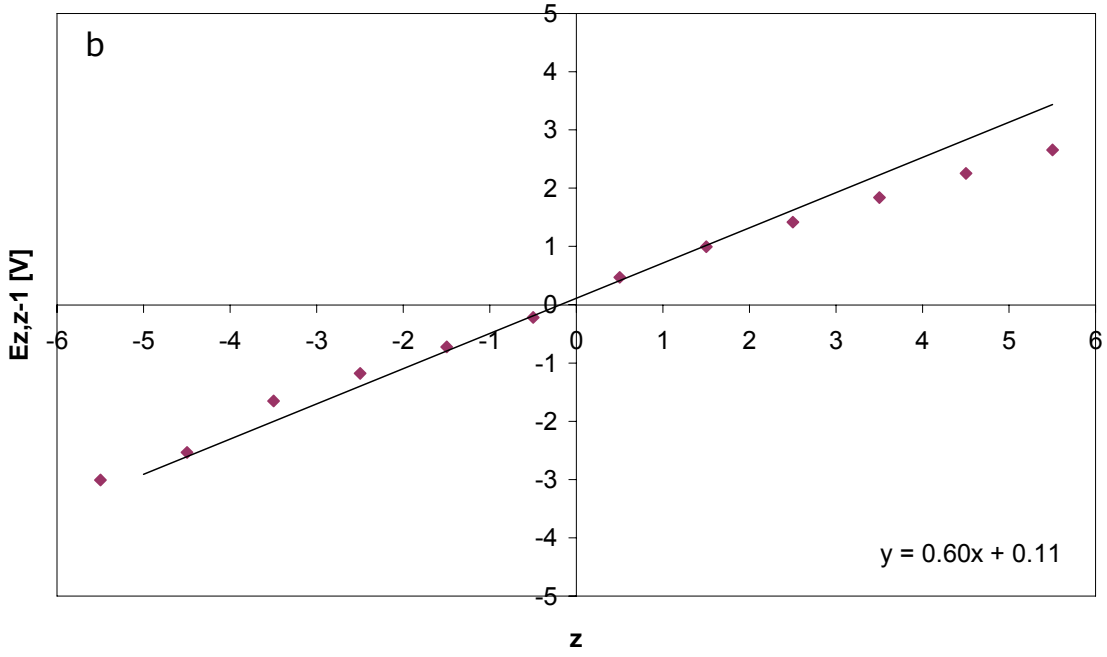
b
Ez,z-1 [V]
z
y = 0.60x + 0.11

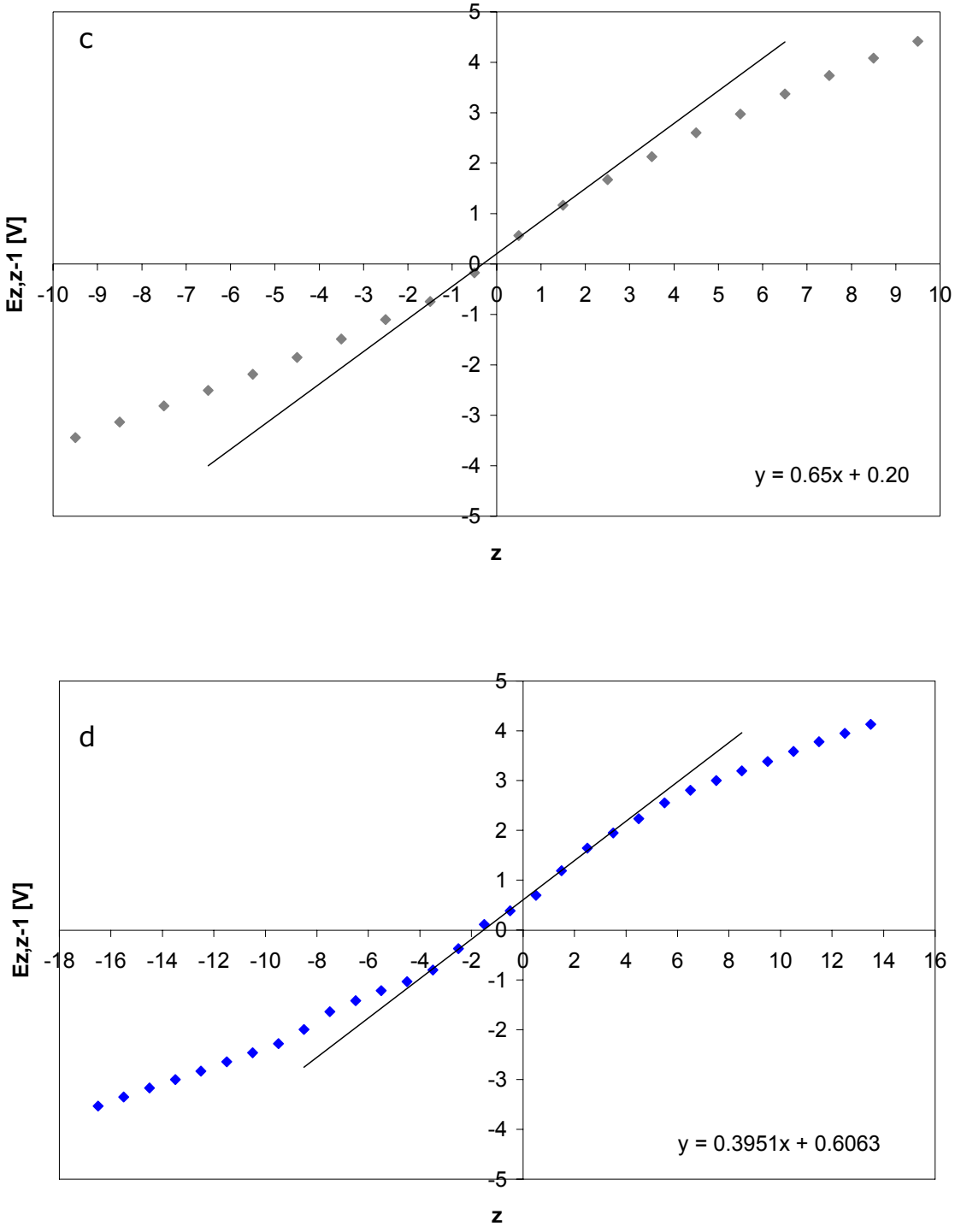

Figure 3.15. Z-plots of peak potential, $E_{z,z-1}$, versus charge state, z, of alkanethiol protected (a) gold, (b) copper, (c) silver, and (d) octanethiol protected silver MPCs. Potentials vs. aqueous Ag/AgCl reference electrode.

From figure 3.15 it is obvious that the linear correlation of potential vs. charge state – as proposed in equation (3.3) - is not fully appropriate. A linear slope is only observed in the centre region between $E_{-1,-2}$ and $E_{2,1}$. For charge states beyond this range, the cluster capacitance cannot be regarded as independent of the core charge any more[19]. The graphs in figure 3.15 also show that it was valid to assign the zero charge state to the open circuit potential (OCP). The middle of the linear region in the centre (where Chen's equation applies) is located at the assumed zero charge state.

Straight lines were fitted through the four charge states in the centre. The intercept gives the E_{PZC} and from the slope the cluster capacitance was calculated (equation 3.3). The results are tabulated below as well as the capacitances derived from the concentric sphere capacitor model.

Sample	**C_{CSC} [aF]**	**C_{CV} [aF]**	**C_{CSC}/ C_{CV}**	**E_{PZC} [V]**	**OCP [V]**
Au C12	0.75	0.19	4.0	+0.99	+0.80
Cu C12	2.06	0.27	7.8	+0.11	+0.11
Ag C12	1.13	0.31	3.6	+0.20	+0.19
Ag C8	1.88	0.41	4.6	+0.61	+0.40

Table 3.2. Cluster capacitances calculated from the concentric sphere capacitor model (C_{CSC}) and from the cyclic voltammetry plots (C_{CV}), the potential of zero charge (E_{PZC}) and the open circuit potential (OCP). C12 stands for dodecanethiol as ligand, C8 stands for octanethiol. The parameters for the concentric sphere capacitor calculations were d = 2.3 nm and 1.6 nm for dodecanethiol and octanethiol, respectively (derived from bond lengths), ε = 2.2, r was taken from the average core size determined from TEM.

The cluster capacitances derived from the concentric sphere capacitor model are all about four-fold above those derived from the z-plots of the cyclic voltammograms, except for copper, where the difference is even greater. In the spherical capacitor model, large particles, which do not show staircase charging and therefore have no or little influence on the quantized capacitance, C_{CV}, contribute to the spherical capacitance, C_{CSC}, via the average of the core size.

C_{CSC} can be used to estimate the order of magnitude of the cluster capacitance but for measurements that are more precise the determination from the staircase spacing in the CV is necessary.

The trend that increasing core radius and decreasing monolayer thickness result in an increase of cluster capacitance, as predicted by the concentric sphere capacitor model, is confirmed by the cyclic voltammetry results.

The elemental composition of the core, whether it is composed of gold, silver, or copper, does not affect the capacitance, as it is the same with macroscopic capacitors, where the capacitor sphere material does not affect the capacitance, as long as it is a metallic conductor.

The nature of the core material, however, has influence on the potential of zero charge, due to the different work functions of gold, silver, and copper. This is illustrated well by equation (3.5) above.

The potentials of zero charge, E_{PZC}, as derived from the intercepts of the z-plots, correspond well to the measured open circuit potentials, OCP. This means, as long as no current is applied on the particle solutions, the particles are on average in a neutral charge state.

3.6 Diffusion Coefficient

3.6.1 Calculation from the Stokes-Einstein Equation

The Diffusion Coefficient *D* was calculated using the Stokes-Einstein Equation (3.6) where η is the solvent viscosity and r_H the hydrodynamic radius of the species. (r_H= r + d).

$$D = \frac{k_B T}{6\pi\eta r_H} \qquad (3.6)$$

This model includes several simplifications:

1) The particles are thought to be spherical.

2) The hydrodynamic radius is approximated by the particle radius (the ligand shell included). Adsorbed ions or solvent and solvation shells are ignored.

3) The viscosity is approximated by the solvent viscosity which for the toluene/DCM mixture was interpolated from the viscosities of the pure solvents. Any influence of the dissolved nanoparticles on viscosity is ignored.

The values obtained for gold, copper and the two silver samples are tabulated in table 3.3 below.

Sample	r_H [nm]	D [$m^2 s^{-1}$]
Au C12	4.1	1.02×10^{-10}
Cu C12	5.7	0.72×10^{-10}
Ag C12	4.6	0.90×10^{-10}
Ag C8	4.4	0.94×10^{-10}

Table 3.3. Diffusion coefficients derived from equation (3.6).

The diffusion coefficient decreases with increasing hydrodynamic radius. The octanethiol protected silver particles (Ag C8) have a larger core than the dodecanethiol protected silver particles (Ag C12), but the ligand shell is thinner with octanethiol, therefore the hydrodynamic radius is lower for the octanethiol coated particles.

3.6.2 Determination by Rotating Disc Electrode

The procedure and background of the rotating disc electrode experiment is described in section 2.10. The diffusion coefficient was determined from the limiting current of the redox active ligand ferrocenecarboxydodecanthiol. For this measurement it is necessary that the nanoparticles, functionalized with the redox active ligand via place exchange, show the ferrocene redox peaks (figure 3.16).

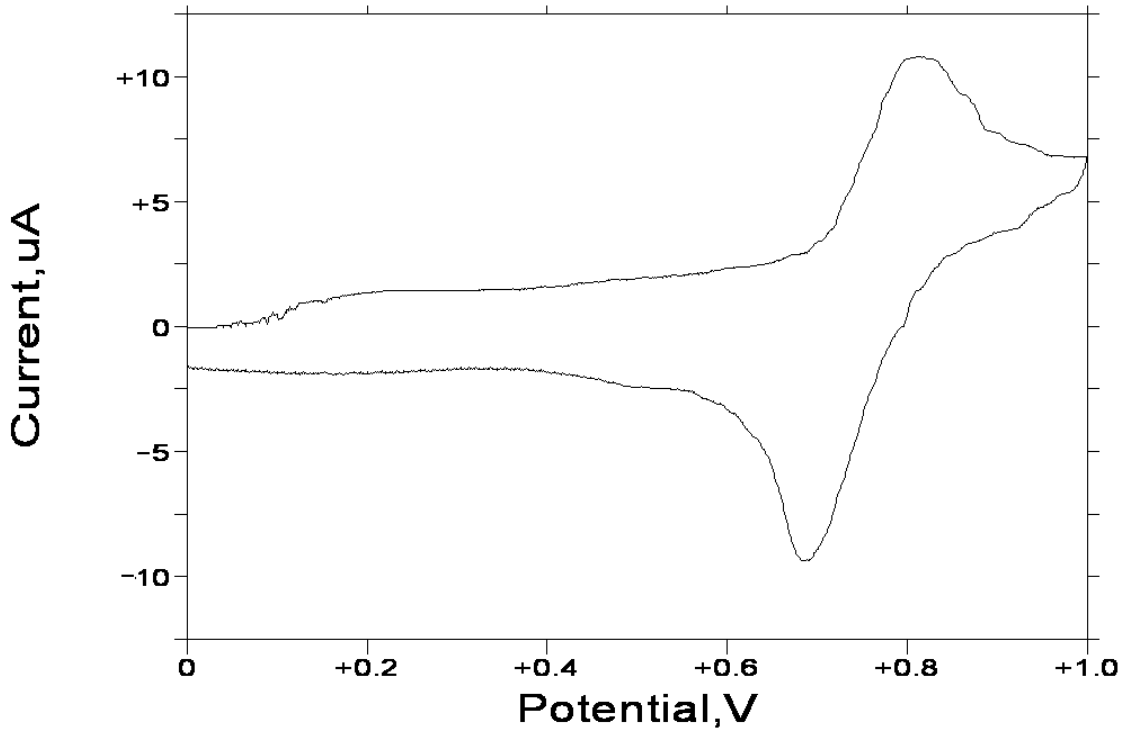

Figure 3.16. Cyclic voltammogram of ferrocenecarboxydodecanethiol protected gold nanoclusters (Au FcC12). Scan rate 0.2 V/s. Potential vs. aqueous Ag/AgCl electrode.

Of the nanoparticles subjected to ligand place transfer, only gold FcC12 was used for RDE. FcC10 spontaneously decomposed when the solvent from NMR was evaporated, covering the glass with a layer of gold. FcC8 did not show the ferrocene peaks in the CV. Obviously, the exchange ratio had not been sufficient. With Silver FcC12, the exchange reaction did not work (see also section 3.3); the copper nanoparticles precipitated out of solution.

The cyclic voltammogram (figure 3.16) shows a redox wave at 0.8 V in anodic (positive) sweep direction which corresponds to the oxidation of ferrocene to ferrocenium and in cathodic (negative) sweep direction, the reduction of ferrocenium to ferrocene results in a peak at 0.7 V. This reaction is outlined below for a single ligand molecule (R is

the carboxyalkanethiol rest). The reaction scheme does not change whether the ligand is free in solution or bonded to a metal nanoparticle.

$$R\text{-}Fc \rightleftharpoons [R\text{-}Fc]^{+} + e^{-} \qquad (3.7)$$

With the FcC12 gold nanoparticle sample CV measurements were conducted at various rotation speeds. The voltammograms are shown in figure 3.17.

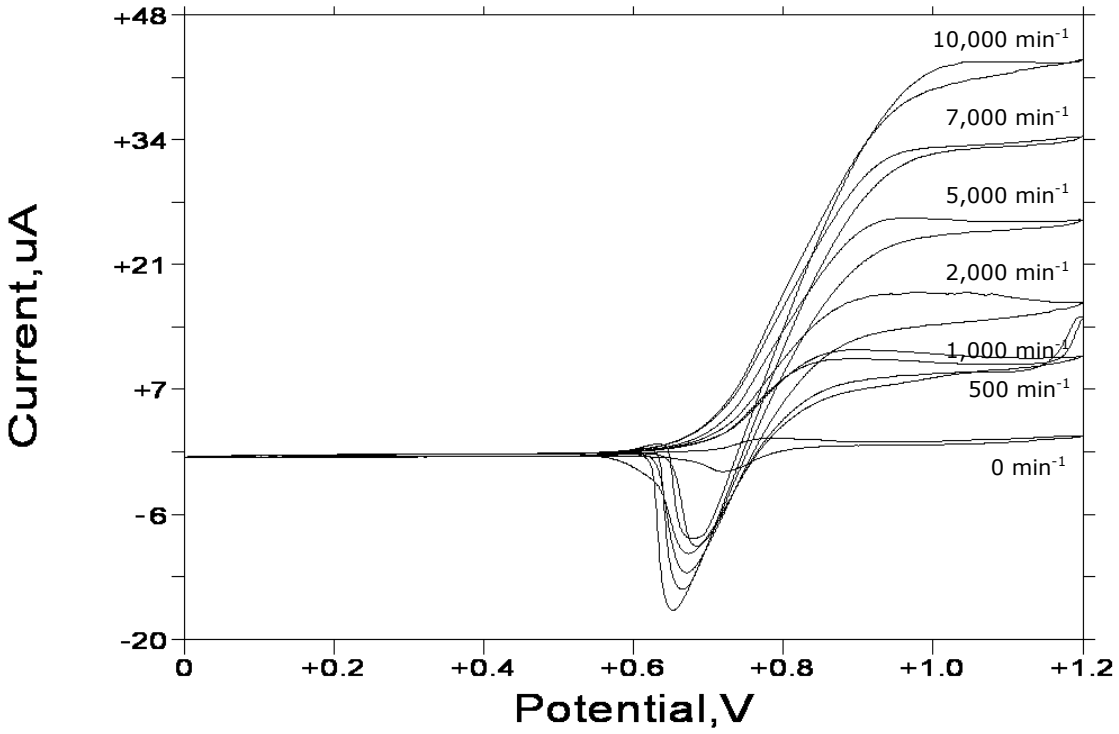

Figure 3.17. Limiting current plateaus of cyclic voltammograms at a rotating disc electrode at different rotation speeds. Scan rate 5 mV/s. Potentials vs. aqueous Ag/AgCl.

The CVs with rotation show a sigmoidal curve with a limiting current plateau at very positive potential, as well as a reduction peak at

around +0.65 V in negative scan direction. Both increase with rotation speed.

As described in section 2.10, the step height, the so-called Levich or limiting current i_L, was plotted versus the square root of the angular frequency, $w^{1/2}$. This was done in figure 3.18.

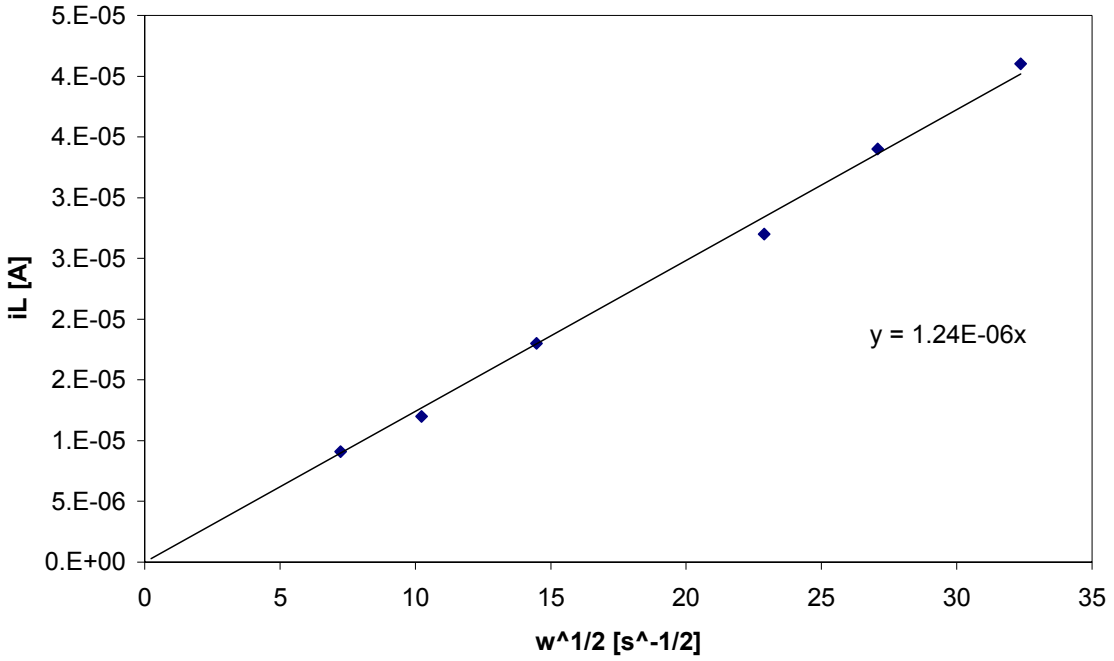

Figure 3.18. Levich plot for determination of the diffusion coefficient from the rotating disc electrode experiment series of figure 3.17.

According to the *Levich equation* (3.8), the Levich current is dependent on the rotation speed and the concentration.

$$i_L = 0.62nFAD^{\frac{2}{3}}\upsilon^{-\frac{1}{6}}c^{\infty}\omega^{\frac{1}{2}} \qquad (3.8)$$

The concentration, c^{∞}, is the bulk concentration of the electroactive species, which is the concentration of ferrocene ligands, not of

nanoparticles. From the molecular mass derived in section 3.1 and the known yield (44 %) in the place transfer, the molecular weight of the particles after place transfer was found to be 444,000 g/mol. For the experiment 18.2 mg nanoparticle powder were dissolved in 15 mL of DCM. From this, a nanoparticle concentration of 2.7 µM was derived. A particle had 358 ligands, of which 44% (that is 158) were ferrocene functionalized ligands. Finally, this gave a concentration of ferrocene functional groups of 43 mM.

From the Levich equation (3.8), the diffusion coefficient of the nanoparticles, D, could be calculated. The kinematic viscosity of DCM is 0.32 x 10^{-6} m^2 s^{-1}. The electrode area was 3 mm^2.

From these data, the diffusion coefficient of ferrocenecarboxydodecanethiol and dodecanethiol protected gold nanoparticles equals 1.5 x 10^{-9} m^2s^{-1}.

3.6.3 Determination by Chronoamperometry

Potential steps were applied on the nanoparticle electrolytes as described in section 2.12. For this purpose the potential had to be stepped to potentials corresponding to defined nanoparticle charge states. This posed a major problem because the whole staircase spectra in the CVs were subject to strong shifts in potential, depending on what potential had been applied to the electrolytes before. The open circuit potentials as well, were shifted by up to 1 V after polarization through cyclic voltammetry measurements and it took them several hours to gain their equilibrium again. This problem occurred with all nanoparticle electrolytes, gold, silver, and copper.

In spite of that, chronoamperometric measurements were conducted at 50 different potentials in a range of -10 to 10 V for dodecanethiol protected gold nanoparticles. As an example, in figure 3.19, the current response to a potential step from +0.82 V (the equilibrium OCP) to -2 V after a time t = 0.5 s, is shown.

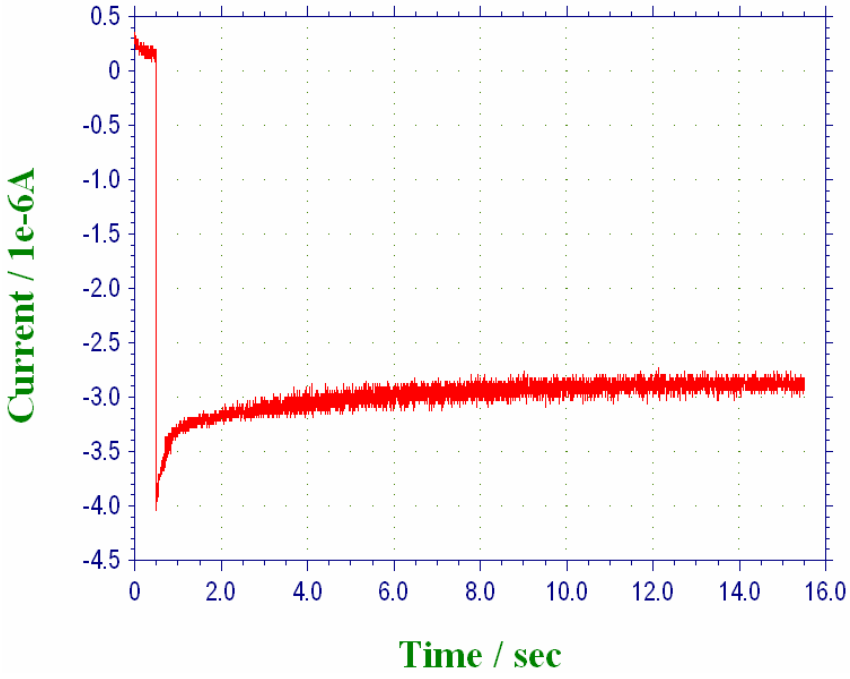

Figure 3.19. Chronoamperometric current response of a gold nanoparticle electrolyte to a potential step from +0.81 V to -2 V. The step was applied after t = 0.5 s.

According to the *Cottrell* equation (3.9), the current should approach an equilibrium value asymptotically with time (i as a function of $1/t^{1/2}$):

$$|i| = \frac{nFD_i^{\frac{1}{2}}c_i^{\infty}}{\pi^{\frac{1}{2}}t^{\frac{1}{2}}} \qquad (3.9)$$

|i| is the absolute current density, n is the charge state, and c_i^{∞} is the bulk concentration of the nanoparticles (2.7 x 10^{-4} M). As it can be seen from figure 3.19, the current took a linear behaviour after less than a second, which contradicts the Cottrell equation. Therefore, only the first 0.01 s were taken for the calculation, where the behaviour predicted by the equation is observed.

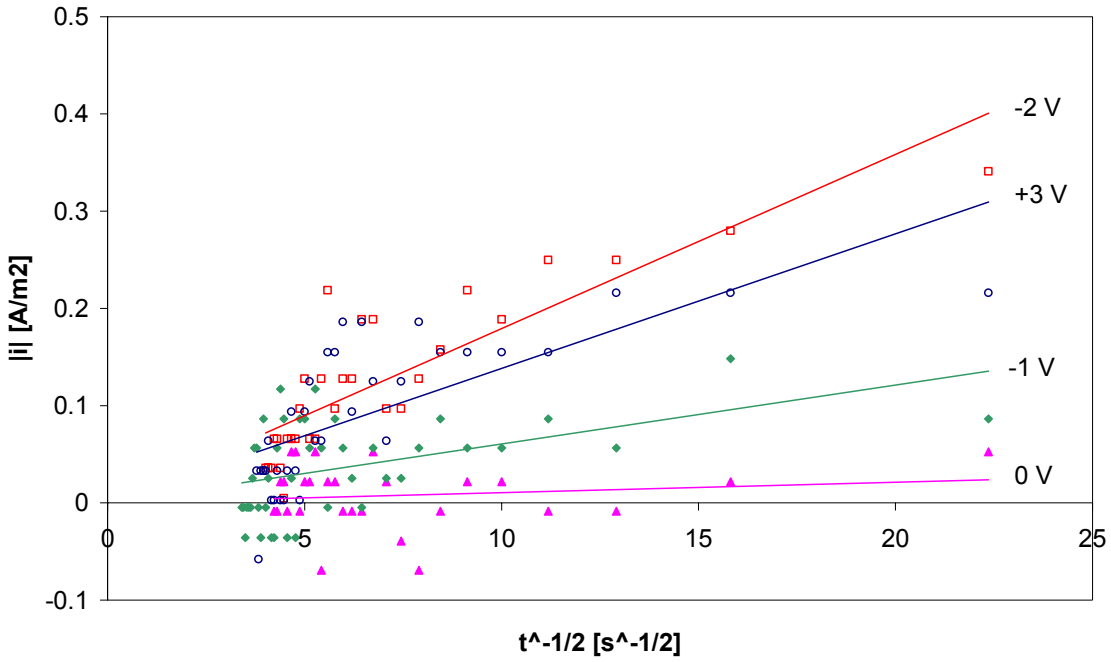

Figure **3.20.** |i| versus $t^{-1/2}$ plots for gold nanoparticles and step potentials -1, 0, +1, and +3 V.

The absolute current density, |i|, was plotted versus the inverse square root of time, $t^{-1/2}$ and linear regression lines were determined. As an example, in figure 3.20 above, four of the graphs for gold nanoparticles and -2, 0, -1, and +3 V are pictured, which correspond to the charge states -4, -2, -1 and +3 (from cyclic voltammetry, see also figure 3.13a).

The slopes of the straight lines in figure 3.20 are tabulated below in table 3.4 together with the diffusion coefficients derived from the slopes.

potential [V]	charge state	slope $dI/d(t^{-1/2})$	D [m^2 s]
-2	-4	0.0179	9.3×10^{-10}
-1	-2	0.0061	4.3×10^{-10}
0	-1	0.0011	5.6×10^{-11}
3	+3	0.0138	5.5×10^{-10}

Table 3.4. Diffusion coefficients calculated from the |i| vs. $t^{-1/2}$ plots.

In 2004, Chaki et al.[20] obtained near-linear graphs in I vs. $t^{-1/2}$ plots, but the diffusion coefficient they derived from these data was very much dependent on the charge state. At high positive or negative charge states, the diffusion coefficient calculated from chronoamperometric data differs by hundredfold or more from that for low charge states. The same trend is observed here. The smallest diffusion coefficients are found for nanoparticles which carry low charge. The more charge on a cluster, the faster it diffuses to and from the electrode. This could have many reasons such as contribution due to migration, or interaction with other charged or uncharged clusters, electrode surface, supporting electrolyte anions or cations, solvent molecules, and so forth.

Also it should not be forgotten that the cluster capacitance increases with charge as well (as it was shown in section 3.5), as if the monolayer thickness decreased when the core is in a high charge state. A reduced particle diameter at high charge states would also explain at least part of the increase of the diffusion coefficient with

charge. It will be open to future investigations, however, whether the thickness and structure of molecule monolayers on nanoparticles are affected by the charge state of the core or if the trends observed here are due to other reasons.

3.6.4 Determination by A. C. Impedance

From the Warburg part at low frequency in the impedance spectra, it should be possible to determine the diffusion coefficient, as described in section 2.13 from the Warburg line of unity slope. Unfortunately, none of the samples measured showed a straight line in the complex plane plot (see figure 3.21), so that these experiments could not be used for determination of the diffusion coefficient. All gold, silver and copper samples, except the ferrocenecarboxydodecanethiol protected gold nanoparticles, showed a suppressed semicircle at high frequency, a large semicircle at medium frequency and a curved line in the low frequencies.

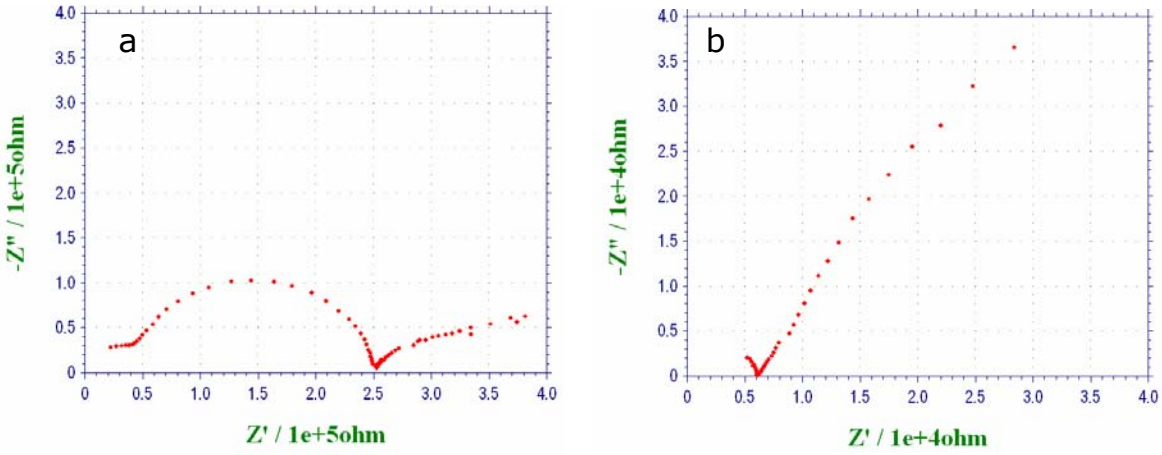

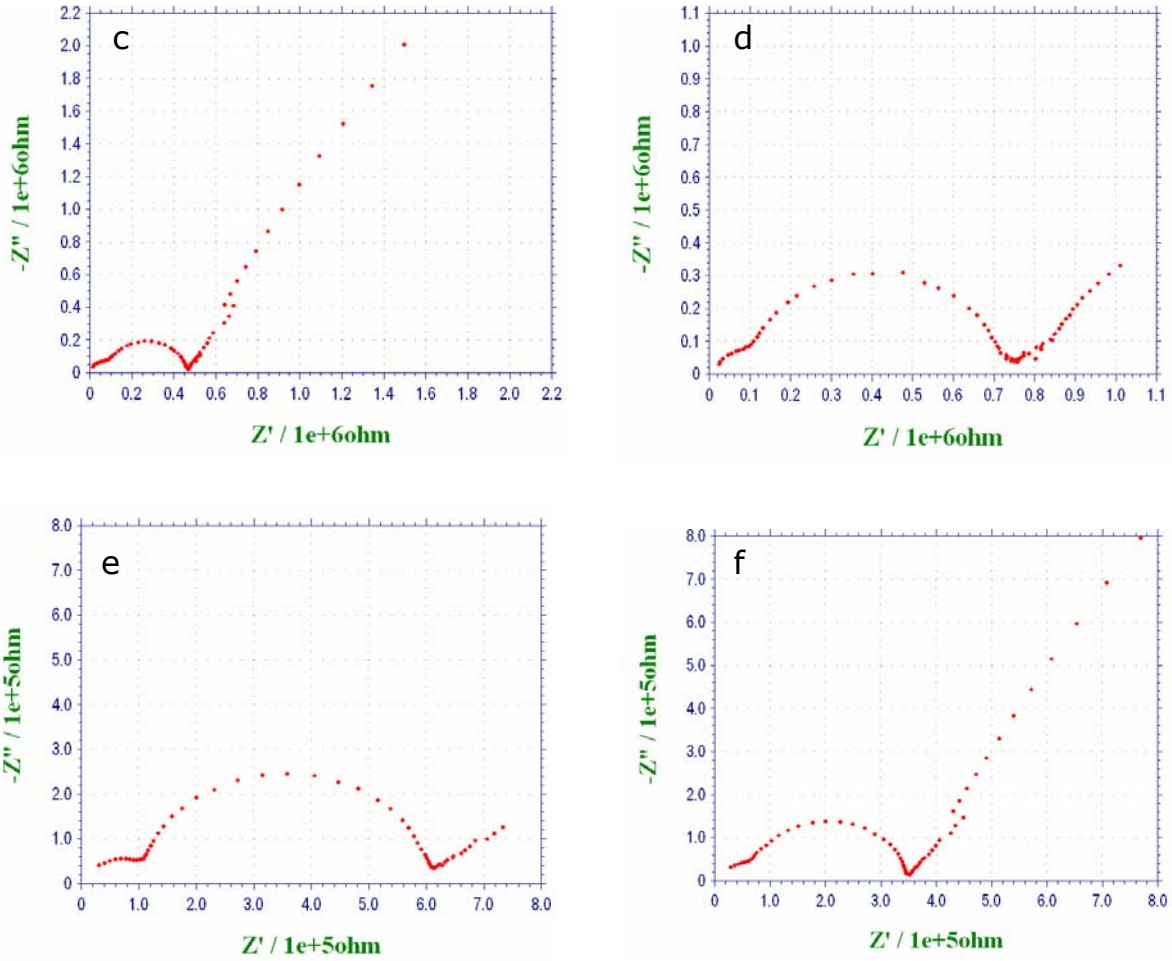

Figure 3.21. Complex plane A. C. impedance plots for (a) dodecanethiol, (b) ferrocenecarboxydodecanethiol, (c) ferrocenecarboxyoctanethiol protected gold, (d) dodecanethiol protected copper, (e) dodecanethiol protected silver, and (f) octanethiol protected silver nanoparticles at a 1 mm^2 gold electrode.

3.6.5 Comparison of the Diffusion Coefficient Results

The diffusion coefficients obtained from the Stokes-Einstein equation, the rotating disc, and from chronoamperometry are summed up in table 3.5.

Sample	D_{SE} [$m^2 s^{-1}$]	D_{RDE} [$m^2 s^{-1}$]	D_{CA} [$m^2 s^{-1}$]
Au C12	1.02×10^{-10}		
- 4			9.3×10^{-10}
- 2			4.3×10^{-10}
- 1			5.6×10^{-11}
+ 3			5.5×10^{-10}
Au FcC12		1.5×10^{-9}	
Cu C12	0.72×10^{-10}		
Ag C12	0.90×10^{-10}		
Ag C8	0.94×10^{-10}		

Table 3.5. Diffusion coefficients determined by Stokes-Einstein equation, D_{SE}, by rotating disc electrode voltammetry, D_{RDE}, and by chronoamperometry, D_{CA}. The numbers at sample Au C12 are the charge states for chronoamperometry.

The diffusion coefficients determined by the three methods described above correspond fairly well to each other. The rotating disc electrode and chronoamperometry measurements are in accordance with the theoretical predictions from the Stokes-Einstein equation. Rotating disc electrode gave the largest diffusion coefficient but this could be due to the ferrocene ligand groups interacting differently with the electrolyte than the dodecanethiol ligands. The values obtained in all of these experiments are well in the order of magnitude of molecules or particles of similar sizes.

3.7 Charge Transfer Resistance and Exchange Current from Impedance Measurements

The impedance spectra presented in figure 3.21 show two semicircles in all cases except for the ferrocenecarboxydodecanethiol protected

gold nanoparticles. These two semicircles correspond to two different relaxation processes and it is reasonable to attribute the larger semicircle to the nanoparticle charging and the smaller, less pronounced semicircle to the effect of the electrode double layer. Both can be represented by a parallel RC circuit, as shown in figure 3.23.

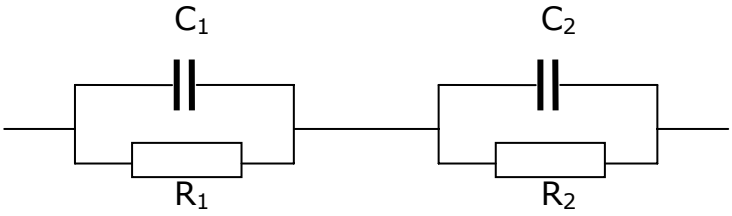

Figure 3.22. The Randles equivalent circuit for high frequencies for the A. C. impedance spectra of figure 3.21, represented by two RC circuits in a series.

In the A. C. impedance spectra the distance between the interpolated intercepts of the semicircles with the Z' axis gives R_{CT}, the charge transfer resistance for the respective relaxation process. Due to the fact that the small semicircles at very high frequency were very suppressed and not curved evenly, only the larger semicircle was used for determination of the charge transfer resistance. From the charge transfer resistance, the exchange current density, i_0, and the rate constant of the quantized charging process, $k^{0'}$, are calculated according to equations 3.10 and 3.11.

$$i_0 = \frac{RT}{nFR_{CT}A} \qquad (3.10)$$

$$k^{0'} = \frac{RT}{n^2F^2R_{CT}c} \qquad (3.11)$$

(A is the electrode area. A = 1 mm^2)

The results for all the spectra of figure 3.21 are tabulated in table 3.6 below.

sample	R_{CT} [Ω]	i_0 [A/cm^2]	$k^{0'}$ [$cm\ s^{-1}$]
Au C12	2.2×10^5	1.2×10^{-5}	4.4×10^{-5}
Ag C12	5.3×10^5	4.8×10^{-6}	1.8×10^{-5}
Cu C12	6.6×10^5	3.8×10^{-6}	1.5×10^{-5}
Au FcC8	4.0×10^5	6.3×10^{-6}	2.4×10^{-5}
Au FcC12	6.2×10^3	4.1×10^{-4}	1.6×10^{-3}
Ag C8	2.9×10^5	8.7×10^{-6}	3.3×10^{-5}

Table 3.6. Charge transfer resistance, R_{CT}, Exchange current, i_0, and electron transfer rate constant, $k^{0'}$, assuming n = 1, c = 2.7×10^{-4} M and T = 293 K.

The charge transfer resistance of all samples is in the 100 kΩ to 1 MΩ region, well above the resistance quantum (2.58×10^4 Ω, the minimum tunnelling resistance for single electron charging to be observed) mentioned in section 3.5, except the ferrocenecarboxydodecanethiol (FcC12) protected gold nanoparticles, which show a resistance of two orders of magnitude lower and a higher exchange current and rate constant. This could be due to the redox active moiety of the ferrocene enhancing electron tunnelling between electrolyte and metal core. With ferrocenecarboxyoctanethiol (FcC8) this effect is not observed, probably because of the lower ferrocene content in the ligand shell (see section 3.4) and the absence of the ferrocene redox signal in the CV (see section 3.6.2).

The lower charge transfer resistance of Ag C8 compared to Ag C12 could be due to the lower ligand shell thickness which allows a greater probability for electron tunnelling.

For all of the samples, the rate constant, $k^{0'}$, is very low compared to a "normal" redox reaction, such as the $Fe(CN)_6^{3-}/Fe(CN)_6^{4-}$ couple on a gold electrode ($k^{0'} \approx 2.3 \pm 0.7 \times 10^{-2}$ cm s^{-1})[21], indicating that the quantized charging process is kinetically very sluggish.

3.8 Transfer Coefficient and Exchange Current Density from Tafel Plots

As quantized capacitance electron transfer can be viewed as multivalency redox systems, it should be possible to determine kinetic data from Tafel plots of the charging waves. This was done with charging states of gold, silver and copper nanoparticles, as pictured in figure 3.23 below.

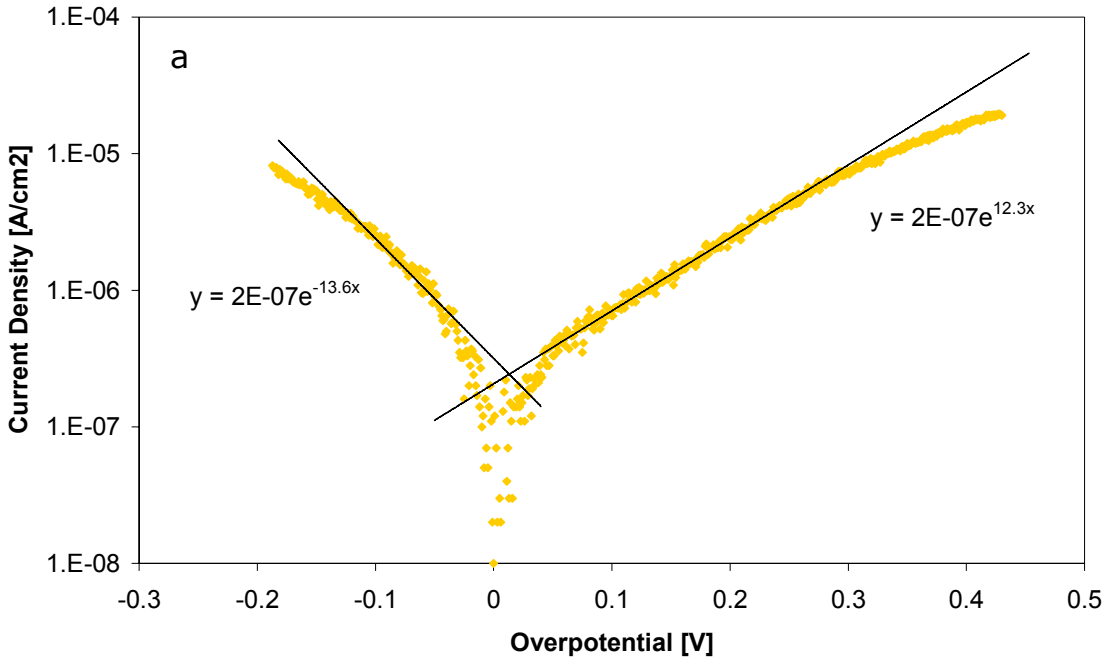

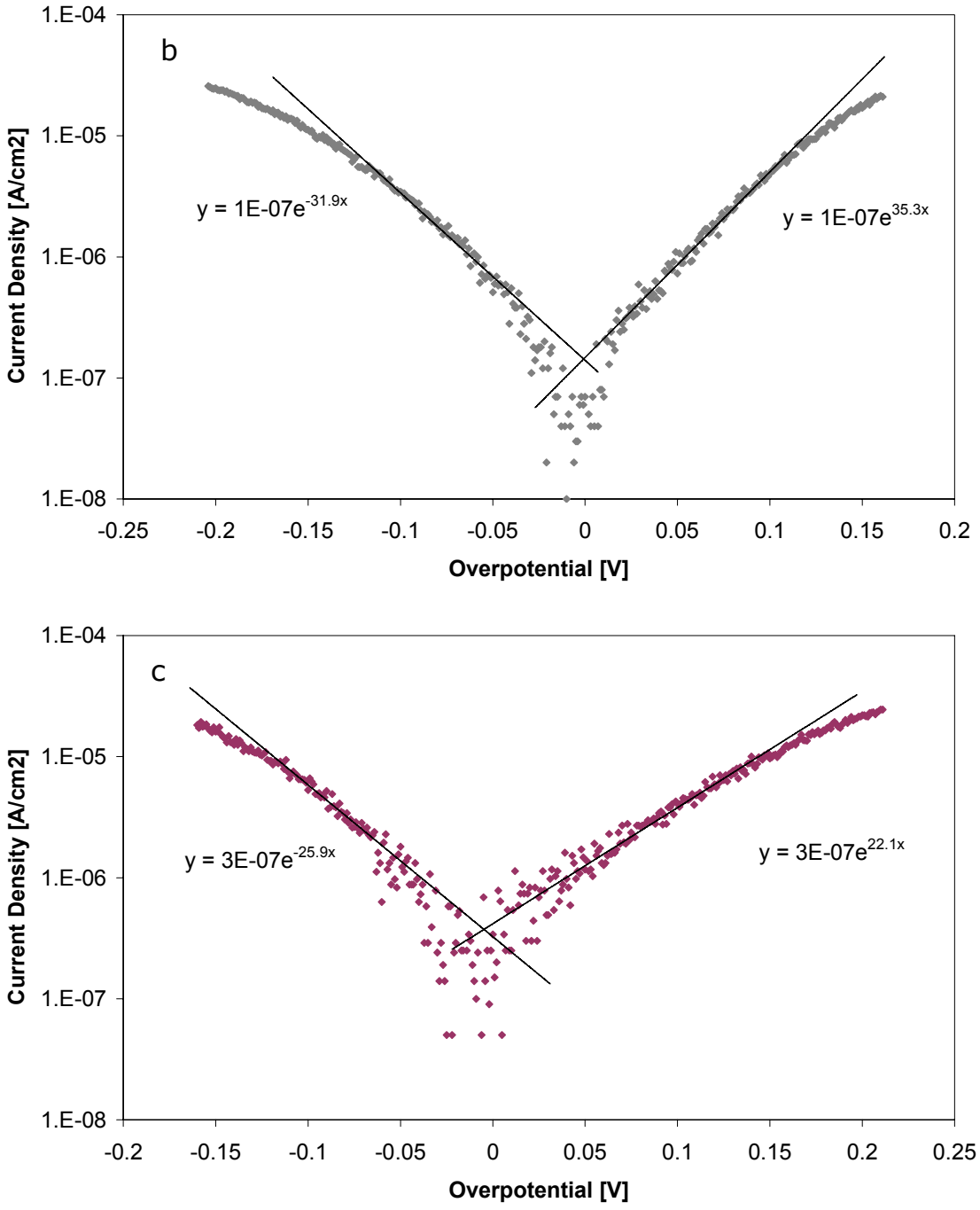

Figure 3.23. Examples of Tafel plots for (a) Au C12 (charge state -1), (b) Ag C12 (charge state 0), and (c) Cu C12 (charge state -3). The data points were taken from CVs (figure 3.14).

In these graphs, the data were fitted to straight lines in the areas of linear slope.

In section 1.1.4, the Tafel equations were derived from the Butler-Volmer equation.

For the anodic branch of the plot, the equation is as follows (in exponential notation):

$$i = i_0 e^{\frac{\beta_a nF}{RT}\eta} \qquad (3.12)$$

and for the cathodic branch:

$$i = i_0 e^{-\frac{-\beta_c nF}{RT}\eta} \qquad (3.13)$$

The values obtained are tabulated in table 3.7 below.

sample	**slope anodic**	**slope cathodic**	**β_a**	**β_c**	**i_0 [A cm^{-2}]**
Au C12	12.3	13.6	0.32	0.35	2.2 x 10^{-7}
Ag C12	35.3	31.9	0.91	0.82	1.4 x 10^{-7}
Cu C12	22.1	25.9	0.57	0.66	3.4 x 10^{-7}

Table 3.7. Anodic, β_a, and cathodic, β_c, charge transfer coefficients and exchange current densities, i_0, derived from the Tafel plots.

The anodic and cathodic charge transfer coefficients are very similar which indicates that the energy barrier between two adjacent charge states is symmetrical. The coefficients are smallest for gold and

largest for silver. This is very likely due to the difference in the spacing between charge states, as observed in CVs. The potentials of adjacent charge states are so close to each other that the outer ends of the Tafel plot for each charge state are already influenced strongly by the next charge state. The linear areas in the Tafel plots are limited by this fact. A mass transport control is never observed therefore because at overpotentials more than 0.2 - 0.3 V already the neighbouring charge state is activated.

The exchange current densities derived from the Tafel plots are very similar for gold, silver, and copper. They are about one order of magnitude smaller than those derived from A. C. impedance.

References

1. M. Brust, M. Walker, D. Bethell, D. J. Schiffrin, R. Whyman, *J. Chem. Soc., Chem. Commun.* (1994) 801
2. M. J. Hostetler et al., *Langmuir* **14** (1998) 17
3. S. He et al., *Langmuir* **17** (2001) 1571
4. S. Chen, A. C. Templeton, R. W. Murray, *Langmuir* **16** (2000) 3543
5. M. J. Hostetler, A. C. Templeton, R. W. Murray, *Langmuir* **15** (1999) 3782
6. M. J. Hostetler, S. J. Green, J. J. Stokes, R. W. Murray, *J. Am. Chem. Soc.* **118** (1996) 4212
7. R. S. Ingram, M. J. Hostetler, R. W. Murray, *J. Am. Chem. Soc.* **119** (1997) 9175
8. A. Labande, J. Ruiz, D. Astruc, *J. Am. Chem. Soc.* **124** (2002) 1782
9. Y. Shon, E. Cutler, *Langmuir* **20** (2004) 6626
10. D. K. Lee, Y. S. Kang, *ETRI Journal*, **26** (2004) 252
11. D. L. Van Hyning, W. G. Klemperer, C. F. Zukoski, *Langmuir* **17** (2001) 3120
12. S. Chen, J. M. Sommers, *J. Phys. Chem. B* **105** (2001) 8816
13. M. D. Malinsky, K. L. Kelly, G. C. Schatz, R. P. Van Duyne, *J. Am. Chem. Soc.* **123** (2001) 1471
14. J. H. Fendler, *Chem. Mater*. **13** (2001) 3196
15. M. J. Weaver, X. Gao, *J. Phys. Chem.* **97** (1993) 332
16. S. Chen, R. W. Murray, S. W. Feldberg, *J. Phys. Chem. B* **102** (1998) 9898
17. R. S. Ingram et al., *J. Am. Chem. Soc.* **119** (1997) 9279
18. B. Su, H. H. Girault, *J. Phys. Chem. B* **109** (2005) 11427
19. D. T. Miles et al., *J. Electroanal. Chem.* **554/555** (2003) 87
20. N. K. Chaki et al., *Langmuir* **20** (2004) 10208
21. K. Tokuda, T. Gueshi, H. Matsuda, *J. Electroanal. Chem.* **41** (1979) 102

4. Conclusion

In this work, an attempt was made to use the well-known gold nanoparticle synthesis method by Brust also for the synthesis of silver and copper nanoparticles.

With silver the reaction was successful; however the reaction mechanism seemed to be different. Silver was not transferred by the phase transfer agent but instead, a precipitation of silver bromide occurred. Even so, the final product of thiol protected silver nanoparticles showed properties and structure very similar to gold nanoparticles.

With copper, on the contrary, the Brust reaction did not yield only copper nanoparticles but also a large amount of larger crystals. Still, the nanoparticle content showed the spectroscopic and electrochemical response similar to that of the silver and gold nanoparticles. Some other experiments with different reducing agents and solvents yielded no copper particles. Instead, a white precipitate was obtained from the reaction of aqueous copper solutions with alkanethiol.

Size-effects were also observed through the application of alkanethiol ligands of different chain length on silver nanoparticle cores.

The exchange of ligands on monolayer protected clusters was studied with the redox active moiety of a ferrocenecarboxy-terminated thiol ligand. Here again, chain length effects were shown. Longer alkane chain ferrocene terminated ligands yielded higher degrees of exchange.

The stability of gold nanoparticles was excellent, silver nanoparticles showed light sensitivity, and copper nanoparticles aggregated within weeks and were presumably air sensitive.

Spectroscopic and electrochemical methods were applied on the various kinds of nanoparticles mentioned before. TEM images showed

core sizes and geometries. Silver and gold nanoparticles had near-spherical shapes whereas copper particles were faceted and of irregular shape, with vast amounts of larger crystals. From TEM images core size distributions were determined. Gold and silver showed narrow size distributions in the 3.5 nm and 4.6 nm regions, respectively. Copper showed a very broad distribution ranging from 2 to more than 10 nm with an average at 6.8 nm.

The UV/VIS spectra of silver nanoclusters showed a very pronounced surface plasmon absorbance peak at 430 nm. Gold nanoclusters, on the other hand, showed only a very weak surface plasmon resonance at 510 nm, superimposed on an exponential decay spectrum due to scattering because of the small particle size. Copper nanoparticles only showed a scattering profile and no characteristic absorbance band.

The capacitance of monolayer protected metal clusters was calculated, according to the concentric sphere capacitor model. These values were compared to those derived from cyclic voltammetry data which showed coulomb staircase behaviour of quantized capacitance charging. Theoretical and experimental values both proved that the capacitance of nanoclusters of the size considered here had sub-attofarad capacitances. However, contrary to assumptions in the quantized capacitance theory, the capacitance seemed to be charge-dependent, i.e. the capacitance was greater with higher core charge states. The introduction of further parameters in the quantized capacitance charging model could account for the obvious charge dependency of the cluster capacitance.

The coulomb blockade features also showed that the properties of metal nanoclusters are very different from those of their bulk metals. The finite size of nanoparticles leads to the onset of quantum effects

as they are observed in molecules. Nanoparticles have crystal lattices but in contrast to bulk metals, surface minimization forces them into shell structures such as truncated octahedra or icosahedra. The nanoparticles themselves are able to organize themselves to nanoparticle arrays of 2D and 3D lattices, thus exhibiting self-assembling abilities.

With the electrochemical methods of rotating disc electrode voltammetry, which is a hydrodynamic method, chronoamperometry, and A. C. impedance, the diffusion coefficient of nanoparticles was determined and the results in the order of magnitude of 10^{-10} m^2 s^{-1} were in good agreement with theoretical calculations.

From A. C. Impedance, data on the electron transfer kinetics were derived. The charge transfer resistance was in the 100 kΩ to 1 MΩ region, only a sample with high content of ferrocene-terminated ligands showed a resistance two orders of magnitude lower. Exchange current densities and electron transfer rate constants indicated a relatively slow electron transfer process, which is well described by the Butler-Volmer equation.

Exchange current densities were also determined from Tafel plots of a sample of the charging steps. The values were in the 10^{-7} A cm^{-2} order of magnitude, about 10-fold below the values obtained from A. C. impedance.

Transfer coefficients derived from the anodic and cathodic Tafel lines were very similar, indicating a relatively symmetric energy barrier for the electron transfer.

5. Outlook

The work undertaken here represents some of the basis of a field of research that is under very intense exploration these days. Every month there are reports of new applications for metal nanoparticles, and of new types of ligands and new methods for measuring their properties.

One of the immediate next steps is to try to apply the synthesis methods mentioned here on other metals, if possible also on less noble metals. The synthesis path for copper nanoparticles requires further improvement in order to obtain nanoparticles of better monodispersity, yield, and stability.

Future investigations will probably bring insight into the structure of the self-assembled layer on metal nanoparticles, its defects, and its behaviour when the core carries high charges. This will help to explain some of the phenomena, like the apparent increase of capacitance with high charge states, which shows in non-linear Z-plots. The linear model of quantized capacitance charging will have to be modified in order to account for this.

Acknowledgements

I would like to thank Dr. Michael Lyons for his support and kind supervision of this work. Thanks also to my family, who supported my stay in Dublin in many ways. A special thank you to my collegues in the physical electrochemistry group, Gar, Johnny, Michael B., Michael K., Ray, and Conchúir, for the hospitable reception, help, and stimulating discussions.

Abbreviations

CV	cyclic voltammetry
DCM	dichloromethane, methylene chloride
DPV	differential pulse voltammetry
HOMO	highest occupied molecular orbital
IHP	inner Helmhotz plane
LUMO	lowest unoccupied molecular orbital
MPC	monolayer protected cluster
NMR	nuclear magnetic resonance
NP	nanoparticle
OCP	open circuit potential
OHP	outer Helmholtz plane
RDE	rotating disc electrode
SAM	self-assembled monolayer
STM	scanning tunneling microscope
TBAP	tetrabutylammonium perchlorate
TEM	transmission electron microscopy
TOAB	detraoctylammonium bromide
XRD	X-ray diffraction

Symbols

Symbol	Meaning	Unit
A	geometric area of electrode	cm^2
A	absorption	-
a_i	activity of the species i	$mol\ dm^{-3}$
C_{CLU}	cluster capacitance	F
C_{dl}	double layer capacitance	$F\ cm^{-2}$
c_i	concentration of the species i	$mol\ dm^{-3}$
c_i^{∞}	concentration of species i in the bulk solution	$mol\ dm^{-3}$
c_i^{σ}	concentration of species i at the electrode surface	$mol\ dm^{-3}$
D_i	diffusion coefficient of the species i	$cm^2\ s^{-1}$
E	electrochemical potential	V
$E^{\otimes}$	standard potential	V
e	elementary charge	C
F	faraday constant ($F = 96485\ C\ mol^{-1}$)	$C\ mol^{-1}$
h	Planck's constant	J s
i	current density	$A\ cm^{-2}$
i_0	exchange current density	$A\ cm^{-2}$
i_a, i_c	partial current density of the anodic/cathodic electrode process	$A\ cm^{-2}$
i_L	limiting (plateau) current density	$A\ cm^{-2}$
J_i	flux of the species i	$mol\ s^{-1}\ cm^{-2}$
$k^{0'}$	rate constant of electrochemical reaction	$cm\ s^{-1}$
k_B	Boltzmann constant	$J\ K^{-1}$
n	number of electrons transferred	-
R	gas constant ($R = 8.314\ J\ K^{-1}\ mol^{-1}$)	$J\ K^{-1}\ mol^{-1}$

R_{ct}	charge transfer resistance	Ω
r_H	hydrodynamic radius	m
R_T	tunneling resistance	Ω
R_u	uncompensated resistance between reference electrode probe and working electrode	Ω
T	temperature	K
t	time	s
x	length	m
z	distance perpendicular to a rotating disc	cm
Z	impedance	Ω
Z’	real component of impedance	Ω
Z’’	imaginary component of impedance	Ω
z_i	charge number of the ionic species i	-
α	transfer coefficient	-
β	symmetry factor	-
δ	diffusion layer thickness	cm
ΔG^0	standard Gibbs free energy	J mol^{-1}
ε	molar absorptivity, extinction coefficient	cm^2 mol^{-1}
η	overpotential	V
ν	kinematic viscosity	cm^2 s^{-1}
ν_i	stoichiometric coefficient	-
σ	Warburg coefficient	Ω $s^{-1/2}$
Φ	electric potential	V
ω	angular frequency	s^{-1}